3002
TR3004

Polarized Neutron Reflectometry on Thin Magnetic Films

Gepolariseerde Neutronen Reflectometrie

aan Dunne Magnetische Lagen

The research described in this thesis was performed in the Department of Radiation Physics of the Interfacultair Reactor Instituut, Delft University of Technology, Mekelweg 15, 2629 JB Delft, The Netherlands.
Financial support was obtained from the Research Stimulation Fund of the Delft University of Technology, known as 'commissie Beek' and from the Netherlands Organisation for Scientific Research (NWO).

Polarized Neutron Reflectometry on Thin Magnetic Films

PROEFSCHRIFT

BIBLIOTHEEK TECHNISCHE UNIVERSITEIT DELFT

ter verkrijging van de graad van doctor
aan de Technische Universiteit Delft,
op gezag van de Rector Magnificus Prof.dr.ir. J. Blaauwendraad,
in het openbaar te verdedigen ten overstaan van een commissie,
door het College van Dekanen aangewezen,
op vrijdag 10 oktober 1997 te 10.30 uur
door

Anja VAN DER GRAAF

materiaalkundig ingenieur
geboren te Lekkerkerk

Dit proefschrift is goedgekeurd door de promotor:
Prof. dr. ir. L.A. de Graaf

Toegevoegd promotor:
Dr. M.Th. Rekveldt

Samenstelling promotiecommissie:

Rector Magnificus, voorzitter
Prof.dr.ir. L.A. de Graaf, Technische Universiteit Delft, promotor
Dr. M.Th. Rekveldt, Technische Universiteit Delft, toegevoegd promotor
Dr. H. Fredrikze, Technische Universiteit Delft
Dr.ir. F.J.A. den Broeder, Philips Research, Eindhoven
Prof.dr.ir. W.J.M. de Jonge, Technische Universiteit Eindhoven
Prof.dr.ir. E.J. Mittemeijer, Technische Universiteit Delft
Prof.dr. A. van Veen, Rijksuniversiteit Groningen en Technische Universiteit Delft
Prof.dr.ir. A. van den Beukel, Technische Universiteit Delft, reservelid

Dr. H. Fredrikze heeft als begeleider in belangrijke mate aan het totstandkomen van dit proefschrift bijgedragen.

CIP-DATA KONINKLIJKE BIBLIOTHEEK, DEN HAAG

Van der Graaf, Anja

Polarized Neutron Reflectometry on Thin Magnetic Films
/ Anja van der Graaf. – Delft : Delft
University of Technology, Faculty of Applied Physics. – Ill.
Thesis Technische Universiteit Delft. – With ref. –
With summary in Dutch.
ISBN 90-407-1526-2
NUGI 841
Subject headings: polarized neutron reflectometry / magnetic thin films.

Copyright © 1997 by Anja van der Graaf

All rights reserved.
No part of the material protected by this copyright notice may be reproduced or utilised in any form or by any means, electronic or mechanical, including photocopying, recording or by any information storage and retrieval system, without permission from the publisher.

Contents

1 General Introduction **1**

2 Theory of Polarized Neutron Reflectometry **5**
2.1 Basics of Neutron Reflectometry 5
2.2 Basics of Polarized Neutron Reflectometry 8

3 ROG, a Polarized Neutron Reflectometer **11**
3.1 Description of the Apparatus 11
3.2 Polarization Calibration by the 3P2S-method 17
3.3 Result of Polarization Calibration 19
3.4 Bulk Nickel Test Sample 20

4 Data Analysis **23**
4.1 Description of the Matrix Method 23
4.2 Correction for the Degree of Polarization 26
4.3 Influence of Divergence of the Neutron Beam 26
4.4 Other Corrections 28
4.5 Influence of Improper Degree of Polarization 29
4.6 Influence of Statistical Errors 32

5 PNR on Co-Cr **37**
5.1 Interest in Co-Cr 37
5.2 Description of the Experiments 38
5.3 Results and Interpretation PNR-Data 39
5.3.1 Correction for the Polarization Degree 41
5.3.2 Model fitted to the PNR-data 44
5.4 Comparison with Other Techniques: SEM and VSM 46
5.5 Discussion 48
5.6 Conclusions 50

6 PNR on Metal Evaporated Videotapes **51**
6.1 Introduction to Metal Evaporated Videotapes 51
6.2 Description of the PNR experiments 52
6.3 Results and Interpretation of PNR 54

6.3.1 Model of the One-layer Tape 58
6.3.2 Model of the Two-layer Tape 61
6.4 Correspondence with Other Techniques 66
6.5 Discussion 67
6.5.1 Nuclear Density 67
6.5.2 Magnetic Depth Profile of the One-layer Tape 68
6.5.3 Magnetic Depth Profile of the Two-layer Tape 72
6.5.4 Interlayer Variations of the Two-layer Tape 77
6.6 Conclusions 79

7 PNR on Fe/Si multilayers **81**
7.1 Interest in Fe/Si multilayers 81
7.2 Description of the Experiments 83
7.3 Results and Interpretation 83
7.4 Comparison with VSM 95
7.5 Discussion 95
7.6 Conclusions and Final Remarks 98

8 NiFe/Cu/NiFe/FeMn; a spin-valve system **101**
8.1 Interest in NiFe/Cu/NiFe/FeMn 101
8.2 Description of the Experiments 104
8.3 Interpretation of PNR-data 106
8.4 Correspondence with VSM 113
8.5 Discussion 113
8.6 Conclusions and Final Remarks 118

9 Conclusions and Final Remarks **121**

Bibliography **125**

Summary **131**

Samenvatting **135**

Glossary of Symbols **139**

Dankwoord **143**

Curriculum Vitae **145**

List of Publications **147**

Chapter 1

General Introduction

In a neutron reflection experiment one measures the fraction of specularly reflected neutrons as a function of their incoming perpendicular momentum. The obtained reflectivity curve is determined by the neutron scattering length density as a function of depth of the sample. This neutron scattering length density contains a nuclear and a magnetic contribution. Using polarized neutrons these two contributions can be separated. In this way polarized neutron reflectometry (PNR) is a tool to obtain magnetization depth profiles.

During the last decades thin film research and technology has made large progress, which made it possible to produce well defined thin films. The study of the physical properties of such thin films revealed a variety of interesting phenomena, especially among the magnetic properties. For example, the exchange coupling through non-magnetic layers was subject of research. The most well known systems used to investigate such coupling are Fe/Cr multilayers. Depending on the thickness of the chromium layer, the magnetization tends to align ferromagnetically, antiferromagnetically or biquadratically. The change from ferromagnetic to antiferromagnetic alignment can also cause a large change in electrical resistance : the so-called giant magneto resistance.

Another mechanism studied in multilayers is exchange-biasing. This phenomenon, first observed in oxidized cobalt particles, can now be used to shift the magnetization curve of a ferromagnetic layer adjacent to an antiferromagnetic layer along the field axis. Other subjects of research by PNR are the penetration depth of superconductors, perpendicular magnetic anisotropy in thin layers and the magnetic moment of atoms at interfaces.

All these magnetic phenomena are investigated by a variety of techniques: for example bulk magnetic methods as vibrating sample magnetometry (VSM), or surface techniques like the magneto-optic Kerr-effect (MOKE). Polarized neutron reflectometry is sensitive for the magnetization as a function of depth up to a few hundred nanometers. Therefore, PNR can give vital complementary information to improve the understanding of the magnetic properties as described—and others.

The maximum depth of about 200 nm on which neutron reflectometry can pro-

vide information is determined by the $\Delta q/q$-resolution of the experiment. Usually, the smallest details for which PNR is sensitive are of the order of a nanometer, although in the literature also reports are given on experiments with atomic layer resolution [1]. The latter resolution is largely determined by the sample-design. As nowadays the thin layers used for magnetic data storage and magnetic read/write devices have thicknesses in the depth-range on which PNR can provide information, it is very interesting to perform PNR experiments on such materials.

In January 1993 the neutron reflectometer ROG was installed at IRI. This reflectometer can be used in polarized and non-polarized mode. In this thesis pioneering polarized neutron reflectometry experiments performed on ROG are described. To gain experience and understanding of polarized neutron reflectometry also experiments were performed on CRISP, the neutron reflectometer at the ISIS facility of the Rutherford Appleton Laboratory, that can be used in polarized mode.

Nowadays the possibilities to use polarized X-rays to study magnetic phenomena in materials are also strongly developing [2]. One advantage of polarized neutron reflectometry as compared to the reflection of polarized X-rays is the penetration depth of neutrons, which is larger than for X-rays, so information can be obtained over a larger depth-range.

Another advantage of neutrons is that the nuclear and magnetic contribution to the neutron scattering cross section are of the same order of magnitude. For X-rays the total scattering cross section contains a classical Thomson (or charge) contribution, a purely magnetic contribution and an interference term between those two contributions. The purely magnetic scattering amplitude of X-rays is about 10^3 times smaller than the charge scattering amplitude. As only the unpaired electrons contribute to the purely magnetic scattering the magnetic scattering intensity is about 10^7 up to 10^8 times smaller than the charge scattering intensity. However, in ferro- or antiferromagnetic materials, always an interference term exists. In practice the magnetic fraction of this interference term intensity is about 10^{-3} [3]. After measuring this term in different magnetic states, the charge and magnetic terms can be separated by several methods [4]. In 1988 Resonant Exchange Scattering of X-rays was first demonstrated [5] to increase the measured intensity with a factor fifty. Using this technique the wavelength of the used X-rays is tuned near an absorption edge of the material investigated.

In order to be sensitive to magnetic scattering with X-rays very high intensities have to be used. This makes it necessary to use large installations like synchroton radiation sources providing high X-ray intensities. Polarized neutron experiments can be performed even at small reactors like the 2 MW reactor of IRI. In general PNR is used to determine magnetization depth profiles [6], whereas X-ray reflectometry is used to study magnetic surfaces [7].

Chapters 2 through 4 of this thesis are general chapters. The theory of neutron reflectometry is described in chapter 2, followed by a description of the ROG instrument in chapter 3, and chapter 4 deals with the data analysis. In the subsequent chapters PNR-experiments on different kinds of samples are discussed. First, experiments on a Co-Cr layer, a candidate to be used as perpendicular

recording medium, are described in chapter 5. In chapter 6 it is shown that PNR can give information on metal evaporated videotapes, as presently available in every ordinary shop selling videotapes, and also on the writing process in these tapes. Chapter 7 deals with experiments on Fe/Si multilayers. The initial interest in such multilayers was to obtain information on magnetic coupling through a semiconductor. In chapter 8 PNR-experiments on spin-valve systems, that probably will be used as magnetic read head material, are described. Finally, chapter 9 gives some conclusions and recommendations for the future.

Chapter 2

Theory of Polarized Neutron Reflectometry

2.1 Basics of Neutron Reflectometry

Using neutron reflectometry one measures the fraction of incident neutrons that is reflected specularly (i.e. angle of incidence is equal to angle of reflection) by a sample as a function of the incoming momentum of the neutrons in the direction perpendicular to the reflecting surface. The fraction of neutrons reflected is called the neutron reflectivity, R.

In general the wave function $\Psi(\vec{\mathbf{r}})$ of a neutron obeys the Schrödinger equation,

$$-\frac{\hbar^2}{2m_n}\nabla^2\Psi(\vec{\mathbf{r}}) + V(\vec{\mathbf{r}})\Psi(\vec{\mathbf{r}}) = E\Psi(\vec{\mathbf{r}}) \ , \tag{2.1}$$

where $\hbar$ is Plancks constant divided by 2π, V the potential energy, E the kinetic energy, m_n the mass of the neutron and $\vec{\mathbf{r}}$ is the position vector of the neutron considered. When $V = V_0$ for all $\vec{\mathbf{r}}$, the solution of Eqn. (2.1) describes a neutron beam as a plane wave with energy E:

$$E = \frac{\hbar^2}{2m_n}|\vec{\mathbf{k}}^2| + V_0 = \frac{\hbar^2}{2m_n}(k_x^2 \ + \ k_y^2 \ + \ k_z^2) + V_0, \tag{2.2}$$

where k_x, k_y and k_z represent the components of the wave vector $\vec{\mathbf{k}}$ in the medium with potential energy V_0.

The potential energy is given by [8]:

$$V(\vec{\mathbf{r}}) = \frac{2\pi\hbar^2}{m_n}n(\vec{\mathbf{r}})b(\vec{\mathbf{r}}), \tag{2.3}$$

with $n(\vec{\mathbf{r}})$ the atomic number density and $b(\vec{\mathbf{r}})$ the total neutron scattering length.

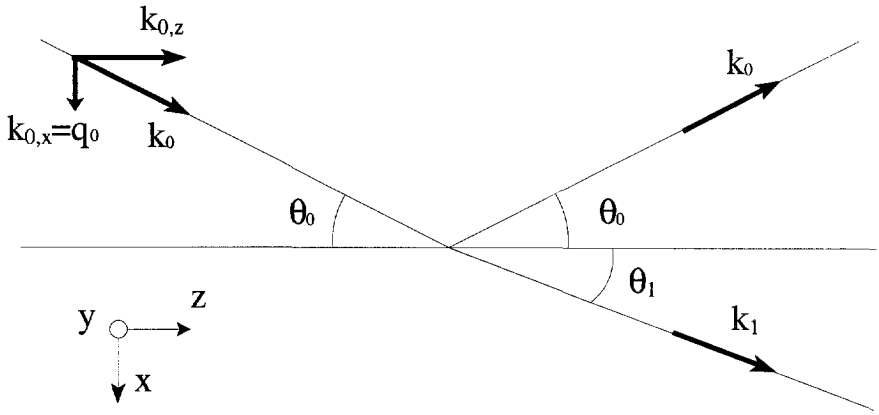

Figure 2.1: *Neutron beam reflecting at sample surface with direction convention used. The right-hand convention is used.*

Defining the neutron scattering length density, $\Gamma(\vec{\mathbf{r}})$:

$$\Gamma(\vec{\mathbf{r}}) = 4\pi n(\vec{\mathbf{r}})b(\vec{\mathbf{r}}) = \frac{2m_n V(\vec{\mathbf{r}})}{\hbar^2} \tag{2.4}$$

the Schrödinger equation can also be written as:

$$\nabla^2\Psi(\vec{\mathbf{r}}) + (k^2 + \Gamma_0 - \Gamma(\vec{\mathbf{r}}))\Psi(\vec{\mathbf{r}}) = 0 \ , \tag{2.5}$$

with k the length of the wave vector and Γ_0 the scattering length density outside the sample. In fact Γ is 4π times the actual scattering length density (Eqn. (2.4)). However, in the following Γ will be called the neutron scattering length density.

Usually in neutron reflectometry one uses samples that only exhibit variations of $\Gamma(\vec{\mathbf{r}})$ perpendicular to the reflecting surface, so the Schrödinger equation can be written in one dimension. In this thesis the neutron beam is supposed to travel in the xz-plane. The direction perpendicular to the sample surface is defined as the x-direction, so the z-direction is defined parallel to the sample surface. Variations of $\Gamma(\vec{\mathbf{r}})$ along the x-direction influence the specular neutron reflectivity. Figure 2.1 shows the direction convention used in this thesis schematically.

When $\Psi = \psi(x)\psi(y)\psi(z)$ and $\Gamma(\vec{\mathbf{r}})$ is independent of y and z, Eqn. (2.5) can be written in one dimension:

$$\frac{\partial^2\psi(x)}{\partial x^2} + (k_x^2 + \Gamma_0 - \Gamma(x))\psi(x) = 0 \ . \tag{2.6}$$

When $k_x^2 + \Gamma_0 - \Gamma(x)$ is not equal to zero, the solution of Eqn. (2.6) in a region where $\partial\Gamma(x)/\partial x = 0$, has the following form [9]:

$$\psi(x) = \alpha e^{ik_m x} + \beta e^{-ik_m x} \ , \tag{2.7}$$

with α and β determined by boundary conditions and k_m given by:

$$k_m = \sqrt{k_x^2 + \Gamma_0 - \Gamma(x)} \ . \tag{2.8}$$

If $k_x^2 + \Gamma_0 - \Gamma(x)$ is equal to zero, $\psi(x)$ is a linear function of x:

$$\psi(x) = \alpha + \beta x \ . \tag{2.9}$$

For $-\infty < x \leq 0$ (outside the sample) the solution of Eqn. (2.6) is given by:

$$\psi(x) = e^{ik_m x} + re^{-ik_m x} \ , \tag{2.10}$$

with r the reflectance (not to be confused with the position vector $\vec{\mathbf{r}}$), which obviously depends on k_x. However, this dependence will be omitted in notation. For negative x-values which are chosen so large that no interference between the incoming and the outcoming wave function takes place, the neutron reflectivity R is given by:

$$R = rr^* \ . \tag{2.11}$$

Using Eqn. (2.6) one can calculate $R(q)$ for a given $\Gamma(x)$ profile. As neutron reflectivity experiments determine R, the phase of the wave function is not obtained. This makes it impossible to calculate $\Gamma(x)$ directly from the reflectivity data. To interpret reflectivity data one usually assumes a model for $\Gamma(x)$ and fits this model to the measured data. The models used in this thesis assume slabs of constant $\Gamma(x)$ as will be discussed in section 4.1.

The quantity $\Gamma(x)$ in Eqn. (2.6) is averaged in the yz-plane. The dependence on x of the neutron scattering length density, Γ, is not always mentioned in this thesis when no confusion can arise.

Traditionally the neutron reflectivity is presented as a function of k_x, the perpendicular component of the incoming wave vector, also called q. When the angle of incidence is θ, q is given by:

$$q \ = \ |\vec{\mathbf{k}}| \ \sin\theta = (2\pi/\lambda)\sin\theta, \tag{2.12}$$

where λ is the wavelength of the neutron. In the literature sometimes the neutron reflectivity is presented as a function of the wave number transfer, Q:

$$Q \ = \ (4\pi/\lambda)\sin\theta \ (\ = \ 2q). \tag{2.13}$$

The neutron scattering length density, $\Gamma(\vec{\mathbf{r}})$ (given in Eqn. (2.4)) is a complex quantity. Absorption of neutrons is represented by a negative value of the imaginary part of the scattering length b and therefore of $\Gamma(\vec{\mathbf{r}})$ [8].

When the neutron beam coming from a medium with constant Γ_i hits an infinitely thick non-absorbing medium with constant Γ_{i+1}, only neutrons with kinetic energy larger than $\hbar^2(\Gamma_{i+1} - \Gamma_i)/2m_n$ will cross the interface; i.e. yield a neutron current density (equal to $\hbar(\Psi^*\nabla\Psi - \Psi\nabla\Psi^*)/2im$) with a non-vanishing component perpendicular to the interface. Therefore, assuming $\Gamma_{i+1} > \Gamma_i$, only

neutrons with $q > q_{cr}$, the critical q-value, will yield a perpendicular component in the neutron current. The value of q_{cr} is given by:

$$q_{cr} = \sqrt{\Gamma_{i+1} - \Gamma_i}\ . \tag{2.14}$$

For neutrons with q smaller than q_{cr} the wave function $\psi(x)$ decays exponentially as a function of x in the medium $i+1$. For neutrons with q larger than q_{cr}, the neutron reflectivity decreases according to Fresnel:

$$R(q_i) = \frac{|q_i - q_{i+1}|^2}{|q_i + q_{i+1}|^2}, \tag{2.15}$$

where q_i is the perpendicular component of the wave vector in the medium with Γ_i. For large values of q_i, Eqn. (2.15) approaches $(\Gamma_{i+1} - \Gamma_i)^2/16q_i^4$. When considering more complicated systems the reflectivity decreases also approximately proportional to q^{-4}. To obtain measurable intensities, the angle of incidence has to be chosen small, so q is also small. In practice angles in the order of a few mrad are used.

2.2 Basics of Polarized Neutron Reflectometry

Neutrons exhibit a spin $\vec{\sigma}$, related to the magnetic moment $\vec{\mu_{\mathbf{n}}}$ of the neutron by:

$$\vec{\mu_{\mathbf{n}}} = \gamma \mu_N \vec{\sigma} \tag{2.16}$$

with γ the gyromagnetic ratio equal to -1.91 [10] and μ_N the nuclear magneton equal to $e\hbar/2m_pc$ where e is the elementary charge, m_p is the proton mass and c is the velocity of light.

From quantum mechanics it follows that the magnitude of the spin of a neutron is always $\hbar/2$, and only one component of the spin can be quantized along a chosen direction giving the values $\hbar/2$ or $-\hbar/2$. A neutron beam is perfectly polarized when all the determined components of the neutron spins along the chosen direction have the same sign. As γ is negative, the spin of a neutron is antiparallel to its magnetic moment. For convenience, however, in this thesis 'spin parallel' and 'spin antiparallel' is used for the magnetic moment of the neutron or neutron beam parallel and antiparallel to the applied field.

Because of the magnetic moment corresponding to the spin the potential energy of a neutron contains a nuclear and a magnetic term,

$$V = V_n + V_m. \tag{2.17}$$

The nuclear part of V is given by the following equation:

$$V_n = \frac{2\pi\hbar^2}{m_n} n b_n = \frac{\hbar^2}{2m_n}\Gamma_n, \tag{2.18}$$

where n is the particle density, b_n is the nuclear neutron scattering length, and Γ_n the nuclear scattering length density multiplied by 4π, in this thesis called nuclear scattering length density, for convenience.

The magnetic part of the potential energy may be written as [10]:

$$V_m = \pm\mu_n B, \tag{2.19}$$

with B the magnitude of magnetic induction and the +(-) applies for the spin component parallel(antiparallel) to the induction.

When reflecting at an interface, the differences in potential energy ΔV, rather than the potential energy itself, are of importance (see Eqn. (2.7)). When coming from vacuum, $\Delta V_n = V_n$, because $V_{n,vacuum} = 0$.

The samples, used in neutron reflectometry, are usually homogeneous in the yz-plane, so $\partial B_y/\partial y = 0$ and $\partial B_z/\partial z = 0$. Because of Maxwell's law:

$$\nabla \cdot \vec{\mathbf{B}} = 0 \ , \tag{2.20}$$

the difference in magnetic induction perpendicular to the surface $\partial B_x/\partial x$ vanishes. Therefore, the difference in magnetic potential experienced by a neutron when entering a sample, with the applied field parallel to the sample, is given by:

$$\begin{aligned} |\Delta V_m| &= \mu_n(\sqrt{B_y^2 + B_z^2} - B_0) \\ &= \mu_0\mu_n(\sqrt{(M_y + H_{y,0})^2 + (M_z + H_{z,0})^2} - H_0), \end{aligned} \tag{2.21}$$

where μ_0 is the magnetic permeability of vacuum, M_y and M_z are the in-plane components of magnetization, and H_y and H_z are the in-plane components of the applied magnetic field both in the sample. B_0 and H_0 are the magnetic induction and the magnetic field outside the sample. In the literature [11, 12] the influence of both in-plane magnetization components on the neutron reflectivity is described.

In the experiments described in this thesis the magnetic field is usually applied in the y-direction, parallel or antiparallel to the polarization direction of the neutron beam. Further it is assumed that the in-plane magnetization in the sample is parallel to the applied field direction, so Eqn. (2.21) can be simplified to:

$$|\Delta V_m| = \mu_n|B_y - B_0| = \mu_0\mu_n|M_y|. \tag{2.22}$$

Analogous to the nuclear scattering length b_n, a magnetic scattering length p can be defined. This magnetic scattering length is related to μ_s the magnetic moment per atom expressed in units of Bohr magnetons, according to:

$$p = \frac{m_n\mu_n\mu_0}{2\pi\hbar^2}\mu_s \ . \tag{2.23}$$

The magnitude of the magnetic potential difference when entering a sample can now be written in terms of p or Γ_m, the magnetic scattering length density:

$$|\Delta V_m| \equiv \frac{\hbar^2}{2m_n}\,\Gamma_m = \frac{2\pi\hbar^2}{m_n}\frac{M_p}{M_s}np \ , \tag{2.24}$$

with M_s the magnetization of the sample at saturation and M_p the magnetization component parallel to the polarization direction of the beam.

Magnetizing the sample to saturation in the direction perpendicular to the surface of the sample, B_y and B_z vanish. Because $\nabla \cdot \vec{\mathbf{B}} = 0$, B_x is the same in and outside the sample. Therefore, in this case, neutrons hitting the sample only experience changes in V_n and the neutron reflectivity is only determined by Γ_n.

Summarizing for an in-plane applied magnetic field when coming from vacuum, Γ can be written as the sum of the nuclear and the magnetic part:

$$\Gamma = \Gamma_n \pm \Gamma_m = 4\pi n(b_n \pm p\frac{M_p}{M_s}), \tag{2.25}$$

where '+(-)' applies for the parallel(antiparallel mode), while for a perpendicular applied magnetic field:

$$\Gamma = \Gamma_n = 4\pi n b_n. \tag{2.26}$$

Chapter 3

ROG, a Polarized Neutron Reflectometer

3.1 Description of the Apparatus

ROG is the time-of-flight neutron reflectometer, to be used in polarized and non-polarized mode, and installed at the 2 MW swimming-pool reactor HOR (Hoger Onderwijs Reactor) of IRI at Delft University of Technology.

ROG uses a white neutron beam, i.e. covering a broad range of the wavelength spectrum. The travelling time of the neutron between two points is measured. In this way the velocity (and therefore the wavelength) of the reflected neutrons can be determined. This method is called time-of-flight or TOF.

When using ROG in polarized mode, the beam is reflected by a polarizing supermirror. This mirror reflects only one spin state, so ideally 50 % of the neutrons are lost. Therefore, no supermirror, or a non-polarizing supermirror, which reflects a higher percentage of the neutrons, is used when ROG is operated in non-polarized mode, unless a deflected beam is needed for liquid samples.

When the index of refraction (directly related to the neutron scattering length density) for neutrons in vacuum is defined as 1, the value of the index of refraction will be only of the order of 10^{-5} smaller than 1 for most materials. This results in very small critical angles, θ_{cr}, typically a few mrad, for the wavelength range of neutrons used by ROG. The critical angle of a system is the angle of incidence below which all neutrons are reflected. As the neutron reflectivity decreases proportional to $(q-q_{cr})^{-4}$ with $q_{cr} = 2\pi \sin\theta_{cr}/\lambda$, measurements should be performed at angles slightly larger than θ_{cr}. To be able to define such angles accurately, the dimension of ROG parallel to the neutron beam was designed large: ≈ 6.5 m. The part of ROG where the beam is defined, reflected and detected is manufactured out of one piece of aluminium, to optimize the stability of the apparatus and the reproducibility of the settings.

In the following the different parts which the neutrons encounter when travel-

ling along the neutron beam used by ROG are presented. In Figure 3.1 a schematic view of the ROG instrument is given. More details about ROG can be found in [13, 14].

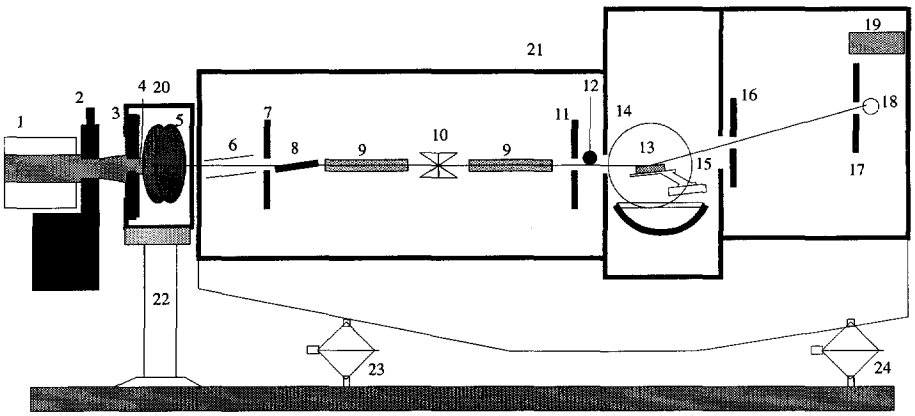

1	stacked neutron guide	9	neutron guides	17	detector diaphragm
2	beam shutter	10	spin flipper	18	^{3}He detector
3	coarse collimator	11	diaphragm 2	19	PSD
4	monitor 1	12	monitor 2	20	short frame
5	chopper	13	sample	21	long frame
6	super mirror	14	electromagnet	22	Leg 1 & 2
7	diaphragm 1	15	sample table	23	Leg 3
8	frame-overlap mirror	16	shielding diaphragm	24	Leg 4

Figure 3.1: *Schematic view of ROG, (not on scale).*

The definition of directions as given in chapter 2 will be used. The direction perpendicular to the sample surface is called the x-direction. The neutron beam is travelling in the xz-plane. The angle of the neutron beam with the z-axis (parallel to the sample surface) determines the angle of incidence. The y-axis is defined as perpendicular to the neutron beam in the surface of the sample. For clarity these directions are given in Figure 3.2.

ROG has been positioned behind the **stacked neutron guide (SNG)** [15, 16] at HOR. This device diminishes the amount of γ-rays and fast neutrons in the beam, resulting in a very clean thermal neutron beam with a total intensity of 2.0×10^7 cm^{-2}s^{-1}. The maximum flux of 2.3×10^8 s^{-1}cm^{-2}nm^{-1}, occurs at a wavelength of 0.160 nm.

After leaving the SNG the neutron beam first encounters the short frame, on which the coarse collimator, the first monitor and the chopper are positioned. The coarse collimator selects a beam of 27 mm width and a height between 0 and

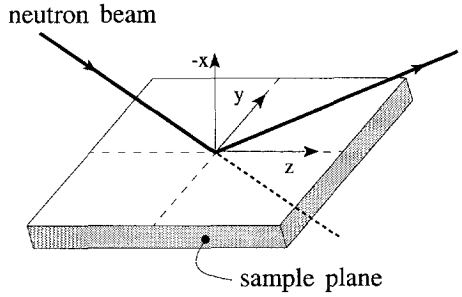

Figure 3.2: *Definition of directions.*

15 mm. Usually the height of the coarse collimator is set on a value of a few mm. The first monitor checks the intensity of the beam. When this intensity is below a preset value, due to low reactor power, the measurement is temporarily stopped. As ROG uses the time of flight method to determine the wavelength of the neutrons, neutron pulses are created by the chopper.

The **chopper** [17] consists of two neutron absorbing disks which rotate around the same axis. A schematic view of the chopper is shown in Figure 3.3. To resist

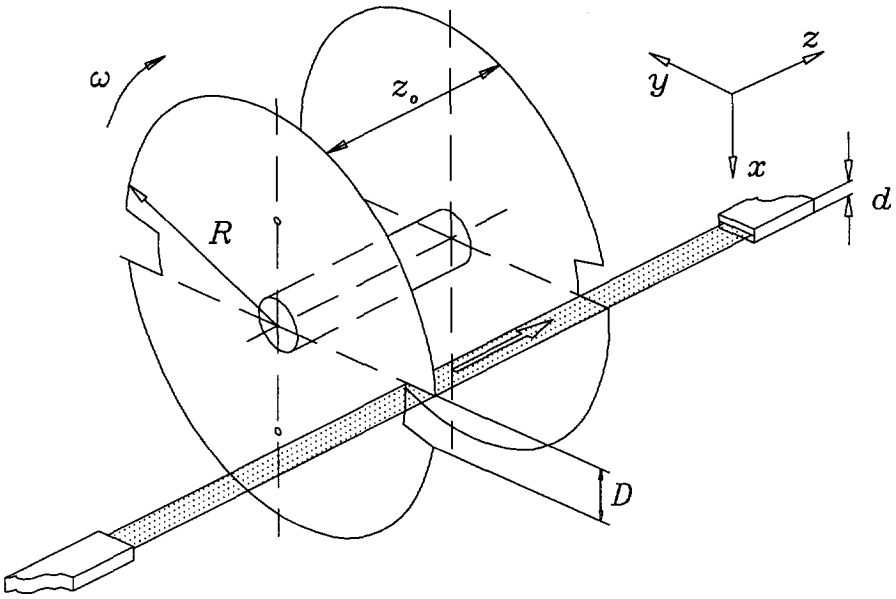

Figure 3.3: *Schematic view of chopper.*

the large forces, resulting from the possibly high speed of rotation (up to 20000 rpm), the disks are made of 19 slabs of a carbon-fiber-reinforced grid embedded in a resin. ^{10}B powder was distributed on the slabs before pressing the slabs, when

the resin is turned into epoxy. After pressing, 16 layers of paint mixed with Gd_2O_3 were applied to the disks to enlarge the neutron absorption. In the measurements presented in this thesis the chopper rotated at a speed of 1800 rpm. Both disks have two opposite open sections of 30 degrees. One disk is rotated 30 degrees with respect to the other disk (see Figure 3.3). Running the chopper the neutron beam is chopped into pulses of neutrons that are fast enough to reach the second disk before the open section has passed the beam path. The time at which a new pulse starts is electronically registered.

Behind the short frame, the long frame is positioned. The first component the neutrons encounter at the long frame is the **supermirror** table. This table contains three supermirrors above each other. One of these mirrors can be selected to reflect the beam. Therefore height and angle of the supermirror table can be adjusted by computer control. One of the mirrors is a polarizing mirror in order to make measurements with polarized neutrons possible. This mirror has a much higher reflectivity for neutrons in one spin-state than for neutrons in the opposite spin-state. Other mirrors are used to deflect the beam, so the possible interval of angles of incidence on the sample is enlarged. The stacked neutron guide produces a beam that is tilted downwards at 0.0133 rad with respect to the horizon. By using a supermirror the surface of liquids can be measured at angles different from 0.0133 rad. It might be interesting to measure the neutron reflectivity from the bottom side of a sample. In that case a supermirror can be used to deflect the beam upwards.

As the polarization of a neutron beam diminishes when encountering large gradients of the magnetic field, a magnetic **guide field** is needed along the beam. Therefore, around the neutron beam a magnetic guide field of about 500 A/m in the same direction as the magnetization direction of the polarizing mirror is created by permanent ferroxdure 330 magnets.

Neutron guides are installed to prevent loss of neutrons by beam divergence in the yz-plane. Those neutron guides consist of neutron mirrors installed on both sides of the beam at 30 mm mutual distance.

The divergence of the beam in the xz-plane, determining the spread in the angle of incidence on the sample, is defined by two **diaphragms**, of which the width and height can be adjusted. The center of these diaphragms is positioned 150 mm above the long frame. Therefore, the neutron beam always travels parallel to the long frame at a height of 150 mm above the frame. The distance between the two diaphragms is 3 m. The width of the diaphragms can be adjusted between 0 and 30 mm and the height between 0 and 10 mm.

Of course after entering the chopper, slow neutrons might pass through an open section of the second rigid disk which passes the beam path, after this disk has rotated more than π rad. To get rid of these unwanted slow neutrons, the **frameoverlap mirror** is used in transmission. The low energy neutrons will be reflected out of the beam and the high energy neutrons will be transmitted through this mirror.

When using polarized neutrons usually one wants to perform the PNR- experiments with the polarization directed in two antiparallel directions (see Eqns. (2.19)

and (2.25)). On the ROG an **adiabatic spin flipper** (shown in Figure 3.4) has been installed to turn the polarization of the beam π rad. This spin flipper is composed of two adiabatic polarization rotators, as described by Kraan et.al. [18]. In non-spin flip mode the polarization is turned $\pi/2$ rad by the first rotator and then turned $\pi/2$ rad backwards by the second rotator to the original polarization direction. In spin flip mode the direction of the current in the second rotator is changed to turn the polarization another $\pi/2$ rad to obtain polarization in the opposite direction. In the two rotators the spin of the neutrons will "follow" the magnetic field adiabatically, by precession around the magnetic field. The advantage of such an adiabatic spin flipper is that a polarized neutron beam travels through (almost) the same gradients of magnetic field, whether the polarization of the beam is turned or not. Therefore the polarization degree of the beam does not depend on the operation mode of the spin flipper.

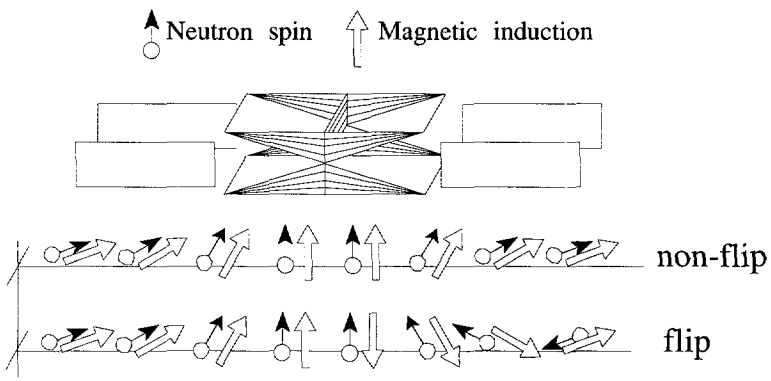

Figure 3.4: *Schematic view of spin flipper and the flipping mechanism.*

Before entering the sample compartment of ROG, the neutrons encounter the **second monitor**. This monitor is used to count how many neutrons enter the sample compartment. This monitor is positioned as close to the sample as possible, to diminish wavelength dependent loss of neutrons between the monitor and the sample.

The **sample table** in the sample compartment can be rotated around the y-axis to obtain the desired reflection angle. It can also be adjusted in height and be rotated around the z-axis to optimize the number of neutrons reflecting from the sample.

Also a water-cooled **electromagnet** can be installed. The magnitude of the applied magnetic field can be adjusted by changing the magnetizing current through both poles and by changing the distance between both pole shoes. This magnet creates a magnetic field along the y-axis of maximal 690 kA/m. The value of the current through the magnet is computer controlled.

When one wants to measure the neutron reflectivity of a magnetic sample as determined by the nuclear structure only, the sample has to be magnetized perpen-

dicular to the beam. The device designed to obtain a magnetic field perpendicular to the sample is shown in Figure 3.5. The device is made such that the vertical

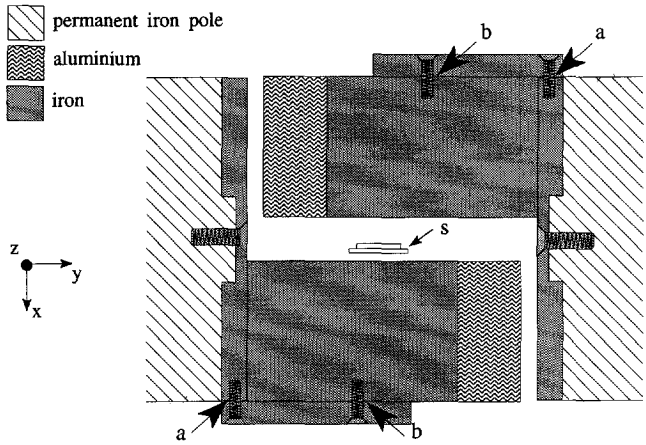

Figure 3.5: *Schematic view of the device to create a magnetic field perpendicular to the sample surface. The permanent parts of the pole shoes are marked by diagonal lines. The vertical distance between the two parts of the devices can be increased by putting rings at interface* **a** *and can be decreased by putting rings at interface* **b**, *depending on the thickness of the sample positioned on the sample table* **s**.

distance at the sample position between the two poles can be adapted. In this way the distance between the two poles can be arbitrarily small, depending on the sample thickness.

To minimize background at the detector, a **shielding diaphragm** is installed at the back of the sample compartment. The upper and lower part of this diaphragm can be adjusted separately.

The detector compartment contains a **^{3}He detector** and a **position sensitive detector**. Both detectors can be adjusted in x-, y- and z-position. All measurements presented in this thesis performed on ROG were performed with the ^{3}He detector, which has a sensitive length of 150 mm in the y-direction. In front of this detector a diaphragm is installed to minimize the background further.

The long frame is supplied with three perspex hoods. In the future they will be used to perform measurements in an argon atmosphere, to diminish the scattering by air. However, presently they are not functioning yet. Recently ROG has been supplied with a polarization analysis unit consisting of a spin flipper and a polarizing unit, both installed between the sample and the detector. Using polarization analysis, one can also perform reflectivity experiments that give information on the magnetic components in the x- and z-direction.

Most components of ROG can be automatically controlled by a processor card on a VME-bus, increasing the reproducibility of measurements. After data col-

lection by the VME computer the data are transferred to a VMS workstation for data storage and processing. In the future software will be available to measure the two spin-states alternately. The measurements presented in this thesis are obtained by measuring two spin states successively in only two subsets.

3.2 Polarization Calibration by the 3P2S-method

As the reflectivity of the polarizing mirror and also the depolarization by gradients in the magnetic field are wavelength dependent, the polarization of the beam at the sample is also wavelength dependent. To take into account the influence of the imperfection of the polarization on the experimentally obtained polarized neutron reflectivity data , the degree of polarization of the beam as a function of wavelength needs to be known. The degree of polarization P, is defined as follows:

$$P(\lambda) = \frac{I^+(\lambda) - I^-(\lambda)}{I^+(\lambda) + I^-(\lambda)} , \tag{3.1}$$

where I^+ is the intensity of neutrons with their magnetic moment along a certain analysing direction and I^- is the intensity of neutrons with opposite magnetic moment. The polarization of the beam can be reversed by the spin flipper. The design of the adiabatic spin flipper is such that the depolarization caused by the spin flipper is the same for both polarization directions of the beam.

To calibrate the degree of polarization of the beam, the so-called 3P2S-method (traditionally using 3 polarizers and 2 shims) with spin flippers instead of shims is applied [19]. The first polarizer is the polarizing supermirror of ROG, the first spin flipper is the spin flipper of ROG. At the sample position the second polarizer is positioned. For this second polarizer a polarizing mirror was used, magnetized in the y-direction. Between this polarizing mirror and the detector a second spin flipper consisting of two adiabatic rotators and a third polarizing mirror are placed. The alignment has to be such that the neutron beam is reflected by both the polarizing mirror at the sample position and by the last polarizing mirror. In Figure 3.6 a schematic view of the set-up when performing the calibration is given.

To calibrate the polarization degree of the beam, four intensities at various operation modes of both spin flippers are measured. The following formulas [19] describe the four intensities I:

$$\begin{aligned} I^{++} &= I_0\{R^{++}(1+\alpha_1 P_1)(1+\alpha_2 P_2) + R^{--}(1-\alpha_1 P_1)(1-\alpha_2 P_2) \\ &\quad + R^{+-}(1+\alpha_1 P_1)(1-\alpha_2 P_2) + R^{-+}(1-\alpha_1 P_1)(1+\alpha_2 P_2)\} \end{aligned} \tag{3.2}$$

$$\begin{aligned} I^{--} &= I_0\{R^{++}(1-\alpha_1 P_1)(1-\alpha_2 P_2) + R^{--}(1+\alpha_1 P_1)(1+\alpha_2 P_2) \\ &\quad + R^{+-}(1-\alpha_1 P_1)(1+\alpha_2 P_2) + R^{-+}(1+\alpha_1 P_1)(1-\alpha_2 P_2)\} \end{aligned} \tag{3.3}$$

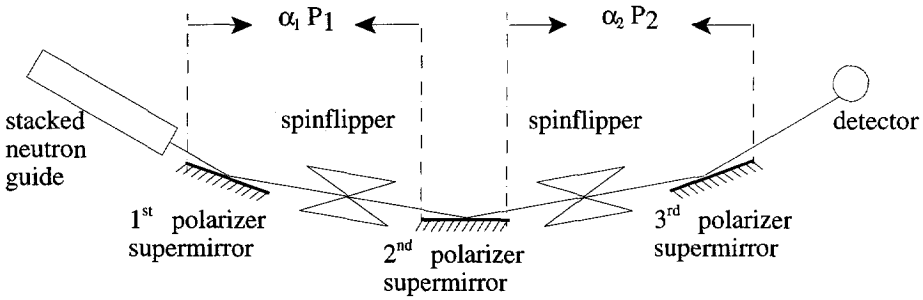

Figure 3.6: *Schematic view of set-up to calibrate $\alpha_1 P_1$ by means of the 3P2S-method.*

$$\begin{aligned} I^{+-} &= I_0\{R^{++}(1+\alpha_1 P_1)(1-\alpha_2 P_2) + R^{--}(1-\alpha_1 P_1)(1+\alpha_2 P_2) \\ &\quad +R^{+-}(1+\alpha_1 P_1)(1+\alpha_2 P_2) + R^{-+}(1-\alpha_1 P_1)(1-\alpha_2 P_2)\} \end{aligned} \tag{3.4}$$

$$\begin{aligned} I^{-+} &= I_0\{R^{++}(1-\alpha_1 P_1)(1+\alpha_2 P_2) + R^{--}(1+\alpha_1 P_1)(1-\alpha_2 P_2) \\ &\quad +R^{+-}(1-\alpha_1 P_1)(1-\alpha_2 P_2) + R^{-+}(1+\alpha_1 P_1)(1+\alpha_2 P_2)\} \ , \end{aligned} \tag{3.5}$$

with

I_0 : a normalization constant
P_1 : the polarizing power of the polarizing mirror at the beginning of the apparatus
α_1 : the depolarization of the beam before it hits the sample
P_2 : the polarizing power of the polarizing mirror between the second spin flipper and the detector
α_2 : the depolarization of the beam after it hits the sample
R : the reflectivity of the sample.

The first(second) sign in the superscript of I refers to the operation mode of the spin flipper before(after) the sample. '+' refers to non-spin flip and '-' refers to spin flip. The first(second) sign in the superscript of R refers to the direction of the spin of the neutron before(after) reflection at the supermirror at the sample position, '+' refers to spin parallel and '-' to spin antiparallel. The direction of the spin may change when the magnetization of the sample has a component perpendicular to the direction of the spin. As the supermirror on the sample position is magnetized in the direction parallel to the polarization direction of the beam by ferroxdure magnets, this component is supposed to be absent and therefore R^{+-} and R^{-+} are supposed to be equal to 0. Then Eqns. (3.2) through (3.5) can be simplified:

$$I^{++} = I_0\{R^{++}(1+\alpha_1 P_1)(1+\alpha_2 P_2) + R^{--}(1-\alpha_1 P_1)(1-\alpha_2 P_2) \tag{3.6}$$

$$I^{--} = I_0\{R^{++}(1-\alpha_1 P_1)(1-\alpha_2 P_2) + R^{--}(1+\alpha_1 P_1)(1+\alpha_2 P_2) \tag{3.7}$$

$$I^{+-} = I_0\{R^{++}(1+\alpha_1 P_1)(1-\alpha_2 P_2) + R^{--}(1-\alpha_1 P_1)(1+\alpha_2 P_2) \quad (3.8)$$

$$I^{-+} = I_0\{R^{++}(1-\alpha_1 P_1)(1+\alpha_2 P_2) + R^{--}(1+\alpha_1 P_1)(1-\alpha_2 P_2) \quad (3.9)$$

After normalization to I_0 Eqns. (3.6) through (3.9) contain only four unknown variables: R^{++}, R^{--}, $\alpha_1 P_1$ and $\alpha_2 P_2$. Following the method as described in [19] one can obtain the product $\alpha_1 P_1$ (in [19] denoted αP). This product determines the polarization of the beam before it hits the sample. The relative times of measurement of the different intensities have been optimized in such a way that the relative statistical accuracy with which $\alpha_1 P_1$ can be determined is optimal [20], because this is the quantity that is interesting for polarization corrections on reflectivity data.

3.3 Result of Polarization Calibration

The polarization of the ROG neutron beam when hitting the samples as a function of λ, as determined using the described 3P2S-method, is given in Figure 3.7. One

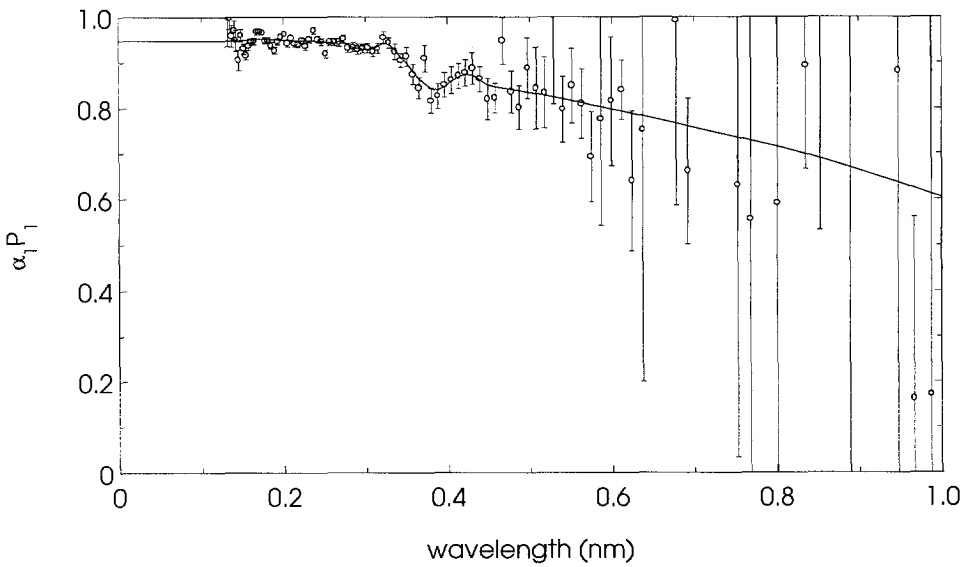

Figure 3.7: *Polarization grade of the ROG-beam as a function of wavelength, as calculated (open circles with error bars) from the calibration measurement. The line represents a spline, by which $\alpha_1 P_1$ is approximated in when correcting PNR-data for the polarization degree of the beam.*

can see that for wavelengths smaller than 0.35 nm the polarization is about 0.95. For higher values the polarization diminishes to values of about 0.8. In Figure 3.7

the spline used to correct the measured data when analysing experiments is given by the solid line.

Unfortunately the determined polarization has bad statistics for neutrons with wavelengths smaller than 0.13 nm or larger than 0.56 nm. In this wavelength region the Maxwell intensity is considerable smaller, so much longer measure time is needed to obtain considerable better accuracy. Another factor 3 in intensity was lost at the large wavelength side of the spectrum, because of the guide-field construction used to magnetize the third polarizer. A table was constructed on which the mirror on both sides was in contact with iron strips (see Figure 3.8). Ferroxdure magnets are attached to these strips to magnetize the mirror homogeneously. Neutrons hitting the iron strips will be absorbed. Therefore only neutrons with small divergence in the yz-plane will be detected and the accuracy with which the polarization is determined is reduced for neutrons with large wavelength.

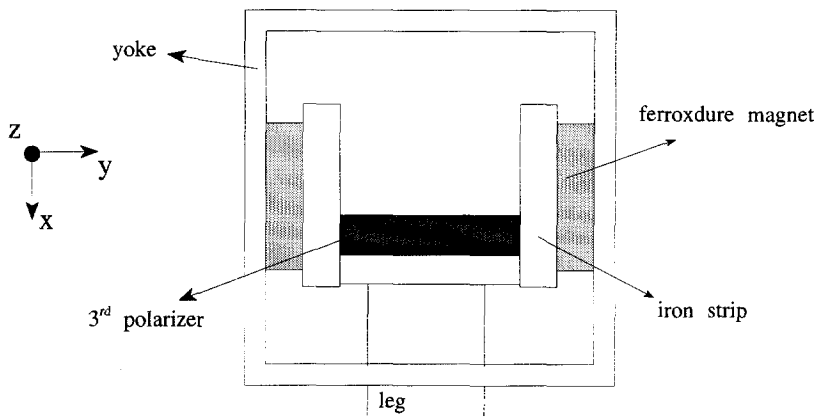

Figure 3.8: *Schematic view of the table supporting the third polarizing mirror during calibration of the incoming polarization.*

Nowadays ROG is supplied with a stacked vertical analyzing mirror system. This implies that the divergence in the yz-plane is no problem and the polarization of the incoming beam is recently determined more accurately. The newly calibrated polarization is in good agreement with the polarization given in Figure 3.7 [20]. Therefore the spline presented in Figure 3.7 seems to be a good approximation of the polarization of the beam.

3.4 Bulk Nickel Test Sample

As a rough check of the validity of the polarization calibration, the spin parallel and spin antiparallel neutron reflectivity curves of bulk nickel in an in-plane field of 480 kA/m have been measured. At such a large magnetic field the nickel should

be saturated. The angle of incidence is 8.1 mrad. The measured data are given in Figure 3.9, where one can see that the spin antiparallel data show a kink at q_{cr} of the spin parallel data. This is caused by the small fraction of spin parallel neutrons in the spin antiparallel beam due to the imperfection of the polarization.

A model is fitted to the data, which assumes that an oxide layer consisting of NiO is formed on the sample. The values of Γ_n of nickel and nickeloxide were kept constant at the bulk values: 0.0118 and 0.0109 nm^{-2} respectively. Only the thickness of the oxide layer and Γ_m were fitted. In this way for the thickness of the oxide layer the value 1.1 nm and for Γ_m the value 0.00174(3) nm^{-2} were found. This value for Γ_m corresponds with a magnetization of 476(8) kA/m. In the literature for M_s the value of 485 kA/m is given [21]. One sees that the difference is only 2 %, which is within the experimental error, giving confidence in the determined polarization degree. The result is especially good, realizing the considerable inaccuracy of the determined polarization in the region with λ smaller than 0.13 nm and larger than 0.56 nm. In Figure 3.9 also the reflectivity curves, assuming that the polarization is perfect, are given. One sees that the imperfection of the beam polarization has negligible influence on the spin parallel data. For the spin antiparallel data considerable differences appear for 0.10 nm $^{-1} < q < 0.14$ nm^{-1}. The influence is larger for the spin antiparallel data because the spin parallel data have a much larger reflectivity then the spin antiparallel data.

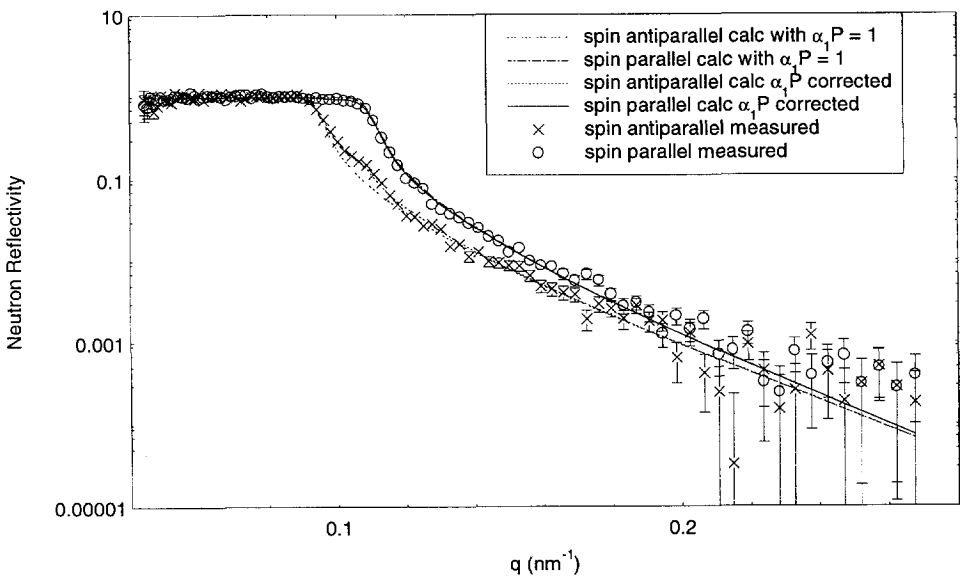

Figure 3.9: *Spin parallel and spin anti-parallel neutron reflectivity of bulk nickel in an in-plane field of 480 kA/m.*

Chapter 4

Data Analysis

4.1 Description of the Matrix Method

The PNR-experiments in this thesis will be interpreted using the matrix method [9], that is described in this section. One can distinguish two versions of the matrix method: the so-called interface—and the layer method. The advantage of the interface method, which will be explained first, is that roughness at interfaces can easily be modelled. A disadvantage of this model is that q, the x-component of the wave vector is not allowed to be zero. Using the layer method q is allowed to be zero.

As mentioned in chapter 2, neutrons obey the Schrödinger equation. The Schrödinger equation can be simplified to:

$$\nabla^2\Psi + (\vec{\mathbf{k}}^2 + \Gamma_0 - \Gamma)\Psi = 0, \tag{4.1}$$

where Ψ represents the wave function of the neutrons, $\vec{\mathbf{k}}$ their wave vector and Γ represents the potential energy multiplied by $2m_n/\hbar^2$, as experienced by the neutron beam. When $\Psi = \psi(x)\psi(y)\psi(z)$, Eqn. (4.1) for the x-direction can be written as:

$$\frac{\partial^2\psi}{\partial x^2} + q^2\psi(x) = 0, \tag{4.2}$$

with

$$q^2 = k_x^2 + \Gamma_0 - \Gamma\ . \tag{4.3}$$

In vacuum, in absence of a magnetic field, $q = k_x$, because $\Gamma_{n,vacuum} = 0$.

Using the interface method, one considers a perfect interface at $x = x_i$, between a material with Γ_i and one with Γ_{i+1}. For $x < x_i$ the solution of Eqn. (4.2) is given by:

$$\psi(x) = \alpha_i e^{iq_i x} + \beta_i e^{-iq_i x} \tag{4.4}$$

and for $x > x_i$:

$$\psi(x) = \alpha_{i+1} e^{iq_{i+1} x} + \beta_{i+1} e^{-iq_{i+1} x}\ . \tag{4.5}$$

At the interface ($x = x_i$) both ψ and $\partial\psi/\partial x$ have to be continuous. This can be used to calculate the values of α_{i+1} and β_{i+1}. Easily can be deduced:

$$\begin{pmatrix} \alpha_{i+1} \\ \beta_{i+1} \end{pmatrix} = \frac{1}{2}\begin{pmatrix} 1+\epsilon_i & 1-\epsilon_i \\ 1-\epsilon_i & 1+\epsilon_i \end{pmatrix}\begin{pmatrix} \alpha_i \\ \beta i \end{pmatrix} = \mathsf{m_s}\begin{pmatrix} \alpha_i \\ \beta i \end{pmatrix} \tag{4.6}$$

with $\epsilon_i = q_i/q_{i+1}$ and $\mathsf{m_s}$ representing a single interface. Eqn. (4.6) is not valid for $q_{i+1} = 0$. A limiting procedure turns out to yield rather complicated expressions. In practice several solutions may be applied to circumvent $q_{i+1} = 0$.

When Eqn. (4.6) is written with $\alpha_i = 1$, $\beta_i = r$ (the reflection amplitude), $\alpha_{i+1} = t$ (the transmission amplitude) and $\beta_{i+1} = 0$, one obtains:

$$r = \frac{\epsilon_i - 1}{\epsilon_i + 1}. \tag{4.7}$$

With the reflectivity R equal to rr^*, Eqn. (4.7) represents the Fresnel reflectivity as given by Eqn. (2.15).

In practice a single interface occurs very seldom and one has to deal with more complicated systems. These complicated systems are usually simplified by assuming them to consist of slabs with constant Γ. When $\Gamma = \Gamma_i$ for $x_i < x < x_{i+1}$, $\psi(x)$ in this interval is again given by:

$$\psi(x) = \alpha_i e^{iq_i(x-x_i)} + \beta_i e^{-iq_i(x-x_i)}. \tag{4.8}$$

Then one can impose boundary conditions ($\psi(x)$ and $\partial\psi(x)/\partial x$ are continuous) at the interface with the next region, where Γ is equal to Γ_{i+1} leading to the following relations between α_i, β_i, α_{i+1} and β_{i+1}:

$$\begin{pmatrix} \alpha_{i+1} \\ \beta_{i+1} \end{pmatrix} = \frac{1}{2}\begin{pmatrix} 1+\epsilon_i & 1-\epsilon_i \\ 1-\epsilon_i & 1+\epsilon_i \end{pmatrix}\begin{pmatrix} e^{iq_iT_i} & 0 \\ 0 & e^{-iq_iT_i} \end{pmatrix}\begin{pmatrix} \alpha_i \\ \beta i \end{pmatrix} = \mathsf{m_i}\begin{pmatrix} \alpha_i \\ \beta i \end{pmatrix}, \tag{4.9}$$

with $T_i = x_{i+1} - x_i$. When the impinging neutrons encounter more interfaces, matrices can be deduced in the same way. Therefore, a system containing more interfaces can be represented by the product of the matrices corresponding to the various interfaces. The matrix M representing a system containing n interfaces can be written as:

$$\mathsf{M} = \mathbf{m_n}...\mathbf{m_{i+1}}\mathbf{m_i}...\mathbf{m_1}\ . \tag{4.10}$$

Here $\mathsf{m_1}$ represents the surface of the system. The boundary conditions for the total system define $\alpha_0 = 1$, $\alpha_n = t$ (the transmission amplitude), $\beta_0 = r$ (the reflection amplitude) and $\beta_n = 0$. And again the reflectivity $R = rr^*$.

Roughness at interfaces affects the reflection and the transmission amplitudes of the wave function, resulting in changes in the measured specular reflection, and it causes also small angle scattering around the specular reflection, called off-specular reflection. The roughness at the interface $x = x_i$ can be approximated by a gradual change of Γ from Γ_i to Γ_{i+1} described by an error function of x/σ, with σ the roughness. The influence of such a gradual change on the specular reflectivity

can be taken into account by adapting the matrix $\mathsf{m_i}$ given in Eqn. (4.9) in the following way [22]:

$$\mathsf{m_i} = \frac{1}{2}\begin{pmatrix} (1+\epsilon_i)e^{q_i q_{i+1}\sigma^2} & (1-\epsilon_i)e^{-q_i q_{i+1}\sigma^2} \\ (1-\epsilon_i)e^{-q_i q_{i+1}\sigma^2} & (1+\epsilon_i)e^{q_i q_{i+1}\sigma^2} \end{pmatrix}\begin{pmatrix} e^{iq_iT_i} & 0 \\ 0 & e^{-iq_iT_i} \end{pmatrix} \tag{4.11}$$

Obviously this approximation of roughness at interfaces generates no off-specular reflection.

In the above method each interface is represented by a matrix. The so-called layer method defines matrices for each slab with constant Γ instead. Suppose a slab is defined by $\Gamma = \Gamma_i$ for $x_i < x \leq x_{i+1}$. Then neutrons in this slab obey the following Schrödinger equation 4.2:

$$\frac{\partial^2}{\partial x^2}\psi_i(x) + q_i^2\psi_i(x) = 0 \tag{4.12}$$

with, according to Eqn. (4.3):

$$q_i^2 = q_0^2 + \Gamma_0 - \Gamma_i \ . \tag{4.13}$$

Eqn. (4.12) can also be written as two coupled first order differential equations:

$$\frac{\partial}{\partial x}\psi_i(x) = \phi_i(x) \tag{4.14}$$

and

$$\frac{\partial}{\partial x}\phi_i(x) = -q_i^2\psi_i(x) \ . \tag{4.15}$$

The solutions of these equations for $x_i < x \leq x_{i+1}$ can be obtained from the continuity conditions of $\psi(x)$ and $\phi(x)$ at the boundaries of the slab. When the thickness of the slab is $T_i(= x_{i+1} - x_i)$:

$$\psi(x_{i+1}) = \psi_i\cos(q_iT_i) + \frac{\phi_i}{q_i}\sin(q_iT_i) \tag{4.16}$$

and

$$\phi(x_{i+1}) = \phi_i\cos(q_iT_i) - q_i\psi_i\sin(q_iT_i) \ . \tag{4.17}$$

Therefore, a slab with constant Γ can be represented as a matrix which gives the relation between ψ and ϕ at the boundaries of this slab:

$$\begin{pmatrix} \psi(x_{i+1}) \\ \phi(x_{i+1}) \end{pmatrix} = \begin{pmatrix} \cos(q_iT_i) & \dfrac{\sin(q_iT_i)}{q_i} \\ -q_i\sin(q_iT_i) & \cos(q_iT_i) \end{pmatrix}\begin{pmatrix} \psi(x_i) \\ \phi(x_i) \end{pmatrix} = \mathsf{m_i}\begin{pmatrix} \psi(x_i) \\ \phi(x_i) \end{pmatrix} \ . \tag{4.18}$$

The matrix $\mathsf{m_i}$ represents the influence of slab i on the wave propagation. It turns out that for $q_i \to 0$ the matrix corresponding to a linear wave function in slab i is

obtained. Again a more complicated system can be represented by multiplication of matrices.

The calculations presented in this thesis are all performed using the interface method. For this version of the matrix method was chosen because roughness can be defined very easily. To take the influence of the in-plane magnetization component perpendicular to the polarization direction into account the matrices have to be extended to 4×4 matrices, as is described by Felcher *et al.* [12].

4.2 Correction for the Degree of Polarization

The polarization of a neutron beam, P is defined by:

$$P = \frac{I^+ - I^-}{I^+ + I^-} \ . \tag{4.19}$$

In this equation I^+ represents the intensity of the neutrons with a positive component of their magnetic moment in the direction in which P is determined and I^- with a negative component of their magnetic moment in this direction.

When a beam is totally polarized, $|P|$ is equal to 1. This is usually not the case. Therefore the experimentally measured reflectivity, R_{exp} will be a mixture of the actual spin parallel and the spin antiparallel reflectivities, R^+ and R^- respectively:

$$R^+_{exp}(\lambda) = \frac{1+P(\lambda)}{2} R^+(\lambda) + \frac{1-P(\lambda)}{2} R^-(\lambda) \tag{4.20}$$

and

$$R^-_{exp}(\lambda) = \frac{1-P(\lambda)}{2} R^+(\lambda) + \frac{1+P(\lambda)}{2} R^-(\lambda) \ . \tag{4.21}$$

From these equations can easily be deduced that the actual value of R for both spin states can also be calculated from the experimentally observed values:

$$R^+(\lambda) = \frac{1+P(\lambda)}{2P(\lambda)} R^+_{exp}(\lambda) - \frac{1-P(\lambda)}{2P(\lambda)} R^-_{exp}(\lambda) \tag{4.22}$$

and

$$R^-(\lambda) = \frac{1+P(\lambda)}{2P(\lambda)} R^-_{exp}(\lambda) - \frac{1-P(\lambda)}{2P(\lambda)} R^+_{exp}(\lambda). \tag{4.23}$$

In chapters 5 through 8 usually R_{exp} is presented instead of R, with the fits to data averaged over R^+ and R^- according to Eqns. (4.20) and (4.21).

4.3 Influence of Divergence of the Neutron Beam

As described in section 3.1 ROG is equipped with neutron guides to maximize the flux of neutrons that hit the sample. These neutron guides are 30 mm wide. The last neutron guide ends just before the monitor. The distance between this last

neutron guide and the sample is 495 mm. Over this distance the neutron beam diverges, depending on the wavelength of the neutrons. The neutron guides are coated with ^{58}Ni that has a critical angle of reflection $\alpha = 20$ mrad/nm. It is assumed that at the end of the neutron guide at each point of the beam, the angular distribution in the yz−plane is homogeneous between −20 and 20 mrad/nm, corresponding to the critical angle of ^{58}Ni.

For the configuration considered here these assumptions lead to a trapezium shape of the intensity of the neutrons as a function of y. In Figure 4.1 half of the trapezium at the position of the sample is given. For ROG the intensity at the middle of the sample for $|y| < |\frac{w}{2} - \alpha\lambda L|$ is constant, for wavelengths $\lambda < 1.5$ nm, which is the maximum wavelength of the available spectrum.

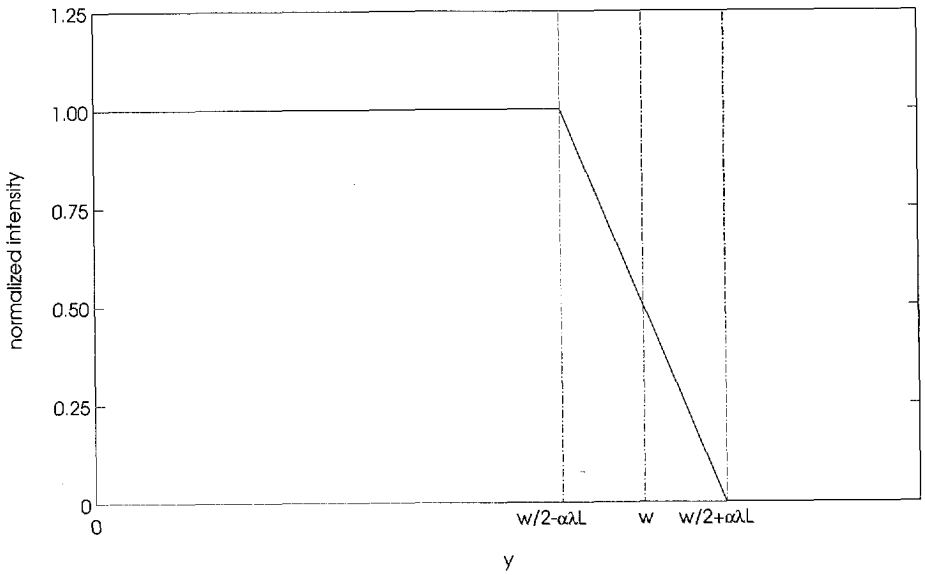

Figure 4.1: *Neutron intensity on the sample for one wavelength normalized to the intensity at y=0.*

In general with w the width of the neutron guide and L the distance between the end of the neutron guide and the sample, the intensity for each wavelength, normalized to the intensity at $y = 0$, is given by:

$$i_\lambda(y) = \begin{cases} 1 & 0 < 2y < |w - 2\alpha\lambda L| \\ 1 - \dfrac{2y - |w - 2\alpha\lambda L|}{w + 2\alpha\lambda L - |w - 2\alpha\lambda L|} & |w - 2\alpha\lambda L| < 2y < w + 2\alpha\lambda L \\ 0 & w + 2\alpha\lambda L < 2y \end{cases} \tag{4.24}$$

The total intensity for a certain wavelength on a sample with width s in the y-direction is proportional to:

$$I_\lambda(s) = 2\int_0^{\frac{1}{2}s} i_\lambda(y)dy \ , \tag{4.25}$$

which yields explicitly

$$I_\lambda(s) = \begin{cases} s & 0 < s < |w - 2\alpha\lambda L| \\ s - \dfrac{(s - |w - 2\alpha\lambda L|)^2}{2(w + 2\alpha\lambda L - |w - 2\alpha\lambda L|)} & |w - 2\alpha\lambda L| < s < w + 2\alpha\lambda L \\ \dfrac{w + 2\alpha\lambda L + |w - 2\alpha\lambda L|}{2} & w + 2\alpha\lambda L < s \end{cases} \tag{4.26}$$

The measured reflectivity has to be multiplied by $(w+2\alpha\lambda L+|w-2\alpha\lambda L|)/2I_\lambda(s)$ to be compatible with the intensity measured in the monitor.

4.4 Other Corrections

Neutron reflectivity data measured on ROG are usually corrected with the program ROGCOR on the data storage VMS workstation. This program determines the wavelength corresponding to each time channel, it corrects for a time independent background, dead time and efficiency for both monitor and detector, it corrects for the wavelength-dependent transmission of the monitor and it corrects for the absorption and scattering in the flight path between monitor and detector. This program also divides wavelength-dependent the neutrons counted by the detector by the neutrons counted by the second monitor, to obtain the reflectivity. Detailed descriptions of these corrections are given in [13].

The angle at which a certain reflectivity experiment is performed is calculated from the position of the detector with respect to the sample. The angle θ is given by the following formula:

$$\theta = \arctan(\frac{h}{2D}) \approx \frac{h}{2D} \ , \tag{4.27}$$

where h is the height of the detector above the incoming neutron beam and D is the distance between the sample and the detector measured along the neutron beam. The largest possible systematic error because of inaccurate alignment and determination of D and h is estimated to be 5 %.

As in this thesis, usually samples are used that are smaller (in the z-direction) than the footprint of the neutron beam at the sample position, the region of total reflection can only be recognized as a q-region in which the neutron reflectivity is constant. Therefore the measured data are normalized to the reflectivity in this region.

4.5 Influence of Improper Degree of Polarization

To correct measured polarized neutron reflectivity data for the imperfection of the polarization, the polarization grade $P(\lambda)$ has to be known. Usually the polarization grade as a function of wavelength is calibrated once for an apparatus and used in the interpretation of all experiments performed on this apparatus. One method to calibrate the polarization of the apparatus is the 3P2S-method described in section 3.2. On the TOF-neutron reflectometer CRISP of ISIS at the Rutherford Appleton Laboratory (UK) the polarization of the spin parallel and spin antiparallel beam was determined by another method using a polarizing mirror identical to the one standard used at CRISP and polarization analysis [23, 24].

Using this polarization calibration to correct experimental data measured on CRISP on a Co-Cr sample at a magnetic field of 573 kA/m (further description in chapter 5) resulted in negative values for R^- for six q-values around 0.065 nm^{-1}. Apparently P was more perfect than resulted from the calibration. In Figure 4.2 the obtained positive values of R^- and R^+ after polarization correction are given.

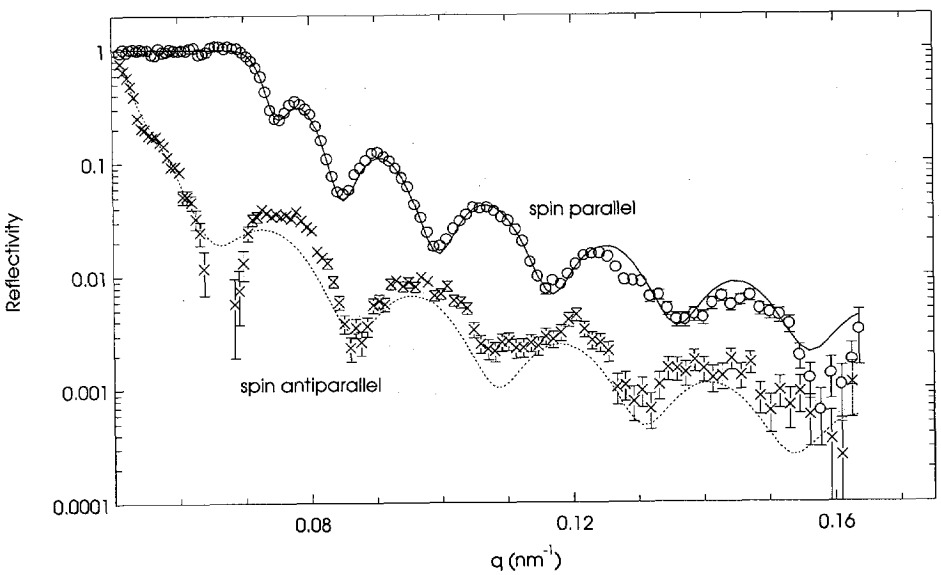

Figure 4.2: *Neutron reflectivity of the Co-Cr sample for the two spin states, described in chapter 5, together with best fit, assuming only one slab with constant* Γ_n *and* Γ_m.

As negative R values are physically impossible, concern has risen about the effect of an improperly calibrated $P(\lambda)$ on the interpretation of measured polarized neutron reflectivity data. To gain insight into the effect of a polarization correction based on an improperly calibrated $P(\lambda)$, a model study was performed. In

this model different polarization degrees are chosen by purpose to simulate experimentally obtained data, while in the interpretation of these simulated data the polarization was supposed to be perfect. Comparison of the obtained fitted parameters for different chosen P-values, gives insight in the influence of the deviation of P.

As a starting point for this model study, the measurement presented in Figure 4.2 is taken. To mimic reality in a simple way, a model assuming only one slab with constant Γ_n and Γ_m is fitted to the measurement in Figure 4.2. In Figure 4.2 this fit is given by the lines. The obtained model, for which the values of the different parameters are given in Table 4.1, is used to calculate reflectivities. The roughness at the interfaces is represented by σ. The resolution $\Delta q/q$ was kept constant at 5 % in this model study.

The reflectivity, R, corresponding to the parameters presented in Table 4.1, is calculated using the matrix method at the same q-values for which the reflectivity was measured. We assumed that the relative error on R is equal to the experimentally determined relative error (see Figure 4.2), $\Delta R_{exp}/R_{exp}$. For the six points which are omitted in Figure 4.2, we assumed the relative error to be of the same magnitude as the points at slightly smaller and larger q. Note that the relative error is used only as a weight factor in the fit procedure and should not be confused with the statistical inaccuracy of the model data.

Although in practice the polarization P will be λ-dependent when a polychromatic beam is used, for simplicity P is supposed to be constant in this model study. Three cases are considered: $P = 0.90$, 0.94 and 0.96 for both spin states. The simulated reflectivity R_{mix} for polarization P is calculated using Eqns. (4.20) and (4.21): the imperfection of the beam polarization is supposed to be equally large for both spin states. The obtained data sets for the three P-values are given in Figure 4.3.

The errors in R^+_{mix} and R^-_{mix} are obtained by weighted averaging over the errors in R^+ and R^- in the same way as for the data itself (see Eqns. (4.20) and (4.21)).

From Figure 4.2 and Figure 4.3 it is clear that R^+_{mix} is almost the same as R^+ for the three considered values of P, while R^-_{mix} differs largely from R^-. The disagreement between R^-_{mix} and R^- increases rapidly with the deviation of P from 1. The reflectivity for spin parallel is in this case much less sensitive to the polarization degree because the spin antiparallel reflectivities are about one order of magnitude smaller than the spin parallel reflectivities.

The simulated data R^+_{mix} and R^-_{mix} are fitted, using two different sets of start parameters, ignoring the deviation from perfect polarization. Set A contains the values used to calculate R, set B contains arbitrary start parameters for the fit. Both sets of start parameters are given in Table 4.1. The obtained values of the parameters corresponding to these fits are given in Table 4.2 and 4.3. From these tables it is clear that the values of the start parameters do not influence the obtained minimum considerably in the present case. The lines in Figure 4.3 correspond to the fits obtained when starting with set B.

Figure 4.3 shows clearly that in the considered cases, the best obtained fit

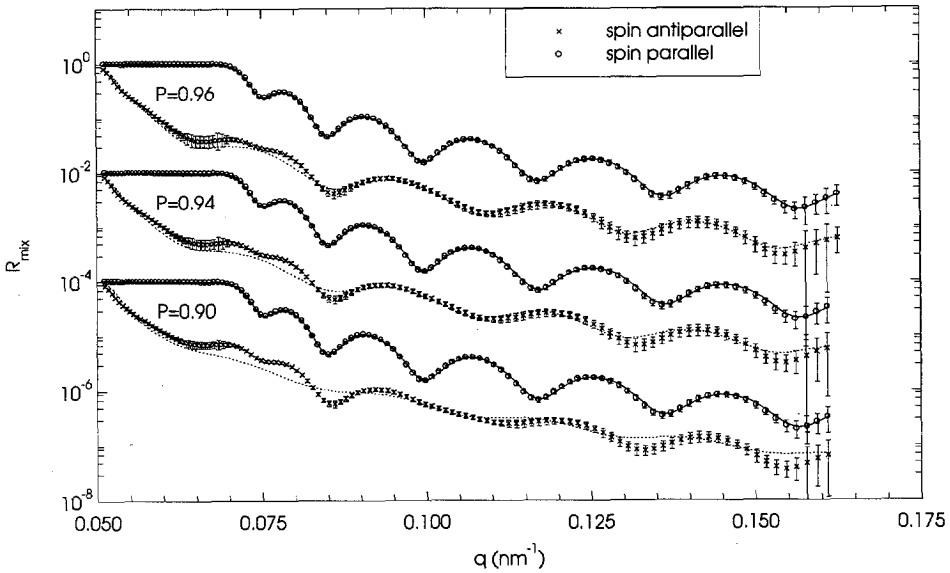

Figure 4.3: *Simulated reflectivity data, for a polarization of 0.96, 0.94 and 0.90. Data for $P = 0.94$ and $P = 0.90$ are offset for clarity. The lines correspond to the fits obtained by using start parameter set B.*

can not describe R^-_{mix} satisfactorily. The badness of fit to the antiparallel data increases when the deviation of perfect polarization increases. On the contrary the fit to the spin parallel data describes R^+_{mix} very well for the three values of P. In Table 4.2 and 4.3 also the parameter dev^2 is given, which is a measure of the quality of the fit and is defined as:

$$dev^2 = \sum_{i=1}^{N} \frac{(R_{fit,i} - R_{mix,i})^2}{N(\Delta R_{mix,i})^2}, \tag{4.28}$$

with $R_{fit,i}$ the reflectivity value calculated for the model, $R_{mix,i}$ the simulated reflectivity value with error $\Delta R_{mix,i}$, N the total number of data points. The value dev^2_{tot} takes all the points (parallel and antiparallel spin) into account, $(dev^{+(-)})^2$ takes only the spin (anti)parallel data into account. The quality of fit is better when dev^2 is smaller. The difference between $(dev^+)^2$ and $(dev^-)^2$ also reflects the fact that the spin parallel curve is fitted much better than the spin antiparallel curves.

In this case the value of $\Gamma_{Co-Cr,magnetic}$ increases when P deviates more from 1. However, the sum of $\Gamma_{Co-Cr,magnetic}$ and $\Gamma_{Co-Cr,nuclear}$, to which the spin parallel data are sensitive, remains almost constant. The obtained minimum seems to be determined predominantly by R^+_{mix} with much better statistical accuracy than R^-_{mix}.

The fitted value of the Co-Cr layer thickness is not influenced considerably

Table 4.1: *Start parameters used in the model study to the influence of incorrect polarization calibration and the influence of statistical errors. Set A corresponds to the assumed model.*

parameter	values set A	values set B
$\Gamma_{substrate}$	$2.648 \times 10^{-3}\text{nm}^{-2}$	$2.800 \times 10^{-3}\text{nm}^{-2}$
$\Gamma_{Co-Cr,nuclear}$	$2.917 \times 10^{-3}\text{nm}^{-2}$	$2.200 \times 10^{-3}\text{nm}^{-2}$
$\Gamma_{Co-Cr,magnetic}$	$2.082 \times 10^{-3}\text{nm}^{-2}$	$1.400 \times 10^{-3}\text{nm}^{-2}$
d_{Co-Cr}	135.836 nm	120.00 nm
$\sigma_{surface}$	0.797 nm	0.000 nm
$\sigma_{substrate}$	0.000 nm	0.000 nm

by the polarization. For $P = 0.90$, the best obtained fit results in a decrease of $\Gamma_{Co-Cr,nuclear}$ of 10 % and an increase of $\Gamma_{Co-Cr,magnetic}$ of 13 %.

Although the values of the fitted parameters do not differ very much for the different assumed P-values, the fact that no satisfactory fit to the data for both spin states can be obtained will in practice give rise to doubts on the meaning of the obtained minimum and the possible existence of another minimum, when P is improperly calibrated.

In this case the spin antiparallel data are much more sensitive to improper polarization correction because the antiparallel data exhibit a much smaller reflectivity than the spin parallel data. The curve with smaller reflectivity is more sensitive to the polarization correction and also is often measured with worse statistics than the other curve.

In general one can say that the fact that dev^2 for the curve with much smaller reflectivity is much larger than for the curve of the opposite spin state, indicates that the polarization correction contains errors.

4.6 Influence of Statistical Errors

As the neutron reflectivity decays proportional to $(q - q_{cr})^{-4}$, it is difficult to measure reflectivity data accurately over a large q-range. Therefore also a model study is done to investigate the influence of statistical accuracy. This model study is also based on the experimental data presented in Figure 4.2 and $R(q)$ is calculated for the parameters of set A given in Table 4.1. To $R(q)$ simulated statistical accuracy is added, using the relative error of the data points presented in Figure 4.2, $\Delta R_{exp}/R_{exp}$:

$$R_{st}(q) = R(q)\left(1 + \eta(q)\frac{\Delta R_{exp}(q)}{R_{exp}(q)}\right) . \tag{4.29}$$

Here $\eta(q)$ is a random number from a standard normal distribution around 0. This calculation was performed for three different series of random values $\eta(q)$, to show a possible influence of the particular used series $\eta(q)$.

Table 4.2: *Fitted parameters obtained by using start parameter set A to simulated reflectivity data with non-perfect polarization.* $\Gamma_{Co-Cr,p}$ *is the sum of* $\Gamma_{Co-Cr,nuclear}$ *and* $\Gamma_{Co-Cr,magnetic}$. Γ *is given in* 10^{-3} nm^{-2} *and* T *and* σ *in nm.*

parameter	start value	$P = 0.96$	$P = 0.94$	$P = 0.90$
$\Gamma_{substrate}$	2.648	2.693	2.704	2.742
$\Gamma_{Co-Cr,nuclear}$	2.917	2.818	2.755	2.637
$\Gamma_{Co-Cr,magnetic}$	2.082	2.174	2.237	2.358
$\Gamma_{Co-Cr,p}$	4.999	4.992	4.992	4.995
T_{Co-Cr}	135.836	135.438	135.177	135.412
$\sigma_{surface}$	0.797	0.426	0.006	0.000
$\sigma_{substrate}$	0.000	0.000	0.000	0.000
dev^2_{tot}		1.34	2.70	6.05
$(dev^+)^2$		0.12	0.32	0.22
$(dev^-)^2$		2.55	5.08	11.89

Table 4.3: *Fitted parameters obtained by using start parameter set B to simulated reflectivity data with non-perfect polarization.* $\Gamma_{Co-Cr,p}$ *is the sum of* $\Gamma_{Co-Cr,nuclear}$ *and* $\Gamma_{Co-Cr,magnetic}$. Γ *is given in* 10^{-3} nm^{-2} *and* T *and* σ *in nm.*

parameter	start value	$P = 0.96$	$P = 0.94$	$P = 0.90$
$\Gamma_{substrate}$	2.800	2.692	2.703	2.742
$\Gamma_{Co-Cr,nuclear}$	2.200	2.825	2.760	2.637
$\Gamma_{Co-Cr,magnetic}$	1.400	2.171	2.236	2.358
$\Gamma_{Co-Cr,p}$	3.600	4.996	4.996	4.995
T_{Co-Cr}	120.00	135.112	135.009	135.412
$\sigma_{surface}$	0.000	0.440	0.137	0.000
$\sigma_{substrate}$	0.000	0.000	0.000	0.000
dev^2_{tot}		1.41	2.77	6.05
$(dev^+)^2$		0.41	0.55	0.22
$(dev^-)^2$		2.42	4.99	11.89

To these simulated data, we fitted a model using the two sets A and B as start parameters (see Table 4.1). The simulated reflectivity data $R_{st}(q)$ are given in Figure 4.4 together with the obtained fits when started with set B for the start parameters. For each set of start parameters the obtained parameter values are presented in Table 4.4 and 4.5.

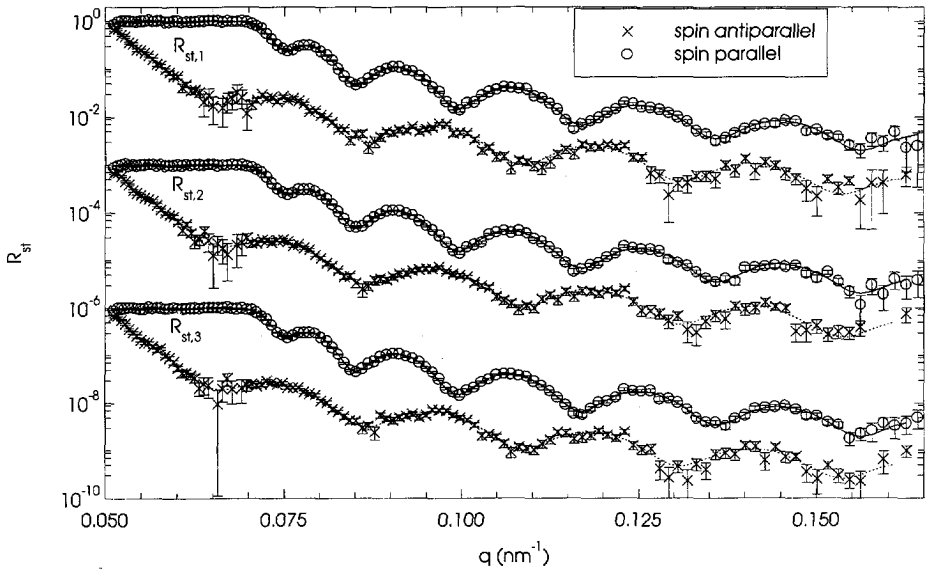

Figure 4.4: *$R_{st,1}$, $R_{st,2}$ and $R_{st,3}$ as a function of q to study the influence of statistical errors. Data for $R_{st,2}$ and $R_{st,3}$ are offset for clarity. The lines represent the calculated reflectivity for start parameters set B.*

Table 4.4 and 4.5 show that adding a statistical error to R, only changes the fitted value for roughness at the interfaces a little. The other parameters do not differ considerably. In Table 4.4 and 4.5 χ^2_{tot} is defined as follows:

$$\chi^2_{tot} = \sum_{i=1}^{N} \frac{(R_{fit,i} - R_{st,i})^2}{(N-p)(\Delta R_{st,i})^2}, \tag{4.30}$$

with $R_{fit,i}$ the reflectivity value calculated for the model, $R_{st,i}$ the simulated reflectivity value with error $\Delta R_{st,i}$, N the total number of data points and p the number of fitted parameters. Eqn. (4.30) is also used in chapter 5 through 8 as a measure of the quality of the fit to experimentally obtained values. In that case R_{st} and ΔR_{st} are substituted by the experimentally obtained values.

The spin parallel and spin antiparallel data are fitted simultaneously and χ^2_{tot} as presented in Table 4.4 and 4.5 is a measure for the quality of fit taking the data with both spin states into account. The quality of fit is best when χ^2_{tot} equals 1. During data simulation and fitting R_{st} the polarization is supposed to be perfect. As it is interesting to look at the quality of fit of the data with the two spin states

Table 4.4: *Fitted parameters obtained by using start parameter set A to simulated reflectivity data.* Γ *is given in* 10^{-3} nm^{-2} *and* T *and* σ *in nm. The parameter* $s(\eta)$ *represents the standard deviation in* η.

parameter	start value	value fit to $R_{st,1}$	value fit to $R_{st,2}$	value fit to $R_{st,3}$
$\Gamma_{substrate}$	2.648	2.644	2.640	2.641
$\Gamma_{Co-Cr,nuclear}$	2.917	2.915	2.904	2.914
$\Gamma_{Co-Cr,magnetic}$	2.082	2.082	2.093	2.090
T_{Co-Cr}	135.863	135.821	135.782	135.888
$\sigma_{surface}$	0.797	0.793	0.667	0.801
$\sigma_{substrate}$	0.000	0.000	0.834	0.522
$s(\eta)_+$		1.18	1.35	1.06
$s(\eta)_-$		1.38	0.84	1.19
χ^2_{tot}		1.26	1.09	1.10
$(dev^+)^2$		1.16	1.35	1.03
$(dev^-)^2$		1.35	0.83	1.16

Table 4.5: *Fitted parameters obtained by using start parameter set B to simulated reflectivity data.* Γ *is given in* 10^{-3} nm^{-2} *and* d *and* σ *in nm. The parameter* $s(\eta)$ *represents the standard deviation in* η.

parameter	start value	value fit to $R_{st,1}$	value fit to $R_{st,2}$	value fit to $R_{st,3}$
$\Gamma_{substrate}$	2.800	2.639	2.646	2.641
$\Gamma_{Co-Cr,nuclear}$	2.200	2.919	2.915	2.914
$\Gamma_{Co-Cr,magnetic}$	1.400	2.081	2.077	2.090
d_{Co-Cr}	120.00	135.826	135.825	135.888
$\sigma_{surface}$	0.000	0.697	0.653	0.801
$\sigma_{substrate}$	0.000	0.698	0.823	0.522
$s(\eta)_+$		1.18	1.35	1.06
$s(\eta)_-$		1.38	0.84	1.19
χ^2_{tot}		1.25	1.11	1.10
$(dev^+)^2$		1.16	1.39	1.03
$(dev^-)^2$		1.35	0.83	1.16

separately, also $(dev^+)^2$ and $(dev^-)^2$ are given in Tables 4.4 and 4.5. Eqn. (4.28) with R_{st} substituted for R_{mix} is used to calculate the value of $(dev^+)^2$ and $(dev^-)^2$. Since the number of parameters to be fitted is much smaller than the number of data points one can roughly assume that the quality of fit is best when $(dev^+)^2$ and $(dev^-)^2$ in Tables 4.4 and 4.5 equal 1. Note that $(dev)^2$ has almost the same values as the standard deviation $s(\eta)$ for the different data sets, indicating that the value of χ^2 is only determined by the added statistical error. From Tables 4.4 and 4.5 it is clear that statistical errors of the magnitude considered here do not influence the interpretation of the measured data considerably.

Chapter 5

PNR on Co-Cr

5.1 Interest in Co-Cr

Since the introduction of both perpendicular recording and Co-Cr as a suitable medium for perpendicular recording by Iwasaki in 1977 [25], research has been performed on the use of Co-Cr layers for perpendicular recording. An overview is given by Lodder [26].

Sputtered layers of Co-Cr contain magnetic particles separated by non-magnetic material. These local differences in magnetic properties are caused by variations in the Cr-concentration with position. For example, the chromium concentration tends to be higher at grain boundaries, causing these regions to be non-magnetic. The presence of magnetic regions separated by non-magnetic material makes these layers suitable for high density recording, as they favour small transition lengths between domains representing bits with opposite magnetization direction.

Sputtering Co-Cr without seed layer, results in a columnar structure with the length direction of the columns, to which the easy axis of magnetization is parallel, perpendicular to the layer surface. This columnar structure is more perfect on the topside of the sample, while smaller particles with random orientation of the easy axis of magnetization appear at the substrate side. Apparently the particles with perpendicular anisotropy are more favourable, as the angular spread in easy axis distribution decreases with increasing thickness of the Co-Cr layer. The columnar structure is shown schematically in Figure 5.1.

The interest in perpendicular media has its origin in the idea that in perpendicular recording less area per bit should be needed. The bit density presently expected for hard disk applications in the year 2000 is 10 Gbits/inch^2. The theoretically predicted maximum bit density possible with perpendicular recording on Co-Cr is 25 Gbits/inch^2 [27].

Nowadays layers of Co-Cr-X are used for longitudinal magnetic recording in computer hard disks. By growing the Co-Cr-X layers on a chromium seed layer, the hexagonal Co-structure is favoured to have the c-axis or magnetic easy axis in-plane. The third component X can be Ni, Pt, Ta or C.

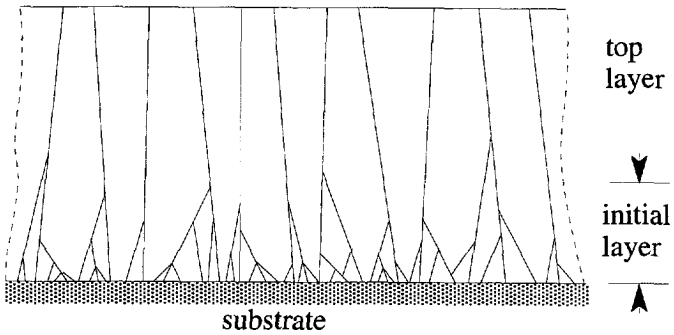

Figure 5.1: *Schematic view of structure of a Co-Cr layer suitable for perpendicular recording.*

As mentioned above, variations in the chromium concentration with position change the magnetic properties of the Co-Cr layer locally. As the structure of the layer changes with depth, the arrangement of the chromium atoms probably also changes with depth. Two possible models describing the compositional changes in a Co-Cr layer are proposed [28]. One model assumes the chromium to diffuse to the edges of each column. The other model, the so-called chrysanthemum-like model assumes also compositional variations in the column itself [29]. For both models the grain size is an important parameter. Since the grain size changes with depth, magnetic properties like M_s can also change with depth.

As a result of the growth mechanism the easy axis of a Co-Cr layer will rotate from more random at the substrate side towards perpendicular at the topside of this layer. The part of the Co-Cr layer at the substrate side exhibiting a more random easy axis of magnetization is called 'initial layer' [28]. By performing polarized neutron reflectometry the in-plane magnetization in the Co-Cr layer, as a function of depth, can be quantified.

5.2 Description of the Experiments

A rf sputtered layer of Co_{81}-Cr_{19} on silicon was obtained from MESA Research Institute at the Twente University. The thickness as determined from sputter time and sputter velocity calibration is 160 nm.

In November 1992 the polarized neutron reflectivity of the Co-Cr layer as a function of q of the sample was measured on CRISP, the time-of-flight reflectometer of ISIS at the Rutherford Appleton Laboratory. The Co-Cr layer was first saturated by a negative in-plane magnetic field. After that PNR-experiments were performed at an in-plane magnetic field of sequentially 3, 18, 36, 108, 248, 573, 36 and 21 kA/m. The angle of incidence was 5 mrad.

This angle was chosen to obtain PNR-data for a q-region of total reflection at

the lowest field. A region of total reflection was needed, to normalize the data, as the footprint of the neutron beam at the sample position was larger than the sample itself. As the spin parallel and antiparallel data for each magnetic field value are normalized by the same factor, the total reflection region of the spin parallel data can be used to determine the normalization constant of the spin antiparallel data. Also in the other chapters of this thesis, the angle of incidence is chosen such that a q-range of total reflection is measured.

In July 1996 neutron reflectivity data of the sample were also measured on ROG, the time-of flight reflectometer of IRI, in a magnetic field of 560 kA/m perpendicular to the sample surface. To obtain a perpendicular magnetic field the device shown in Figure 3.5 has been used. During this measurement a non-polarized beam was used. The angle of incidence was 6 mrad.

SEM-pictures were obtained of the sample. They were obtained in cross section and top view. The magnetization curve of the sample was measured by VSM.

5.3 Results and Interpretation PNR-Data

In Figure 5.2 the spin parallel and antiparallel neutron reflectivity data are given together at magnetic field values of 3, 18 and 573 kA/m as examples. The data as presented are not corrected for the polarization degree. At a magnetic field of 3 kA/m, q_{cr} of the spin parallel data is smaller than of the spin antiparallel data. This indicates that the overall magnetization of the sample is negative.

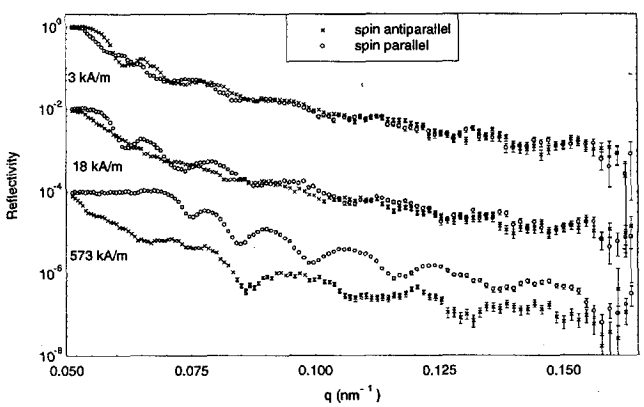

Figure 5.2: *Measured and simulated neutron reflectivities of the Co-Cr film with spin parallel and spin anti-parallel at various magnetic fields. For clarity the data measured at different magnetic fields are divided by increasing powers of hunderd.*

At 18 kA/m for most q-values the spin parallel data have higher intensity than the spin antiparallel data, indicating the overall magnetization to be positive. At higher magnetic fields the difference between spin parallel and spin antiparallel data increases due to the increasing magnetization.

The measured spin (anti)parallel neutron reflectivity curves at all considered magnetic fields are given in Figure 5.3a(b). In this figure the presented data are also not corrected for the polarization degree. Figure 5.3a clearly shows the increase of q_{cr} of R^+ with the applied magnetic field of 3 up to 573 kA/m. The

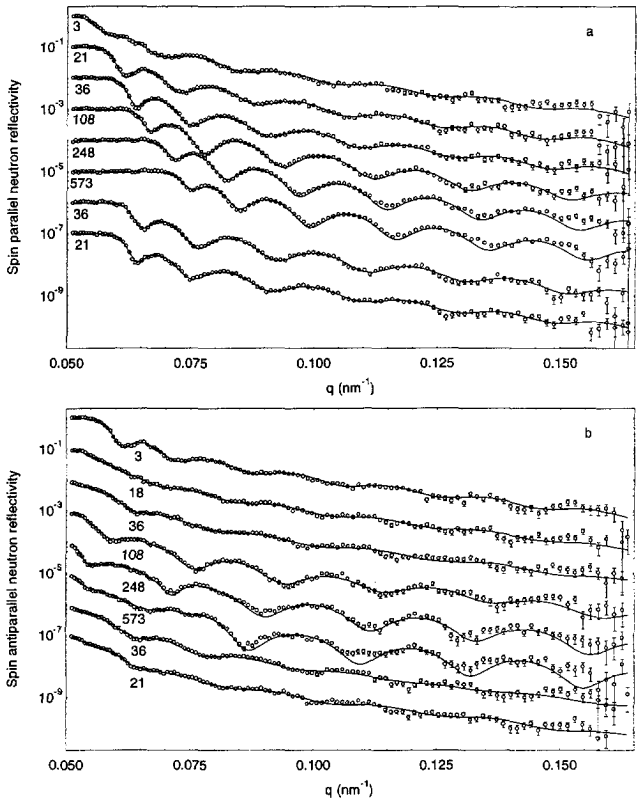

Figure 5.3: *Measured (circles) and simulated (lines) neutron reflectivities of the Co-Cr film with spin parallel (Figure 5.3a) and spin anti-parallel (Figure 5.3b). For clarity the data measured at different magnetic fields are divided by increasing powers of ten. The figures below each curve represent the magnitude of the applied in-plane magnetic field in kA/m.*

expected decrease of q_{cr} for the spin antiparallel data (Figure 5.3b) is less clear, because no reflectivities for q-values smaller than 0.05 nm^{-1} were measured. The measurement of the Co-Cr layer in a perpendicular field of 560 kA/m is given in Figure 5.4.

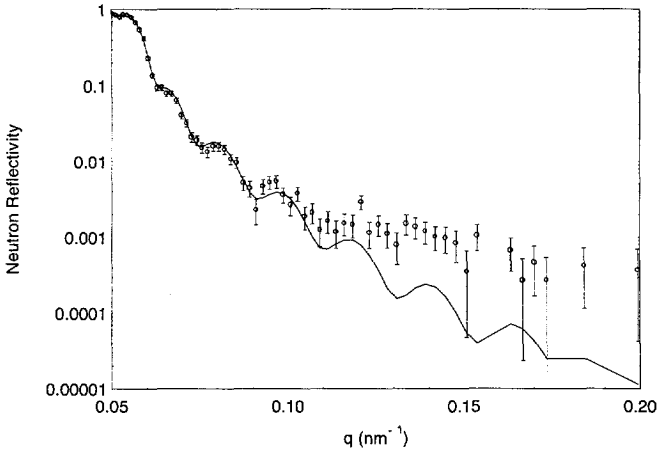

Figure 5.4: *Measured (circles) and simulated (lines) neutron reflectivity of the Co-Cr layer in a perpendicular magnetic field of 560 kA/m.*

5.3.1 Correction for the Polarization Degree

The PNR-data measured on CRISP have to be corrected for the imperfectness of the polarization of the beam. CRISP is supplied with a Drabkin two-coil non-adiabatic spin flipper [30] which only operates for the spin antiparallel state. This implies that only the spin antiparallel neutrons experience depolarization caused by this spin flipper. In this case the experimentally measured reflectivity does not depend on the theoretical reflectivity as given by Eqns. (4.20) and (4.21) but by:

$$R^{+}_{exp} = \frac{1+P}{2}R^{+} + \frac{1-P}{2}R^{-} \tag{5.1}$$

and

$$R^{-}_{exp} = \frac{1+\epsilon P}{2}R^{+} + \frac{1-\epsilon P}{2}R^{-} \tag{5.2}$$

with P the polarizing power of the mirror used to polarize the beam and ϵ defined as:

$$\epsilon = 1 - 2f, \tag{5.3}$$

where f is the efficiency of the spin flipper, i.e. the fraction of neutrons with their spins reversing to the opposite direction when passing the spin flipper. In Eqns. (5.1) and (5.2), R^{+} and R^{-} resemble the theoretical spin parallel and spin antiparallel reflectivity. For an ideal flipper f is equal to 1 and ϵ to -1.

The polarization degree of the CRISP beam impinging on the sample was calibrated by putting a second polarizing mirror on the sample position. This mirror was identical to the one used standard on CRISP to polarize the beam. In this configuration four intensities were measured as a function of wavelength: the reflected intensity with spin flipper on and off and the reflected intensity travelling

through a depolarizing shim with spin flipper on and off [23]. From those four intensities P and also f can be determined. Using this calibration P was estimated to be 0.976 independent of wavelength, and for f the following relation published in February 1992, f_{92} [24], was obtained:

$$f_{92} = 0.95575 + 3.4251 \times 10^{-3}\lambda - 8.5781 \times 10^{-4}\lambda^2 \ , \tag{5.4}$$

with λ the wavelength in nanometers. In Figure 5.5, f_{92} as a function of q is given for the angle of 5 mrad used in this experiment.

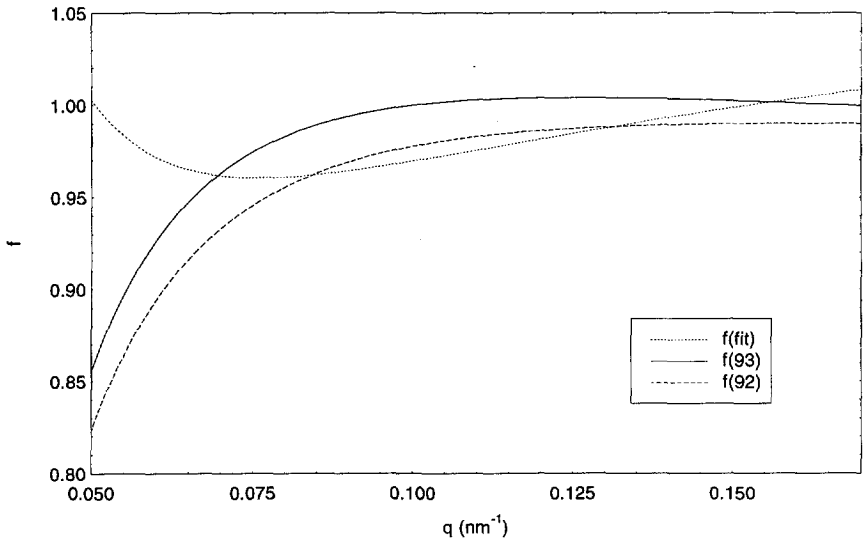

Figure 5.5: *The relation between the flipper efficiency f and q at the angle of incidence of 5 mrad used on the Co-Cr sample, according to the calibration in February 1992 (f_{92}), the calibration published in April 1993 (f_{93}) and as obtained by fitting a polynomial, (f_{fit}). The relation $q = 2\pi \sin\theta/\lambda$ with $\theta = 5$ mrad is used to calculate the dependence of the flipper efficiency on q.*

Using Eqn. (5.4) to calculate the actual reflectivities for both spin states, resulted in negative spin antiparallel reflectivity at the highest magnetic fields for $q \sim 0.065$ nm^{-1}. At the magnetic field of 573 kA/m R^+_{exp}/R^-_{exp} amounted to more than 25 in this q-range. Therefore, this measurement was extremely sensitive to the calibration of P. As negative values of R^- are impossible, it was difficult to interpret the measured data.

To circumvent the negative values of R^-, the q-dependence of f was fitted together with the model to the PNR-data measured at the highest field. This resulted in the function f_{fit} as given in Figure 5.5. The PNR-data measured on CRISP at the different field values were fitted simultaneously using f_{fit} for the flipper efficiency, resulting in the profiles of Γ_n and Γ_m given by the solid line in Figure 5.6 and published in [31].

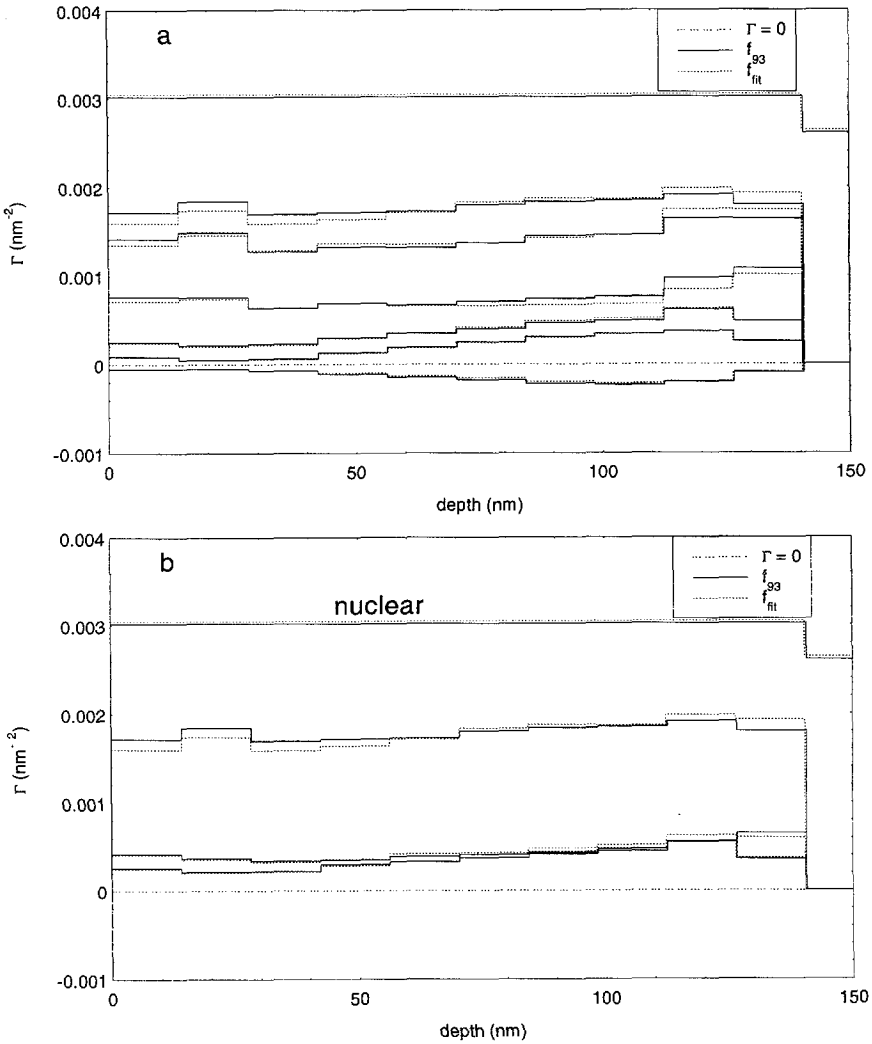

Figure 5.6: *The model fitted to the PNR-data assuming f_{fit}(solid lines) and f_{93}(dashed lines) for the flipper efficiency. The magnetic profiles for increasing(decreasing) magnetic field values are given in figure a(b). For magnetic field values see Figure 5.7.*

In 1993 a commissioning note on the polarization degree of CRISP [32] appeared with an improved calibration of the flipper efficiency, denoted f_{93}:

$$f_{93} = 0.939 + 0.051\lambda - 0.01\lambda^2. \tag{5.5}$$

In Figure 5.5 $f_{93}(q)$ is also given.

For values of $q \sim 0.065$ nm^{-1}, using f_{92} negative values for R^- were obtained. This is caused by overcorrecting the measured data for the imperfectness of the beam polarization: f_{92} is an underestimate of the flipper efficiency. This can also be seen in Figure 5.5: for $q \sim 0.065$ nm^{-1}, f_{fit} and f_{93} both are closer to 1 than f_{92} so they represent a more ideal spin flipper than f_{92}.

To check whether our interpretation of the data was right, the model was fitted again to the data using f_{93}. The difference in χ^2 of both fits is very small: use of f_{fit} led to χ^2 of 3.83 and use of f_{93} to a value of 3.81 for χ^2. Apparently the used fitting procedure did not succeed in finding the minimum that gave χ^2 equal to 3.81. This might be due to the fact that f_{fit} was obtained by fitting the data measured at the highest field only. The obtained model using f_{93} is given by the dashed line in Figure 5.6.

From Figure 5.6 it can be concluded that small deviations in the flipper efficiency used, do not influence the tendency of the model very much. However, at the highest field f_{93} results in a less steep increase of Γ_m with depth than f_{fit}. Apparently in the considered case with the Drabkin flipper functioning only in the spin antiparallel mode, the model fitted to the PNR-data is not very sensitive to the assumed dependence of f on the wavelength.

The flipper efficiency is supposed to be best described by $f_{93}(\lambda)$, and will be used in the rest of this chapter.

5.3.2 Model fitted to the PNR-data

To interpret the data measured on CRISP shown in Figures 5.2 and 5.3 a model was assumed in which the Co-Cr layer consists of ten slabs. The depth-resolution of Γ of the fitted model, is of the order of π divided by the maximum q at which the neutron reflectivity is measured, in this case this will be about 19 nm. Therefore, by dividing the Co-Cr layer in ten slabs, the model will be sensitive to all information that can be obtained from the data. At first instance the nuclear scattering length density, Γ_n, is supposed to be equal for all the slabs and independent of the applied magnetic field, however the magnetic scattering length density, Γ_m, can vary in each slab. The thickness and Γ_n, both the same for each slab, are both parameters to be fitted. Using the matrix method the values of the fitting parameters (thickness of the slabs, Γ_m of each slab at the various fields and Γ_n) are optimized such that the difference between the calculated reflectivity and the measured reflectivities is minimal. The optimized models for f_{fit} and f_{93} are given in Figure 5.6.

The model fitted to the data was refined, allowing the top slab to have a Γ_n and thickness value, different from these quantities for the bulk slabs. This refinement

resulted in a reduction of χ^2 from 3.81 to 2.65. This refined model is presented in Figure 5.7, the simulated reflectivity presented in Figures 5.2 and 5.3 corresponds to this model. Allowing Γ_n of the other slabs to fit independently from each other did not improve the fit to the data considerably and resulted in almost equal Γ_n values in these nine slabs. The model given in Figure 5.7 is considered the best model and will be discussed in the rest of this chapter.

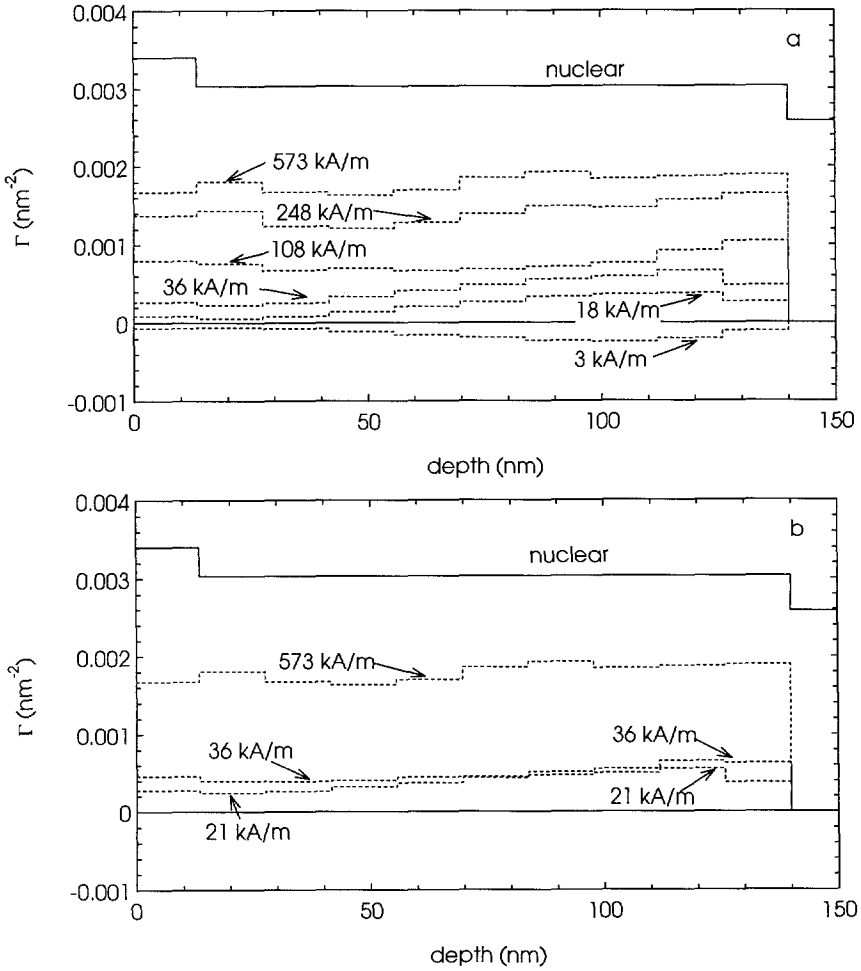

Figure 5.7: *The model fitted to the PNR-data, when the top slab is allowed to have a different value for Γ_n than the bulk. The model is fitted using f_{93} for the flipper efficiency. The magnetic profiles for increasing(decreasing) magnetic field values are given in figure a(b).*

The model is fitted to the data using 5.5 % $\Delta q/q$-resolution. Allowing some roughness at the interfaces did not decrease χ^2. The standard deviation s as a result of the counting statistics, considering a probability interval of 68.3 % of the fitting parameters is presented behind the obtained values in the following. The value 0.00301(3) nm^{-2}, obtained for Γ_n for the bulk Co-Cr, agrees with the value of 0.0030 as estimated by weighted averaging over Γ_n of bulk Co and bulk Cr. The top layer of the model is 14.7(2) nm thick and exhibits a value of 0.00335(1) nm^{-2} for Γ_n. The value of Γ_n for the silicon substrate: 0.00257(1) nm^{-2} differs only 1.4 % of the value 0.002604 nm^{-2} as calculated from lattice-spacing [33] and the scattering length [34]. The thickness of the bulk Co-Cr layer, obtained by fitting the data is 125.4(2) nm. The value of s for Γ_m varies between 0.03×10^{-3} nm^{-2} for the low magnetic fields and 0.06×10^{-3} nm^{-2} at the highest magnetic field of 573 kA/m.

None of the models given in Figures 5.6 and 5.7, with Γ_m equal to zero, could describe the data measured on ROG in a perpendicular field of 560 kA/m. However, when the same models were used with Γ_m at all slabs equal to zero, *and* roughness was allowed at the surface, all three models could describe this measurement. The simulated reflectivity in Figure 5.4 is obtained by assuming a roughness of 3 nm and the model given in Figure 5.7. Probably the sample has been contaminated in the three and a half years between the two measurements. The simulated reflectivity is smaller than the measured reflectivity for q larger than 0.11 nm^{-1}. This might be caused by a high background during this experiment. The data measured on ROG were fitted with a $\Delta q/q$-resolution of 6.6 %.

5.4 Comparison with Other Techniques: SEM and VSM

The thickness of the Co-Cr layer is determined from a cross section SEM-picture to be about 140 nm in agreement with the value determined by PNR of 140.1(4) nm. The thickness as determined by the sputter time and sputter velocity calibration is 160 nm. Apparently, in this case, PNR gives a better estimate than the value from sputter time and velocity.

Figure 5.8 shows the VSM magnetization curves in-plane and perpendicular to the plane. To calculate the magnetization from the product of the magnetic volume and magnetization, measured by VSM, the thickness as determined by PNR is used. In this figure also the overall magnetization corresponding to the fitted Γ_m-profile at the various applied fields is given. The agreement is reasonable. Figure 5.9 gives a SEM-picture of the top of the Co-Cr layer clearly showing the tops of the columns. From the scale of the picture it can be seen that one single column has a diameter of about 30 nm.

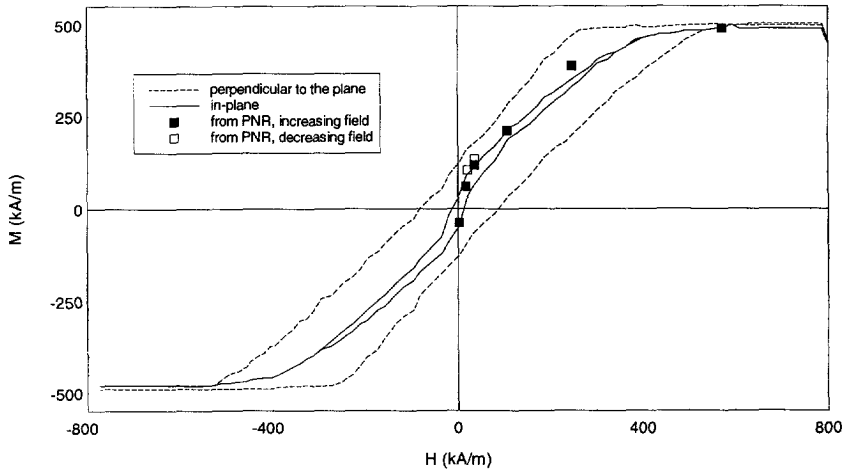

Figure 5.8: *Magnetization of the Co-Cr layer as a function of applied field as measured by VSM and as calculated from the model fitted to the PNR-data. The solid line represents the in-plane magnetization, the dashed line represents the magnetization perpendicular to the surface.*

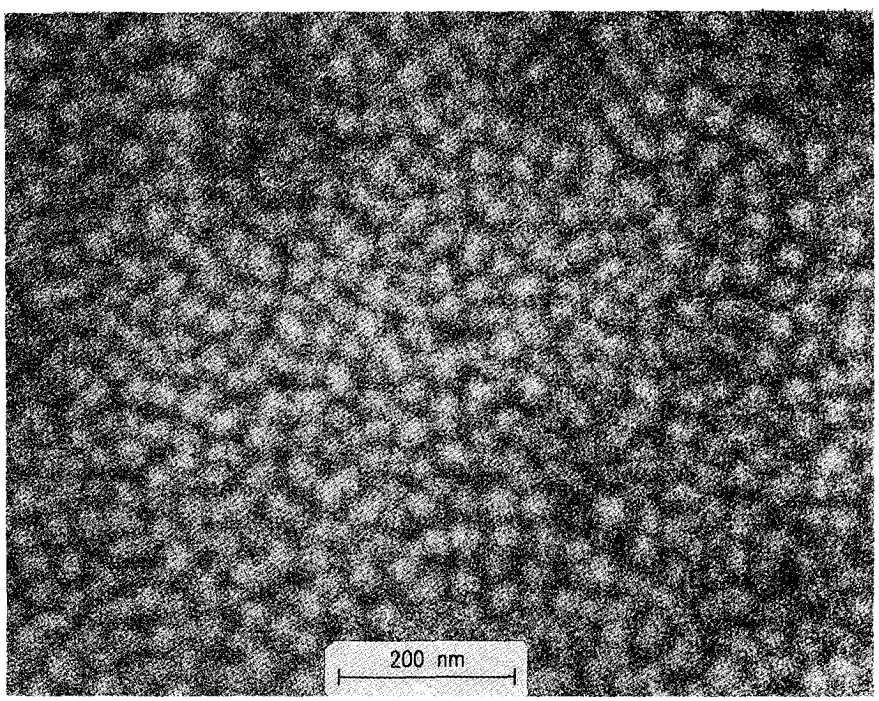

Figure 5.9: *Top side SEM-picture of the Co-Cr layer. The tops of the columns are clearly visible.*

5.5 Discussion

The in-plane magnetization curve as measured by VSM is much narrower than the perpendicular one, caused by the perpendicular magnetic anisotropy of the sample. The "S" shape of the in-plane magnetization curve at low magnetic fields was usually attributed to the relatively easy magnetization of the initial layer. However, the model given in Figure 5.7 clearly shows that Γ_m exhibits gradual changes rather than a discrete step, caused by an initial layer. From the model it is clear that at the lowest applied field of 3 kA/m the maximum of in-plane magnetization occurs in the third slab from the substrate. So M_r exhibits a maximum around 35 nm from the substrate. The "S" shape of the in-plane magnetization curve is caused by the relatively easy magnetization of the Co-Cr layer at the substrate side.

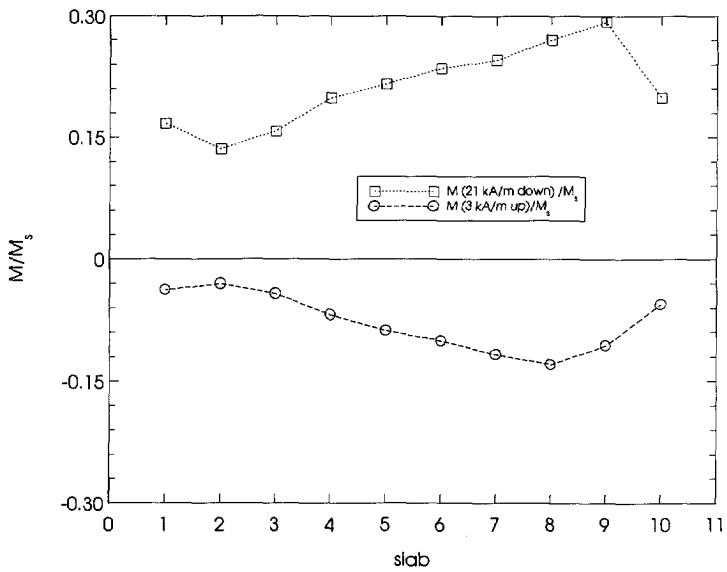

Figure 5.10: *The relative magnetization at an increasing field of 3 kA/m and a decreasing field of 21 kA/m in each slab of the model.*

The increase of Γ_n over 13 nm at the top of the sample can be caused by oxidation or contamination. From Figure 5.7 it is clear that the top layer exhibits a considerable magnetization. This magnetization can be caused by this top layer being only partially oxidized and by the presence of the magnetic compound CrO_2.

The gradual increase of the in-plane magnetization from the surface side into the layer of the Co-Cr at these low in-plane magnetic fields can be explained by a decrease of the preference orientation of the easy axis of magnetization perpendicular to the layer with depth. In Figure 5.10 the magnetization at 3 kA/m and at 21 kA/m (at decreasing field) both divided by the magnetization at 573 kA/m

are presented. As the sample is saturated at 573 kA/m (see Figure 5.8), the difference in this quotient shows the in-plane component of the easy-axis orientation throughout the sample.

At higher fields the in-plane magnetization increases also gradually with depth and no pronounced step of Γ_m (so-called initial layer) is observed. This gradual increase at high fields can be explained by the fact that the layer becomes more perfect when the layer grows thicker. Therefore, close to the substrate more grain boundaries will occur in which chromium dissolves. The spontaneous magnetization of Co-Cr sensitively increases with a decrease of the amount of chromium. As the cobalt closer to the substrate contains less chromium, M_s increases with depth.

To compare the field dependence of the magnetic properties as a function of depth, in Figure 5.11 the magnetization averaged over the two slabs at the surface side, in the middle and at the substrate side are presented as a function of applied field. By comparing the three curves one sees that the slope of the increasing field curve (at low magnetic field) increases with depth, caused by the decreasing perpendicular anisotropy from the surface to the substrate. From Figure 5.11 it is also clear that the saturation magnetization increases with depth. At magnetic field values of 108 and 248 kA/m, the middle slabs exhibit the lowest magnetization. This is not understood.

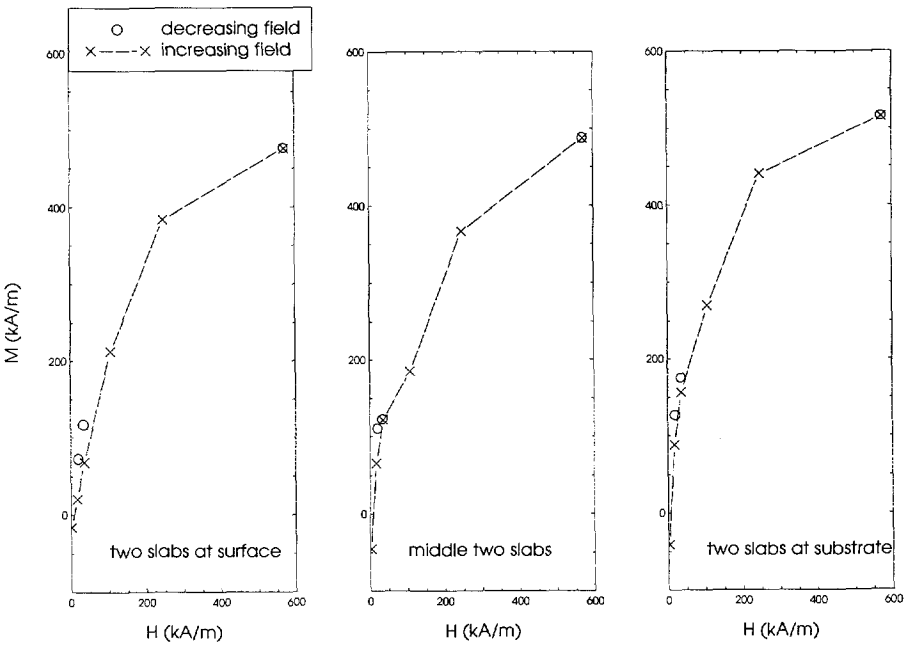

Figure 5.11: *The magnetization as a function of applied field for the two slabs at the surface, in the middle and at the substrate of the sample.*

5.6 Conclusions

- The measured polarized neutron reflectivity data of a Co-Cr film in an in-plane magnetic field can well be described using the model presented in Figure 5.7. This model exhibits no distinct initial layer, but gradual changes in the in-plane magnetization are observed. The maximum in M_r in-plane occurs around 35 nm from the substrate. The magnitude of M_s increases gradually with depth.

- The model describing the PNR data can be understood from the structure of the Co-Cr layer. At low fields the increase of Γ_m with depth, i.e. the in-plane magnetization, is caused by the increasing spread in preference orientation of the easy axis. At high magnetic fields the increase of Γ_m is caused by the increasing amount of grain boundaries with depth, in which chromium tends to dissolve. As the spontaneous magnetization of Co-Cr sensitively increases with a decrease of Cr, M_s increases with depth.

- The model agrees with the thickness as obtained by SEM and the average magnetization as determined by VSM.

Chapter 6

PNR on Metal Evaporated Videotapes

6.1 Introduction to Metal Evaporated Videotapes

Metal evaporated tapes (ME-tapes) are commercially available since 1989 and used in video Hi8mm-applications. ME-tapes are fabricated by oblique evaporation of cobalt and nickel at an increasing angle of incidence in the presence of oxygen [35]. This results in columnar banana-like structures with an average direction of their easy axes of about 45° to the substrate [36]. Figure 6.1 shows how

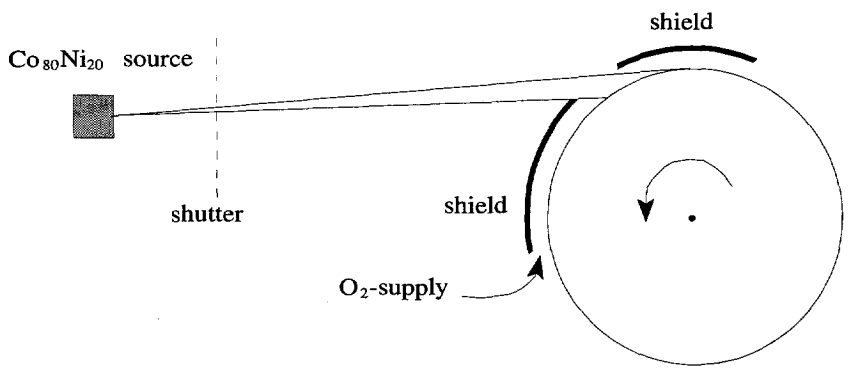

Figure 6.1: *Schematic view of the fabrication process of the videotape.*

the increasing angle of incidence is obtained. During evaporation the substrate moves along a rotating drum. As a result of this at the start of the evaporation process the angle of incidence is 90° (measured from the normal to the substrate) whereas at the end this angle is about 60°. The columns contain magnetic crystalline CoNi-grains, with oxides (primarily CoO) amongst them [37]. Figure 6.2

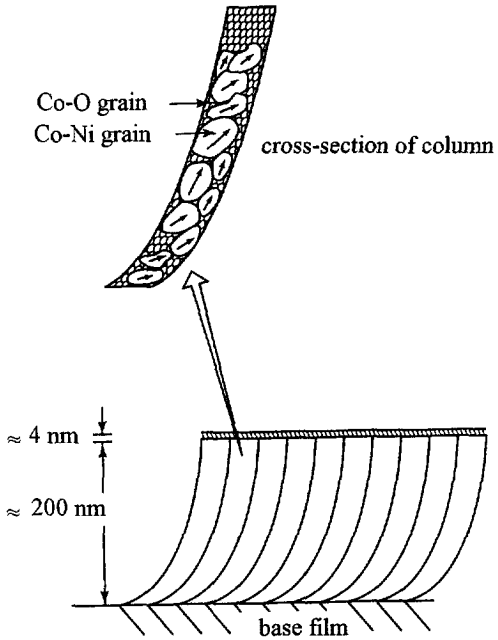

Figure 6.2: *Schematic view of the structure of the videotape, [38]*

gives a schematic overview of the structure of a ME-tape sputtered in one shift. ME-tape contains voids as a result of shadowing effects during evaporation [39]. As a substrate in most cases a polyester-type polymer containing fillers is used [36].

Recently ME-tapes are produced in more than one sputter-shift, resulting in multi-layered structures. The orientation of the columns in the separate layers might differ in order to give more symmetric pulse shapes [40]. Finally a lubricating non-magnetic protection layer is deposited on top of the magnetic layer.

ME-tapes show excellent recording performance at high recording densities. ME-tapes usually contain a magnetic layer of about 200 nm thick whereas this layer in traditional metal particle tapes is about 3 μm [41]. Because of the structure of the tapes changing with depth, one can expect their magnetic properties to depend on the depth. Until now little is known on the behaviour of the tape during a writing process. As PNR is sensitive to the magnetization as a function of depth, this technique is very useful to investigate the process of writing a signal on the tape and to determine magnetic characteristics of ME-tape as a function of depth.

6.2 Description of the PNR experiments

Two types of commercially available ME-tape are subject of this study: the SONY Hi8 ME and the TDK Hi8 ME-tape. The SONY Hi8 ME-tape is evaporated in one shift resulting in a magnetic layer of 150 nm thick as determined

by TEM [40]. In the following this tape will be referred to as the one-layer tape. The TDK Hi8 ME-tape is evaporated in two shifts at opposite angle of incidence, resulting in two magnetic layers with their easy axes nearly perpendicular to each other. A TEM-picture of this tape is given in Figure 6.3, showing the direction of the columns in both layers. From TEM the thickness of this tape is determined to be 180 nm [40]. This tape will be referred to as the two-layer tape. The bulk composition of both tapes is $Co_{71}Ni_{16}O_{13}$.

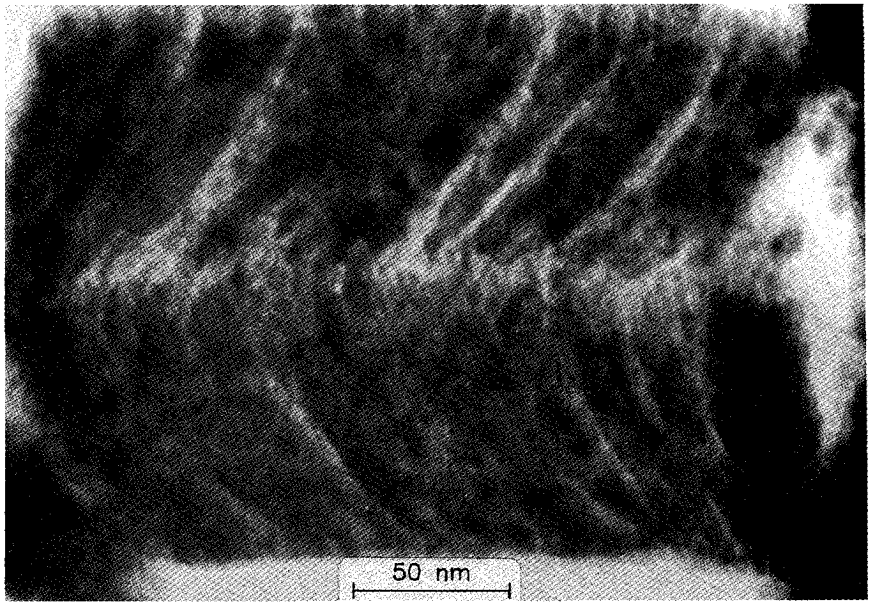

Figure 6.3: *TEM-picture of a two-layer tape, showing the banana-like regions in the tape.*

To study the magnetization by a recording head as used in a writing process, an 11 mm wide MIG recording head with a gap of 0.25 μm was used to write a DC signal on the 8 mm wide tape. The recording head had to be wide as PNR needs an in-plane homogeneous sample. Neutron reflectivity data of the tapes in the following magnetic states are obtained:

1. in remanence, after magnetizing the one(two)-layer tape by a field of 339 (337) kA/m using the wide head and a DC current
2. in remanence, after magnetizing the one(two)-layer tape by a field of 339 (337) kA/m using the wide head and a DC current and then demagnetizing (overall magnetization equal to zero as measured by VSM) it using an appropriate DC current of opposite sign
3. in remanence, after magnetizing the one(two)-layer tape by a field of 339 (337) kA/m using the wide head and a DC current and subsequently magnetizing

the tape in the opposite direction using a DC current of the opposite sign and same magnitude

4. in remanence after bulk demagnetization

5. perpendicularly magnetized by a field of 560 kA/m, to obtain a neutron reflectivity curve as determined by the nuclear structure of the tape only

6. in-plane magnetized by a field of 560 kA/m

7. in remanence after perpendicular magnetization of 560 kA/m (only for the two-layer tape).

In the first three states the tape moved along the recording head in the same direction during all magnetization processes. As the tape is not symmetrical in the writing direction, a difference might appear when the tape is moved in the opposite direction. However, in this preliminary study we have only considered the direction that is used in practice. When the magnetic field produced by the recording head is larger than the chosen fields of 337(339) kA/m, the magnetization of the tapes does not increase, as determined by VSM.

The first four states for both tapes are measured on CRISP [42], the time-of-flight reflectometer of ISIS, states **5**, **6** and **7** are measured on ROG [14, 43], the time-of-flight reflectometer of IRI in Delft. The measurements on CRISP are performed with a second spin flipper and a polarization analyzer between the sample and the detector. In this way, neutrons that might have reversed their polarization as a result of the interaction with the sample are not detected.

To measure the tape in state **5** a device was attached to the pole shoes (see Figure 3.5) to turn the direction of the applied magnetic field by 90°. As the device has been used for the first time in the measurement of the one-layer tape, its reflectivity was measured with a spin parallel and a spin antiparallel polarized beam separately to check the functioning of the device. For the two-layer tape the unpolarized beam is used, to gain intensity. All measurements are performed with an angle of incidence of the neutron beam of about 5 mrad.

The tape was side to side attached to a flat piece of glass using vacuum oil, both to enlarge the sample surface in the length direction of the neutron beam and to diminish the curling of the tape. The tape tends to curl especially in the direction perpendicular to the recording direction. The glass support has a width of 3 cm. Figure 6.4 shows the configuration of the sample in the neutron beam.

6.3 Results and Interpretation of PNR

The measured neutron reflectivity data of the one-layer tape are shown in Figures 6.5 through 6.9 and of the two-layer tape in Figures 6.12 through 6.17.

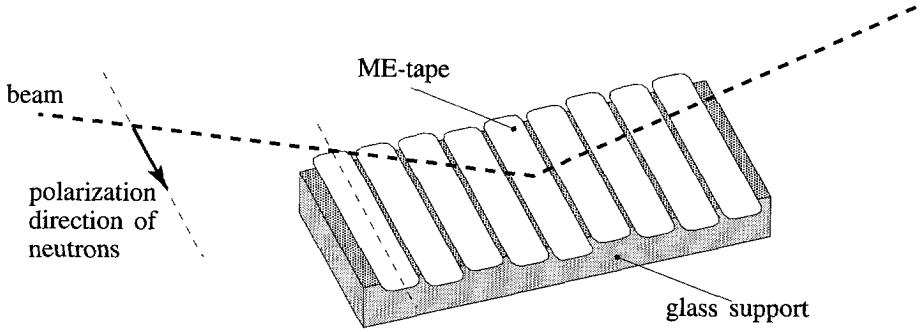

Figure 6.4: *The configuration of the sample during the PNR-experiment.*

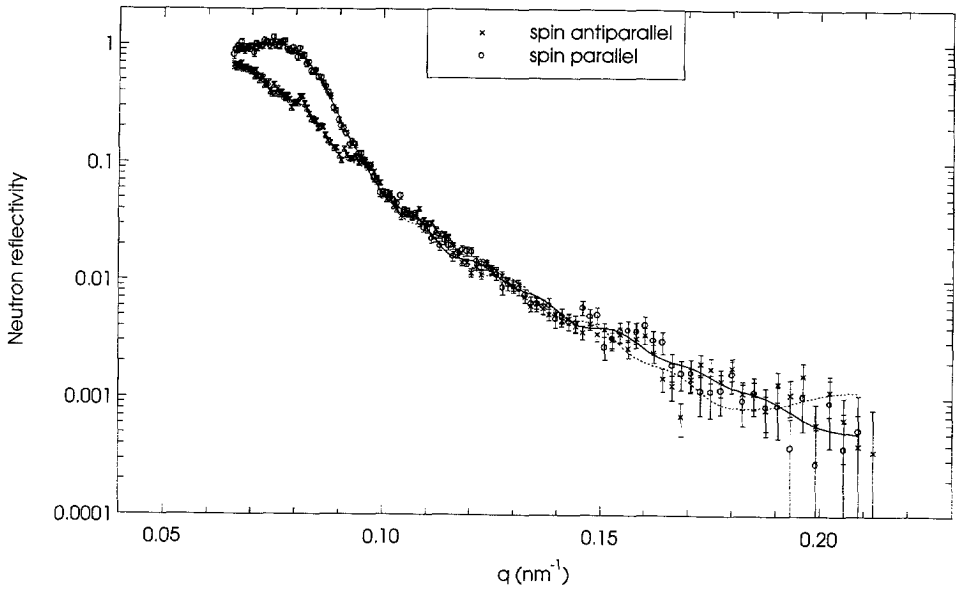

Figure 6.5: *Neutron reflectivity of the one-layer tape in state* **1** *as measured (symbols) and simulated for both spin states (solid line parallel, dashed antiparallel).*

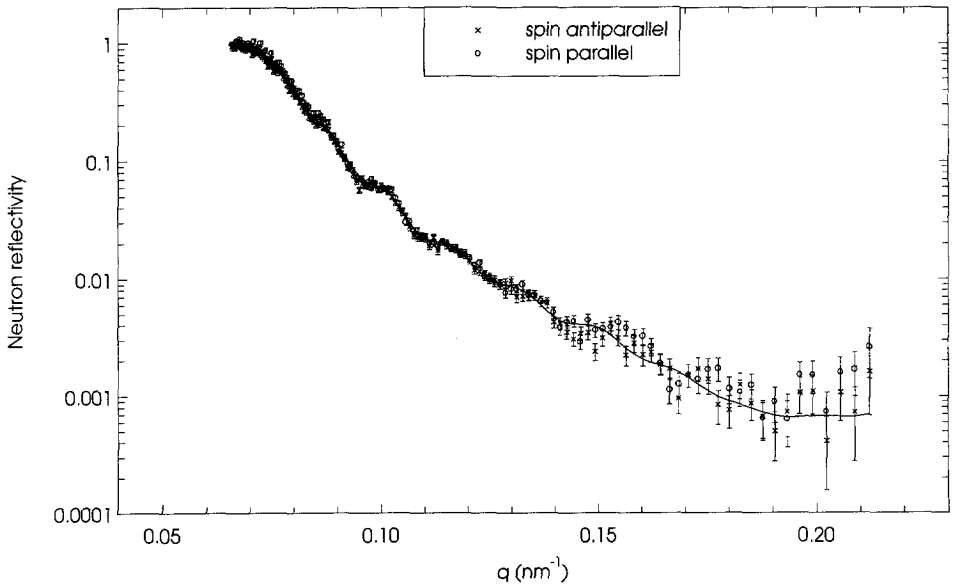

Figure 6.6: *Neutron reflectivity of the one-layer tape in state* **2** *as measured (symbols) and simulated for both spin states (solid line parallel, dashed antiparallel).*

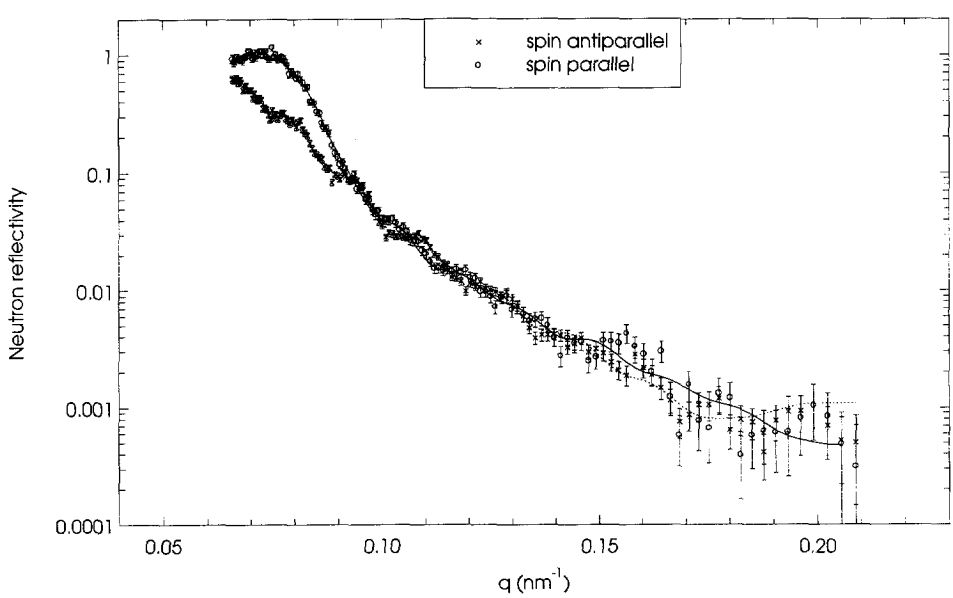

Figure 6.7: *Neutron reflectivity of the one-layer tape in state* **3** *as measured (symbols) and simulated for both spin states (solid line parallel, dashed antiparallel).*

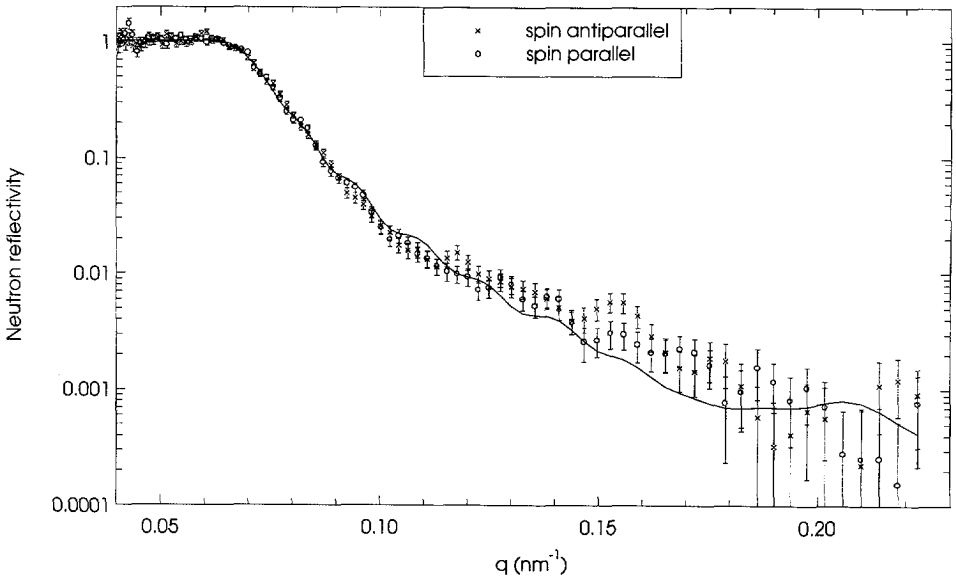

Figure 6.8: *Neutron reflectivity of the one-layer tape in state* **5**, *sensitive to the nuclear structure, as measured (symbols) and simulated (solid line).*

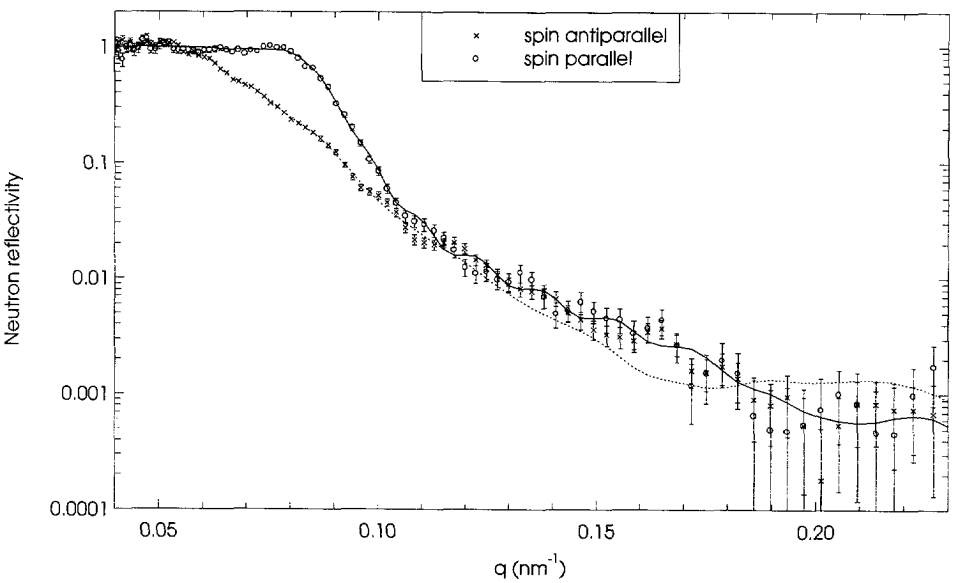

Figure 6.9: *Neutron reflectivity of the one-layer tape in state* **6** *as measured (symbols) and simulated for both spin states (solid line parallel, dashed antiparallel).*

The lines in these figures represent the neutron reflectivity as simulated by the parameter optimization routine corresponding to the models described below. The presented simulated neutron reflectivity has also been convoluted with the $\Delta q/q$-resolution, and corrected for the polarization of the instruments. The data measured on ROG as presented are corrected for the divergence of the neutron beam as described in paragraph 4.3. To perform this correction it is assumed that the useful sample width was 2.5 cm, by visual inspection. The exact sample width was difficult to determine because the videotape curled. For clarity see Figure 6.4. The divergence of the beam on CRISP is independent of the wavelength and therefore no correction for the beam divergence is performed.

For both tapes the neutron reflectivity data of state **2** and **4** are approximately equal. This means that demagnetizing the tape by the recording head or by bulk demagnetization results in the same depth dependence of the in-plane magnetization in the tape. As the difference between spin parallel and antiparallel data is very small in both states, Γ_m vanishes throughout the whole tape. For both tapes the data of state **1** and **3** are very similar, except that spin parallel reflectivity of state **1** corresponds to the spin antiparallel reflectivity of state **3** and vice versa.

Figure 6.8 shows the measured data of the one-layer tape in a perpendicular field of 560 kA/m. The two reflectivity curves for the spin parallel—and the spin antiparallel—case are the same within the statistical error. This indicates that the device to create a perpendicular magnetic field has saturated the one-layer tape perpendicular and is functioning well in this case.

6.3.1 Model of the One-layer Tape

To avoid confusion, hereafter "layer" will refer to a layer of one of the tapes, grown in one sputter shift, and "slab" will refer to a slab of constant nuclear scattering length density Γ_n and magnetic scattering length density Γ_m represented by a matrix in the matrix method described in section 3.1.

A model is fitted simultaneously to the data shown in Figures 6.5 through 6.9, This model assumes a pile of ten magnetic slabs of equal thickness and a non-magnetic slab of different thickness on top of it, to include the lubricating layer. The smallest x-range on which information can be obtained is related to the maximum q-value at which the reflectivity is measured and is of the order of $\pi/0.22\ \mathrm{nm}^{-2} = 14$ nm. By dividing the tape in ten slabs, each slab is of the order of this x-range. Each slab has constant Γ_n and Γ_m keeping the thickness and Γ_n the same for the different magnetic states. The total thickness, Γ_n of each slab and Γ_m of each slab at the various magnetic states are parameters to be fitted. The neutron reflectivity curves of the one-layer tape show no pronounced details, resulting in a very weak dependence of the value of χ^2 (for definition Eqn. (4.30)) on the model parameters. This makes it difficult to find an objective set of values for the model parameters.

For example, when no boundary conditions are applied to the above described model, a minimum of 1.51 for χ^2 is found for the set of model parameters given by the dashed line in Figure 6.10. This model will be called the free-model. The

total thickness of the magnetic layer according to this model is 148 nm.

In Table 6.1 the average magnetization simulated for the free-model of the tape in different magnetic states is given. Also the average magnetization as determined by VSM is given. To calculate the magnetization from the VSM-signal, 150 nm was used for the thickness of the tape. From Table 6.1 it is clear that the average magnetization values in the tape from the parameters corresponding to the free-model do not match with the VSM results. The values from PNR seem to be shifted to the positive direction compared to the VSM-values. To obtain a minimum that agrees better with VSM, various boundary conditions were tried. Good agreement could be obtained when using two boundary conditions:
- Γ_m in state **3** has to be equal in size but opposite to Γ_m in state **1** (this boundary condition is deduced from the opposite values of the average magnetization in both states as obtained by VSM).
- Γ_m in state **2** has to be equal to zero in all slabs (this boundary condition is deduced from the resemblance in the measured PNR-data in state **2** and state **5**).
The model obtained when applying above conditions is called the boundary-model. The values for the average magnetization corresponding to this model are also given in Table 6.1. The agreement is acceptable.

From Table 6.1 it is clear that χ^2 increases a little when boundary conditions are applied, but the agreement with the VSM-data is best for the boundary-model. In Figure 6.10 the free-model and the boundary-model are given together. The nuclear structure and also the over depth averaged magnetization, <M>, in state **6** as obtained by fitting the various models does not change considerably for the different models.

Also the trend in the obtained Γ_m-profiles in state **1**, **2** and **3** is similar in both models. Apparently the different assumptions have very little influence on the depth profile of Γ_n and Γ_m.

Based on the agreement of the values obtained by fitting the PNR-data and VSM-measurements, the boundary-model presented in Figure 6.11 is considered to represent the reality the best. The lines presented in Figures 6.5 through 6.9 correspond to the boundary-model.

Allowing roughness at the surface and interfaces did not improve the fit to the data or the correspondence between VSM and PNR considerably. Therefore it was decided not to allow roughness at the interface.

For the boundary-model the values of the standard deviation s of the different model parameters, as a result of the counting statistics corresponding to a probability interval of 68.3 %, are estimated. To estimate the values of s it is assumed that the boundary-model represents the physical reality well. However, from Table 6.1 it is clear that also other models can give a reasonable fit to the data. Table 6.1 gives an indication of the possible error in the determined values of Γ_m.

All values for Γ_n have a relative standard deviation of less than or equal to 1 %. The values of s of Γ_m in state **1** and **3** vary between 0.02×10^{-3} nm^{-2} on top of the magnetic sample to 0.07×10^{-3}nm^{-2} at the substrate side. For state **6** s of Γ_m varies between 0.07 and 0.14×10^{-3}nm^{-2}.

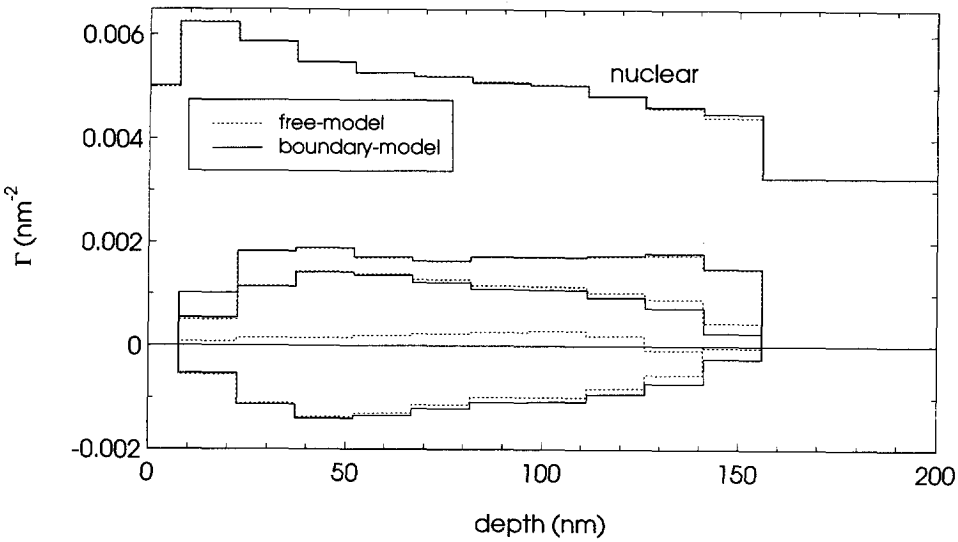

Figure 6.10: *The two models fitted to the PNR-data of the one-layer tape: the solid line represents the free-model and the dashed line represents the boundary-model. In Figure 6.11 the different magnetic states are given*

The calculated value for Γ_n of pure PET (weight density of 1.375 g/cm^2) is 3.1 $\times$ 10^{-3} nm^{-2}. By fitting the boundary-model to the PNR-data, a value of 3.25 $\times$ 10^{-3} nm^{-2} with an s of 0.03 $\times$ 10^{-3} nm^{-2} is determined. It is possible that PET of a different density is used, or fillers are added, but the agreement between the two values is very good.

A way to minimize the number of fitting parameters for this sample is to assume an analytical dependence of Γ_n and Γ_m on the depth. In that case software should be written that approaches this dependence by a model with very thin slabs.

Summarizing one can say that great care has to be taken in interpreting PNR-data showing little details. Therefore it is necessary to collect as much information as possible from other techniques.

Table 6.1: *Comparison of magnetization, as obtained by fitting PNR-data and by VSM for the one-layer tape.*

	VSM (kA/m)	PNR free-model (kA/m)	PNR boundary-model (kA/m)
M state 1	256±10	284	267
M state 2	-20±10	39	0
M state 3	-257±10	-242	-267
M state 6	-	447	451
χ^2	-	1.51	1.63

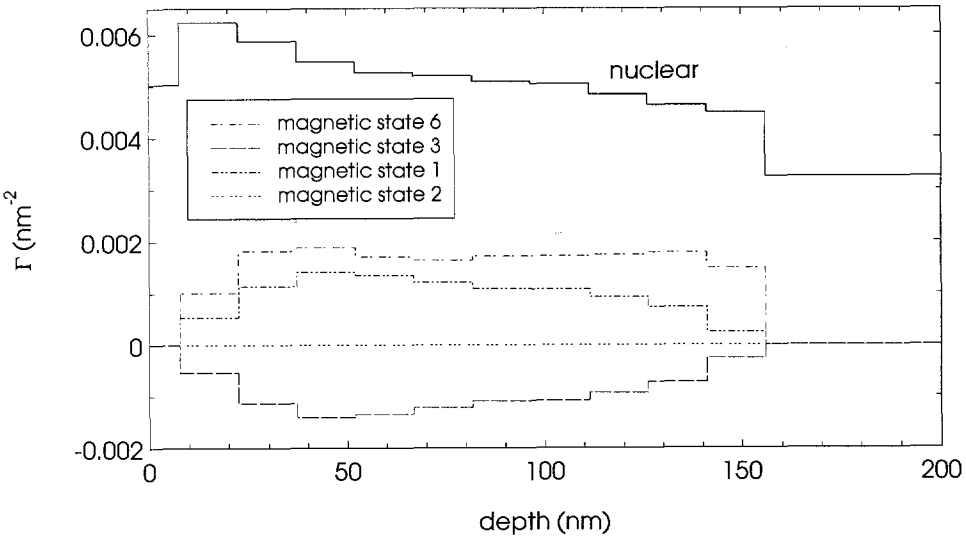

Figure 6.11: *The boundary-model. The simulated neutron reflectivity in Figures 6.5 through 6.9 corresponds with this model.*

6.3.2 Model of the Two-layer Tape

In Figures 6.12 through 6.17 the PNR curves of the two-layer tape are presented. Compared to the PNR-curves of the one-layer tape, these curves contain more characteristics and therefore probably contain more information.

In first instance the data were fitted by a model of 10 slabs of equal thickness with a non-lubricating slab on top of it. This resulted in a value for χ^2 of 2.96 and the depth profiles of Γ_n and Γ_m as presented in Figure 6.18. From Figure 6.18 it is clear that a local minimum in $|\Gamma_m|$ occurs in the fifth slab of the model for all magnetic states. Therefore a new model has been fitted to the data, assuming a non-magnetic region between the two sputtered layers.

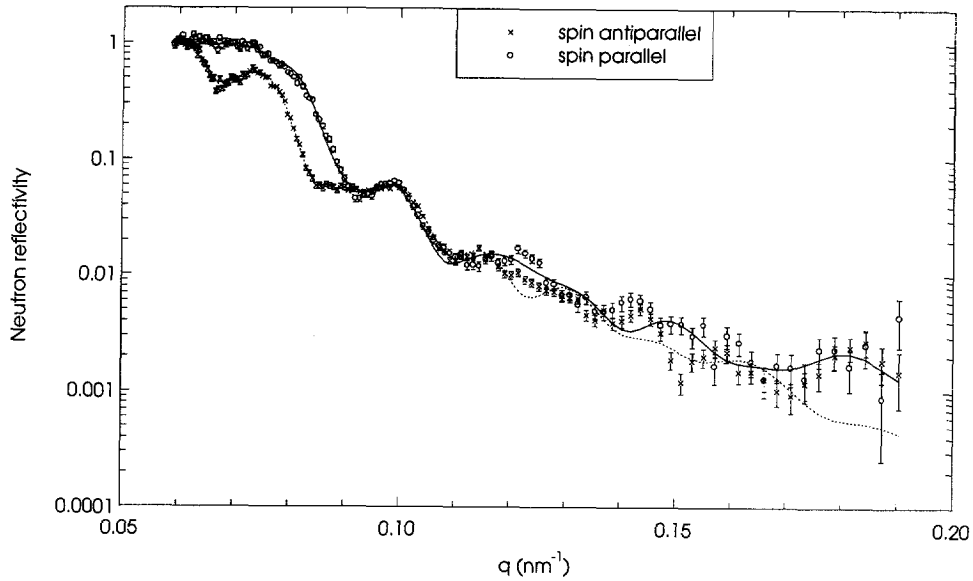

Figure 6.12: *Neutron reflectivity of the two-layer tape in state* **1** *as measured (symbols) and simulated for both spin states (solid line parallel, dashed antiparallel).*

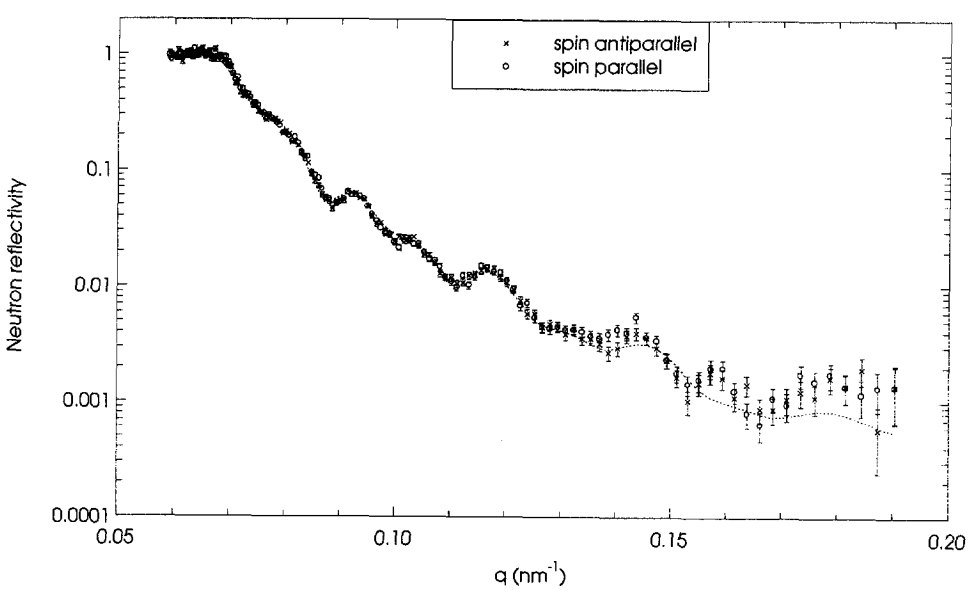

Figure 6.13: *Neutron reflectivity of the two-layer tape in state* **2** *as measured (symbols) and simulated for both spin states (dashed line).*

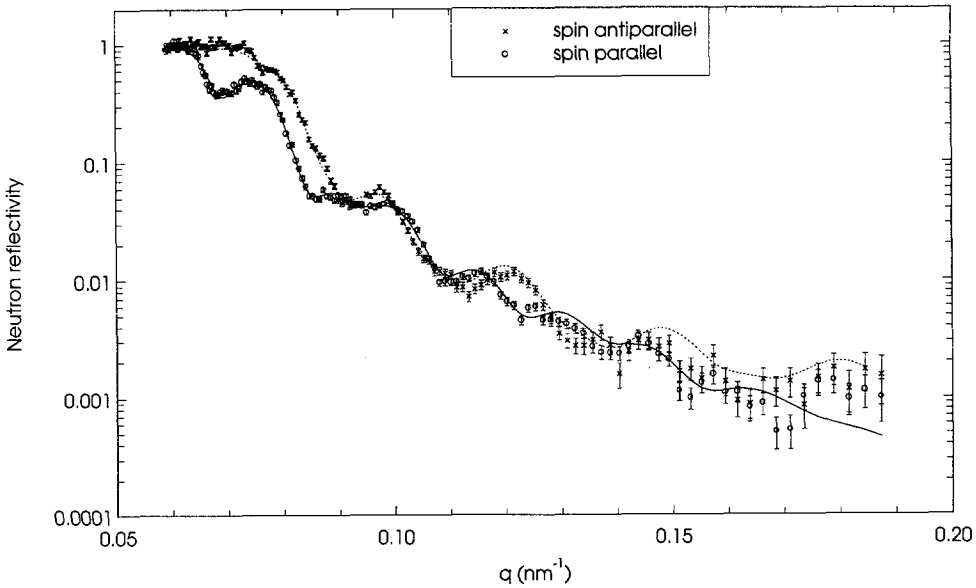

Figure 6.14: *Neutron reflectivity of the two-layer tape in state* **3** *as measured (symbols) and simulated for both spin states (solid line parallel, dashed antiparallel).*

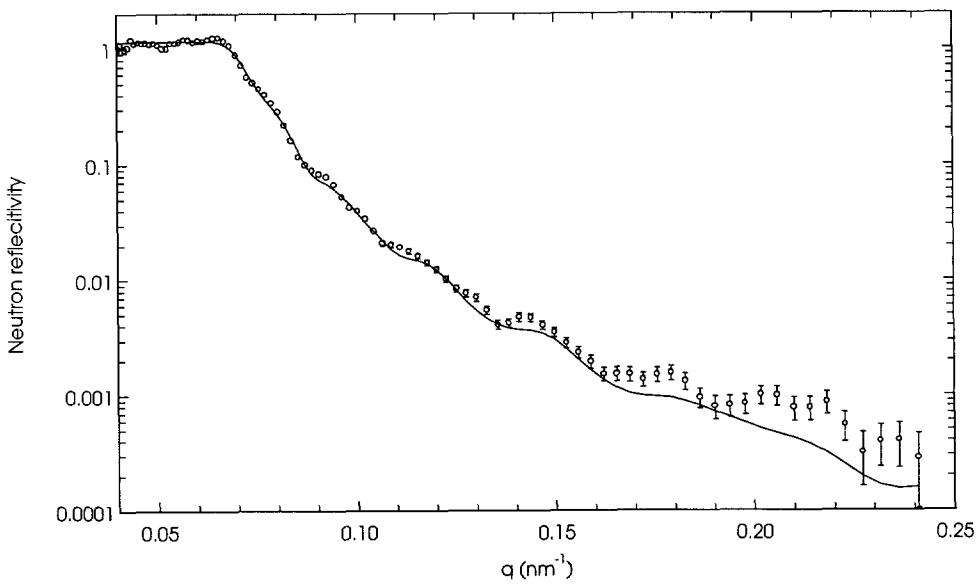

Figure 6.15: *Neutron reflectivity of the two-layer tape in state* **5** *as measured (symbols) and simulated (solid line).*

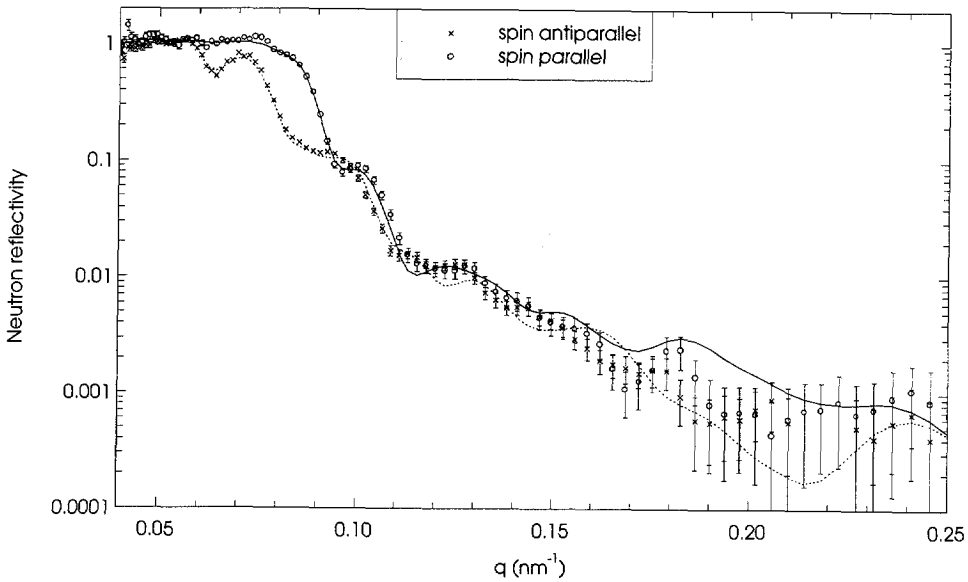

Figure 6.16: *Neutron reflectivity of the two-layer tape in state* **6** *as measured (symbols) and simulated for both spin states (solid line parallel, dashed antiparallel).*

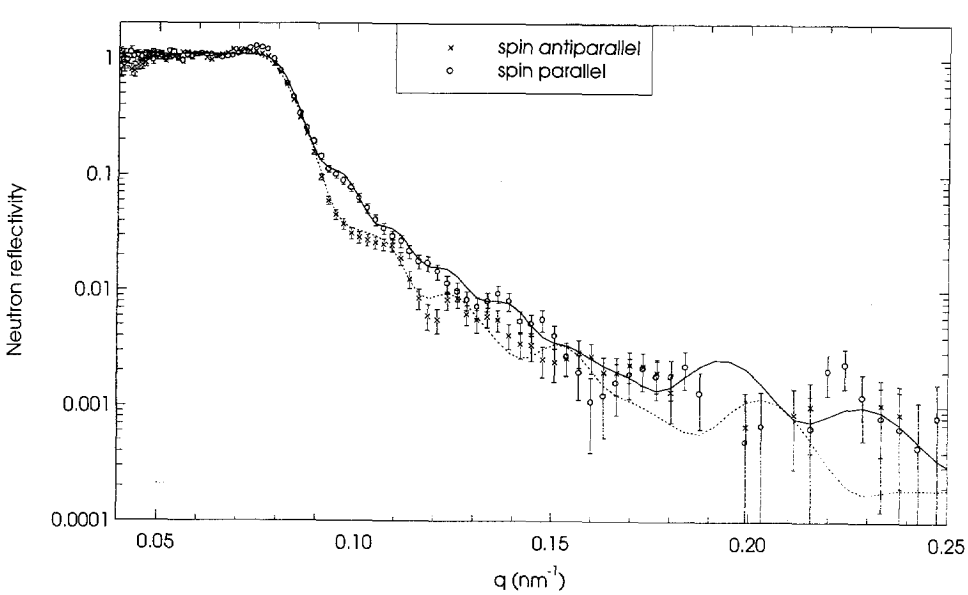

Figure 6.17: *Neutron reflectivity of the two-layer tape in state* **7** *as measured (symbols) and simulated for both spin states (solid line parallel, dashed antiparallel).*

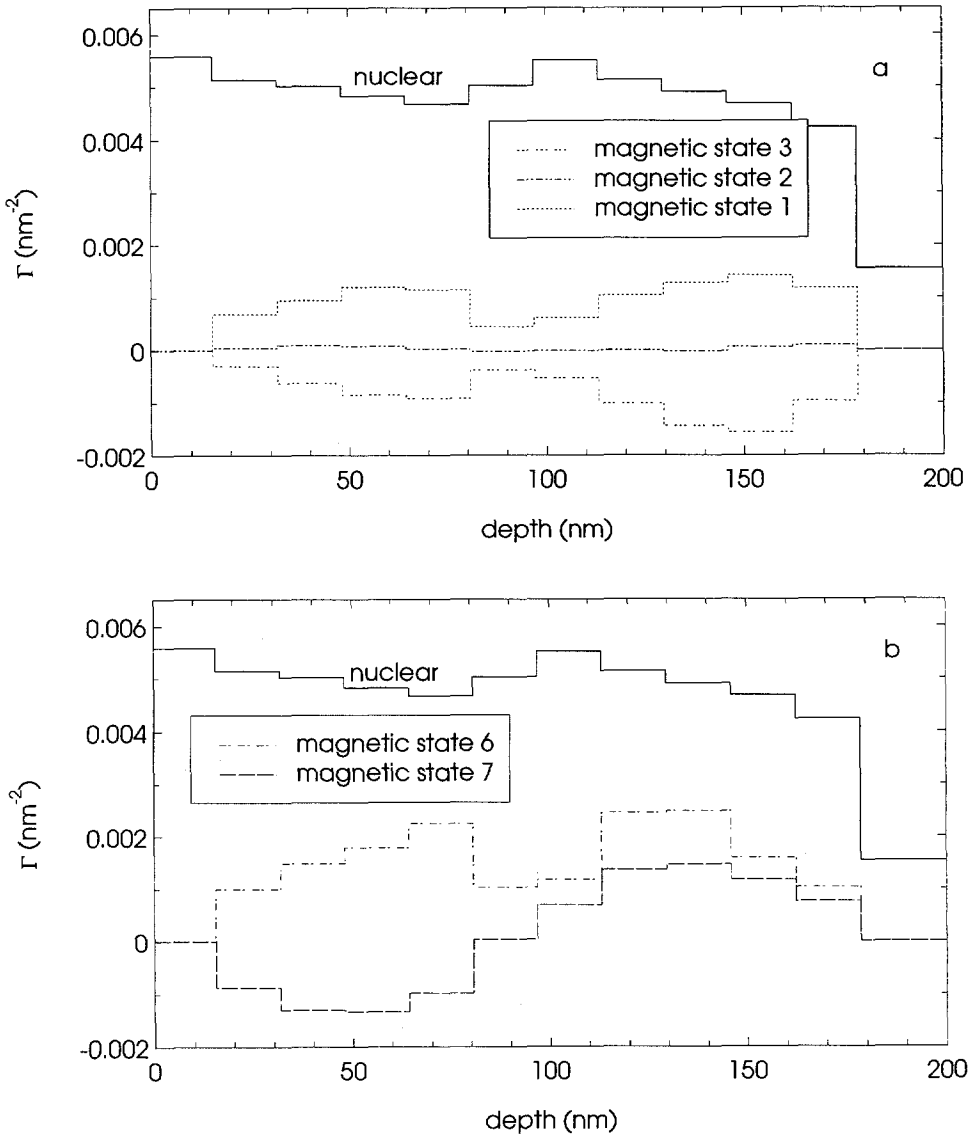

Figure 6.18: *Model fitted to the two-layer tape assuming ten magnetic slabs of equal thickness. In Figure a the model for state* **1**, **2** *and* **3** *is given, in Figure b the model for state* **6** *and* **7**.

In this model the sputtered layers are both divided in five magnetic slabs of equal thickness. However, the thickness of the slabs in one layer, and therefore the total thickness of this layer, is not related to this parameter of the other layer. The thickness of the non-magnetic slab between these two layers is also a parameter to be fitted. Assuming this model improved the agreement between simulated and measured PNR-data: χ^2 reduced from 2.96 to 2.71. Also the correspondence between VSM and PNR became better. This indicates that between the two sputtered layers the tape indeed contains a region of non-magnetic material. Another advantage of this model is that by determining the boundary between the two layers, the integrated magnetization in the two layers separately can be compared. The model assuming a non-magnetic region is supposed to describe the measurements best and will be discussed in the following.

The model assuming two layers separated by a non-magnetic slab, resulted in the set of fitting parameters given in Figure 6.19. As allowing roughness at the surface and interfaces did not improve the fit to the data, the model neglects this. The value of the relative standard deviation of Γ_n is for the lubrication slab and the substrate 3 % and for the magnetic slabs less than 1 %. In magnetic states **1**, **2** and **3**, $s(\Gamma_m)$ varies between 0.03×10^{-3} and 0.07×10^{-3} nm^{-2}. In magnetic state **6** $s(\Gamma_m)$ is about 0.13×10^{-3} nm^{-2} and in state **7** s varies between 0.11 and 0.29×10^{-3} nm^{-2}.

The quality of fit is relatively low for state **5**, as compared to the other magnetic states. Calculating dev^2 (in agreement with Eqn. (4.28)) according to:

$$dev^2 = \sum_{i=1}^{N} \frac{R_{fit,i} - R_{exp,i}}{N(\Delta R_{exp,i})^2}, \tag{6.1}$$

a value of dev^2 of the PNR-data in state **5** is obtained of 4.6. This is relatively large: dev^2 of the other curves varies around 2.2. This indicates that the magnetization in the two-layer tape still contains in-plane magnetic components. Apparently a larger perpendicular field is needed to saturate the two-layer tape in this direction.

Fitting the model to the data results in a value of 1.6×10^{-3}nm^{-2} with s of 0.7×10^{-3}nm^{-2} for Γ_n of the substrate. This value is lower than the calculated value for Γ of pure PET (weight density of 1.375 g/cm^2), 3.1×10^{-3} nm^{-2} and also lower than the value found for the one-layer tape. Considering the fact that fillers might be added [36] or PET with a different density might be used, the agreement between the fitted value and this calculated value is considered acceptable.

6.4 Correspondence with Other Techniques

For the one-layer tape the results from VSM were needed to choose the best fitted model to the PNR-data as discussed in the subsection 'model one-layer tape'. The value of M_s of this tape as determined by VSM is 420($\pm$10) kA/m [40]. From PNR a value of 451($\pm$19) kA/m is obtained at an in-plane magnetic field of 560 kA/m, in reasonable agreement with VSM. This value indicates that the tape in

Table 6.2: *Comparison of magnetization, as obtained by fitting PNR-data and by VSM for the two-layer tape.*

magnetic state	$<M>_{VSM}$ (kA/m)	$<M>_{PNR}$ (kA/m)
remanent state 1	216±10	222±10
remanent state 2	10±10	10±9
remanent state 3	-187±10	-191±11
state 6	366±6	356±18

state **6** is in-plane saturated. The fitted thickness of the boundary-model is 148 nm with s 1 nm. This is in good agreement with the 150 nm obtained by TEM.

In Table 6.2 the average magnetization from the model fitted to the two-layer tape is given together with the magnetization as determined from VSM-measurements. To calculate the average magnetization from the VSM-measurements the magnetic thickness as obtained from the model fitted to the PNR-data is used. The agreement between the results from PNR and VSM is very good. The magnetization in state **6** is obtained from the VSM curve in Figure 6.20 [40].

In Figure 6.3 a TEM-picture of the two-layer tape is given. The total thickness of the tape as determined from this picture is 180 nm. The total thickness of the tape from PNR is 179 nm, in excellent agreement with TEM.

6.5 Discussion

The experimental $\Delta q/q$-resolution for the different experiments is treated as a parameter to be fitted. Both for the experiments performed on CRISP and on ROG the fitted resolution was larger than estimated from the diaphragm settings. From the diaphragm settings, a resolution of about 5.5(6.6) % was expected for CRISP (ROG) whereas a value of 8(9) % was fitted. This difference in resolution is probably caused by the sample not being perfectly flat, for example caused by air bubbles or variation in the amount of vacuum oil used to attach the tape to the glass support.

6.5.1 Nuclear Density

From Figure 6.11 it is clear that Γ_n increases during sputtering. This can be caused by more voids produced at the beginning of the sputtering process by shadowing effects, and the layer becoming more dense during sputtering. However, the increase in Γ_n can also be caused by compositional changes. In the case of the two-layer tape Γ_n of the two separately sputtered layers increases during sputtering just like in the case of the one-layer tape, as shown in Figure 6.19.

In the literature high percentages of voids are mentioned as a consequence of shadowing effects during sputtering. As a first order estimate of the expected Γ_n in the tapes with composition $Co_{71}Ni_{16}O_{13}$, each atom is supposed to occupy a

cubic volume with its edge two times its atomic radius. Dividing the neutron scattering length of each atom by this cubic volume and then averaging this 'neutron scattering length density' weighted for the composition of the tapes, results in an estimate of Γ_n of solid $Co_{71}Ni_{16}O_{13}$ of 0.0069 nm^{-2}. This estimate corresponds to the assumption that all atoms are packed according to a simple cubic structure. When a perfect body centered structure is assumed, a value of 0.0090 nm^{-2}, and for a perfect face centered cubic or hexagonal structure a value of 0.0097 nm^{-2} is found. The CoNi-particles order in a hexagonal or face centered cubic structure. However, also oxides and amorphous regions occur.

The average value of Γ_n of the model fitted to the one-layer tape is 0.0052 nm^{-2}. Assuming only the closed packed hexagonal and face centered cubic structures, an estimate of the voids fraction in the tape can be calculated of 46 %. For the two-layer tape the average value of Γ_n is 0.0049 nm^{-2}, resulting in an estimate of the voids fraction of 51 %. This estimate is the largest fraction of voids possible, as also less dense packed regions will occur in the tape. Apparently the pause in the sputter process of the two-layer tape and/or the changing angle of incidence, results in a lower Γ_n averaged over whole tape depth.

An estimate of the voids fraction in ME-tape of almost 50 % is reported by Richter [44], in good agreement with the rough estimate from this work. This estimate is based on the measured amount of Co in the tape and density data for Co (probably in CoNi) and CoO.

6.5.2 Magnetic Depth Profile of the One-layer Tape

As mentioned above voids diminish the volume fraction of material resulting in variations of M_s through the layer. In Figure 6.21 the quotient Γ_m/Γ_n for state **6** is given. As Γ_n is directly dependent on the fraction of voids, this quotient represents the magnetization of the non-voids part of the layer when 560 kA/m in-plane is applied. The slab at the surface side has a considerably smaller magnetization than the rest of the layer. This is probably due to oxidation of the surface.

In Figure 6.22 the relative composition as a function of sputter time as obtained by Auger analysis is presented. The vertical lines are estimates of the interfaces of the slabs of the model in Figure 6.11. To make this estimate, the following was assumed:

- The crossing between the signal of Co and C represents the interface between the magnetic region and the PET substrate of the tape.
- All represented elements are equally sensitive to the sputter process.
- The sputter time is linear with the depth of the layer (i.e. the density of the layer has no influence).

Figure 6.21 shows that in the bulk of the layer the quotient Γ_m/Γ_n is almost constant. Since Figure 6.22 shows that it is reasonable to assume a constant composition in the middle eight slabs of the magnetic region, the fact that the quotient Γ_m/Γ_n is constant is an indication that the layer is saturated.

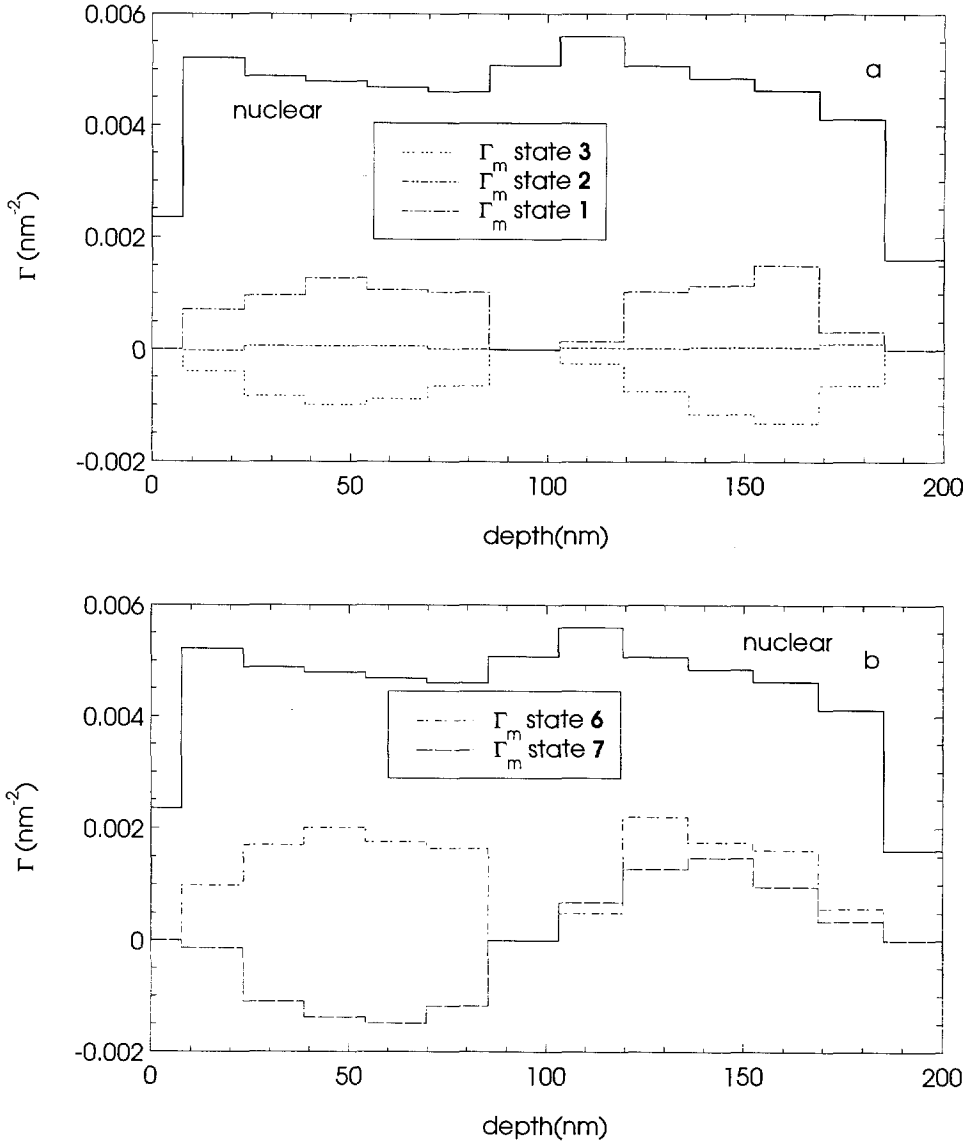

Figure 6.19: *The model obtained by minimizing the measured PNR data of the two-layer tape assuming the two layers are separated by a non-magnetic region. Figure a shows the model for magnetic state* **1**, **2** *and* **3**, *Figure b shows the model for magnetic state* **6** *and* **7**.

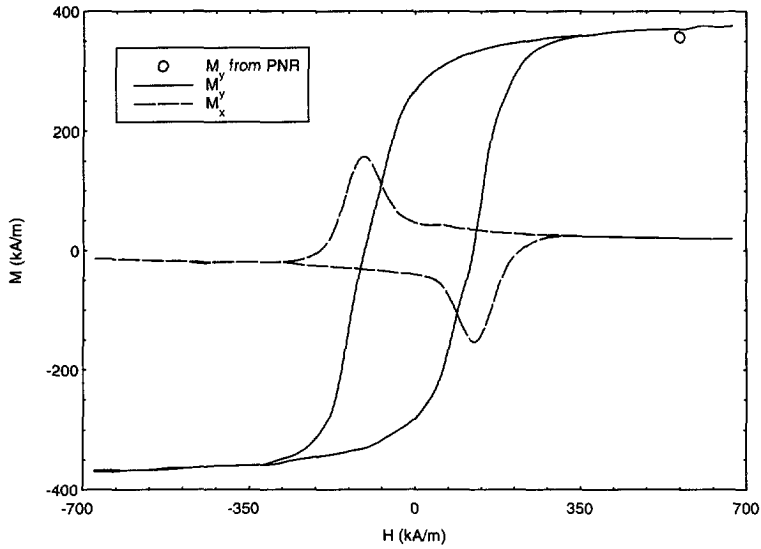

Figure 6.20: *The magnetization of a two-layer tape in the in-plane direction (M_x) and perpendicular to the plane (M_y) both when an in-plane magnetic field is applied as measured by VSM [40]. The open circle indicates the average magnetization calculated from the model fitted to the PNR-data at the applied magnetic field in magnetic state* **6**.

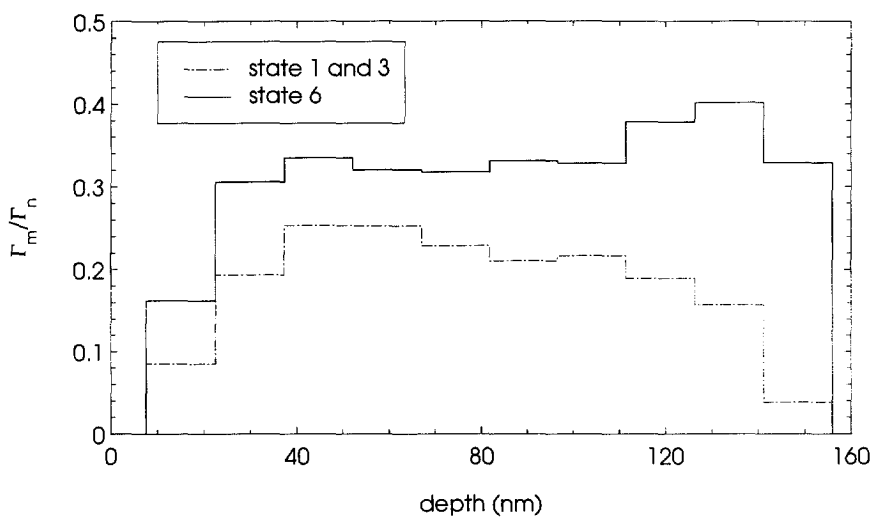

Figure 6.21: *The magnetic part of* Γ *in state* **6** *(solid) and state* **1** *and* **3** *(dashed) divided by the nuclear part for each slab of the one-layer tape.*

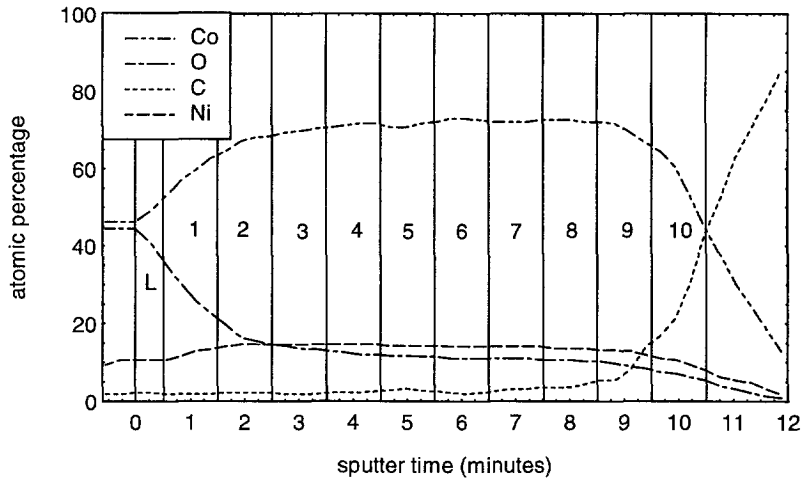

Figure 6.22: *The atomic percentage as determined by Auger analysis as a function of sputter time. During the Auger analysis small amounts of the sample are removed, so the sputter time is a measure for the depth. The vertical lines correspond to the slabs of the model fitted to the PNR-data (see Figure 6.11), assuming the crossing between Co and C concentration corresponds to the boundary between magnetic area and PET-substrate. 'L' denotes the lubricating layer.*

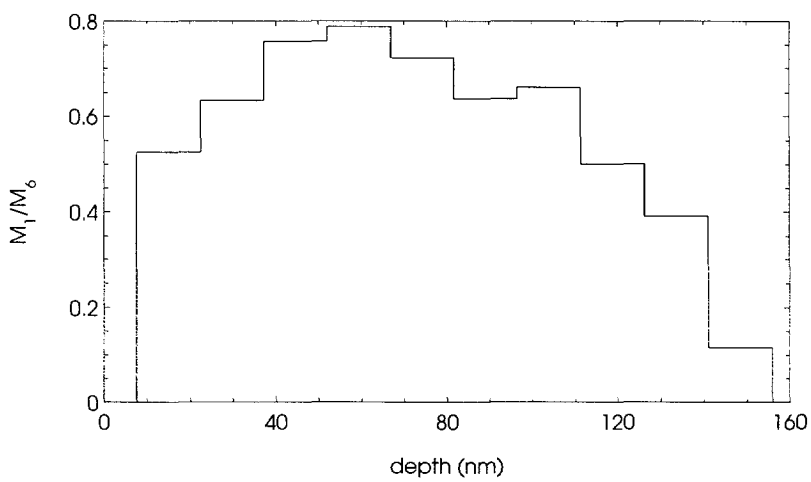

Figure 6.23: *The in-plane magnetization in state* **1** *and* **3** *divided by the in-plane magnetization in state* **6** *as a function of depth for the one-layer tape.*

Figure 6.21 also gives the Γ_m in state **1** and **3** in each slab divided by Γ_n. In contrast to the almost constant quotient in state **6**, in state **1** and **3** a maximum occurs around 50 nm from the surface. By dividing by Γ_n correction has taken place for the density difference in the material. Apart from this density difference, other effects have to be considered:

- At low fields the voids not only diminish the magnetization because of the smaller volume of magnetic material but also because of demagnetization fields. The fraction of voids is also a measure for the inhomogeneity of the layer. Probably when more voids are present more non-magnetic or non-magnetized material is present around these voids. As the amount of voids increases from the surface to the substrate both effects result in a decrease of magnetization with depth.

- In state **1** and **3** a signal has been put on the tape using a recording head with a gap of 250 nm. The magnetic field generated by this head varies with depth. As the tape moves along the recording head, the field experienced by the tape also varies with time.

- Metal evaporated tape exhibits an easy axis of magnetization. This easy axis of magnetization becomes more in-plane with depth. This effect results in an increase of the magnetization in states **1** and **3** with depth.

Apparently the interplay between the three effects described above gives rise to the profile in state **1** and **3** given in Figure 6.21. This indicates that at the surface the anisotropy effect has the largest influence on the magnetization profile in these states, while on the substrate side the demagnetization by voids, or a decay of the applied field with depth, has a larger influence on the magnetization.

In Figure 6.23 Γ_m of state **1** and state **3** divided by Γ_m of state **6** is given. The figure shows which fraction of the saturation magnetization as function of depth is obtained when writing on the tape with a recording head. This fraction exhibits a maximum at 60 nm depth.

6.5.3 Magnetic Depth Profile of the Two-layer Tape

Similar to the one-layer tape also for the two-layer tape the quotients Γ_m/Γ_n in different magnetic states as a function of depth are given in Figure 6.24. In Figure 6.25 Γ_m in state **1**, **3** and **7** normalized to Γ_m in state **6** are given. From Figure 6.20 it is clear that it is reasonable to assume that the two-layer tape is saturated in state **6**.

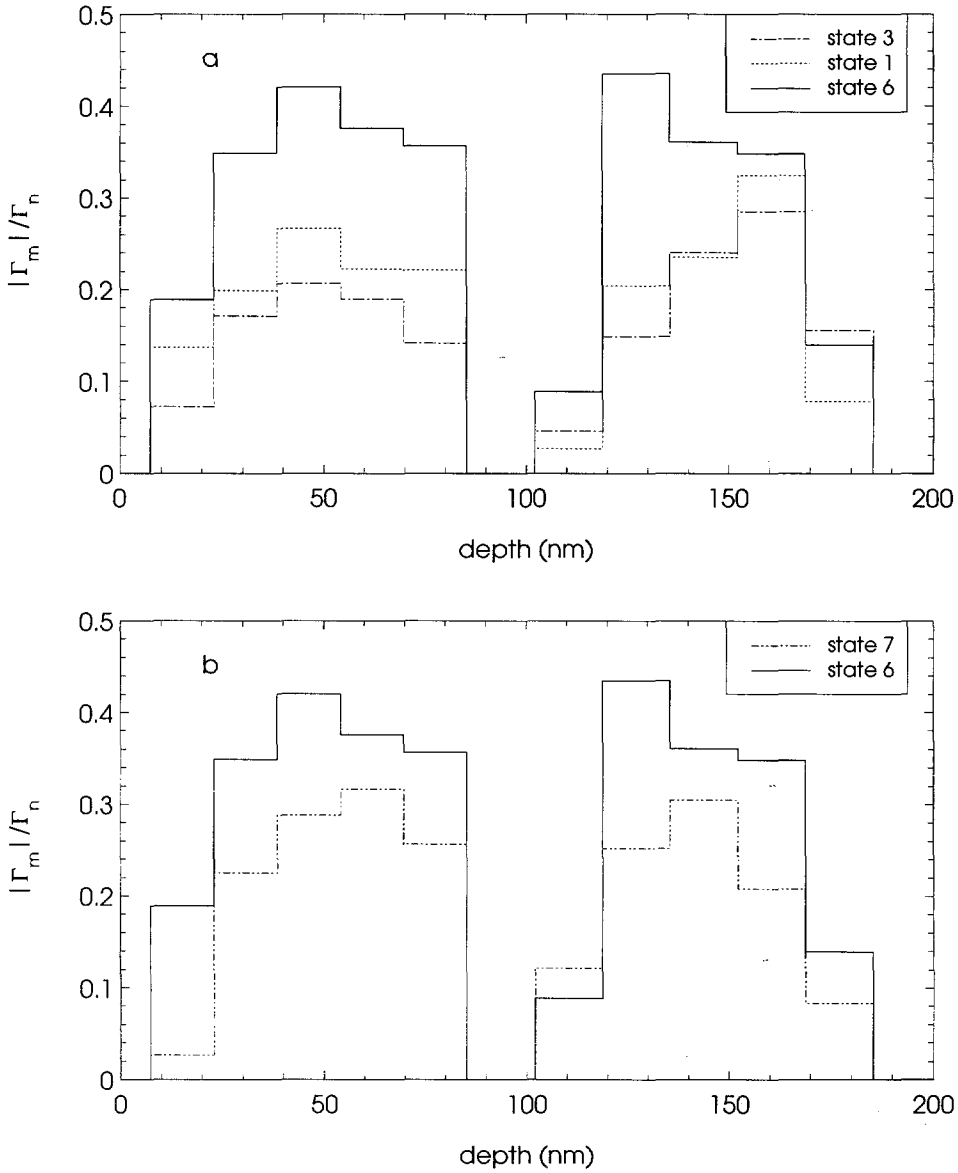

Figure 6.24: *The quotient* $|\Gamma_m|/\Gamma_n$ *of the two layer tape for magnetic state* **1**, **3**, **6** *(figure a) and* **6** *and* **7** *(figure b) as a function of depth.*

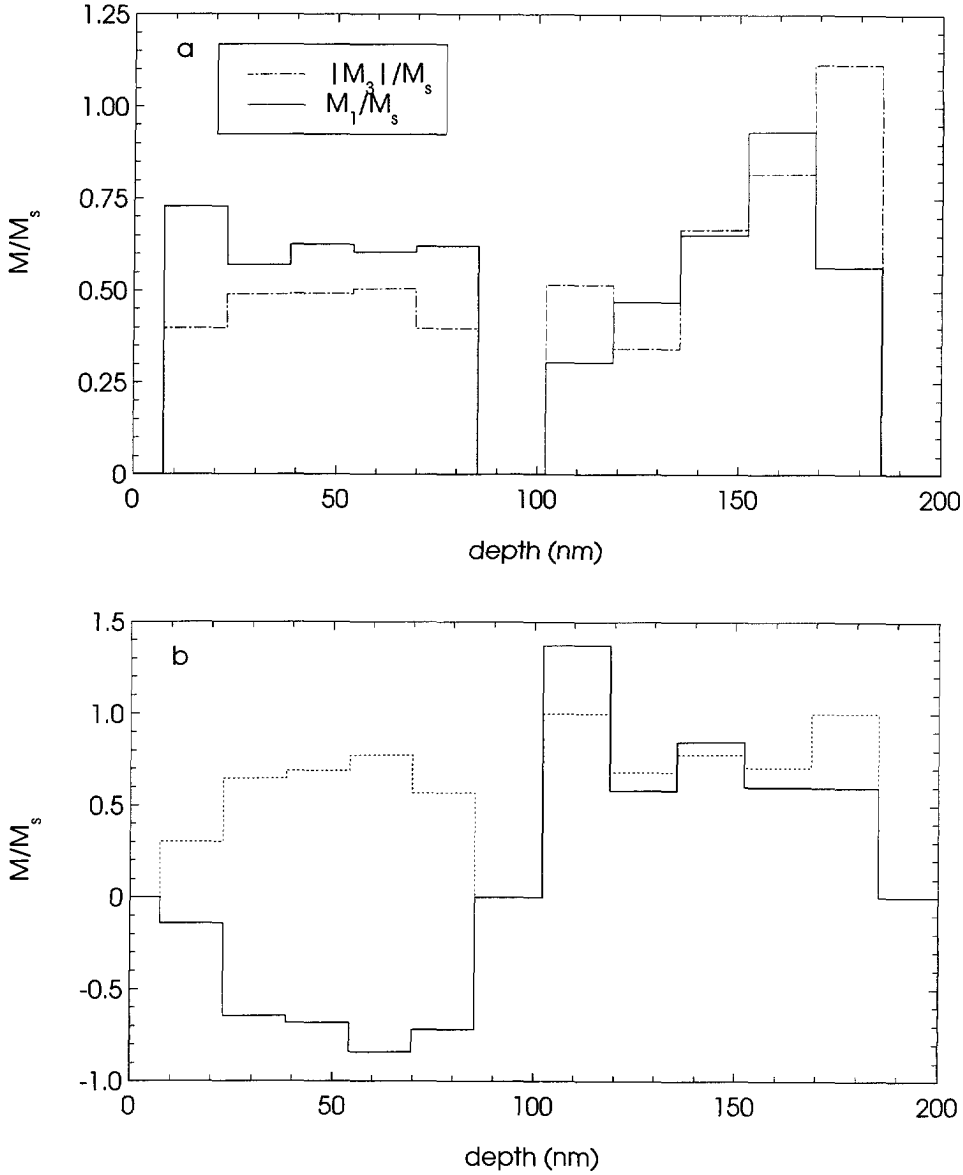

Figure 6.25: *The quotient of Γ_m in state* **1**, **3** *(Figure a), and state* **7** *(Figure b), both divided by Γ_m in state* **6**, *in Figure b the solid line represents the actual value of Γ_m in state* **6** *normalized to Γ_m in state* **7** *and the dotted line represents the absolute value of this quotient (when the quotient becomes larger than 1 it is assumed to be equal to 1).*

From Figure 6.24a it is clear that the shape of the magnetization profile in the upper layer after writing a signal resembles the shape of the magnetization profile in state **6**. In the bottom layer this resemblance does not occur: after writing a signal by a recording head a clear increase of Γ_m with depth is observed, which does not occur in state **6**. A possible explanation could be magnetostatic interactions between both layers. However, in the literature, it is stated that the two layers behave as magnetically independent layers [45]. Also the magnetization curve of the two-layer tape can be described well by assuming no magnetostatic interaction between both layers and the magnetic properties of a one-layer tape for both layers [40]. In Figure 6.26 the relative composition of the two-layer tape as a function of sputter time as obtained by Auger analysis is given. At the interface of the two sputtered layers more oxygen is determined. The increased amount of oxygen is probably the cause of the non-magnetic region, resulting in no significant magnetic interaction between both layers. Moreover it is not expected that magnetostatic interactions between the two layers will influence the magnetization profile, obtained by writing a signal by a recording head, of one layer much more than of the layer.

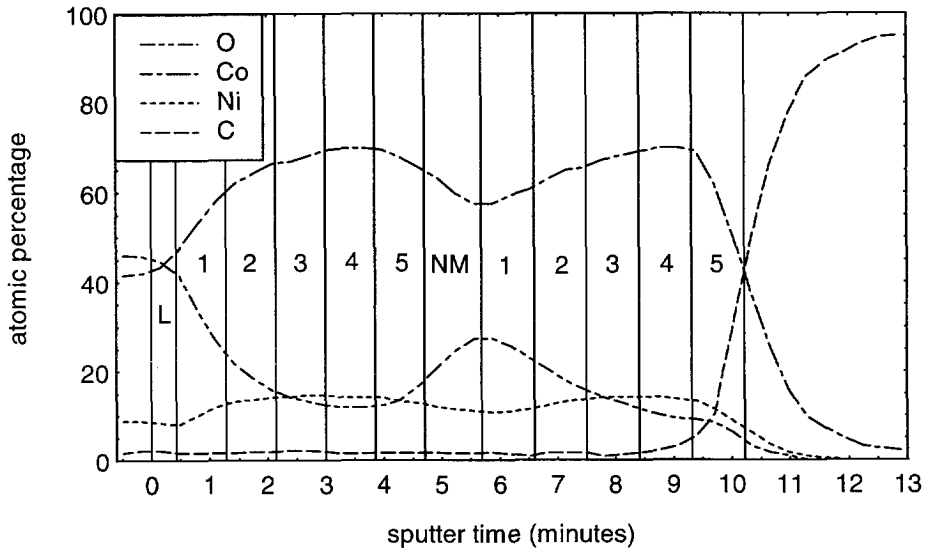

Figure 6.26: *The atomic percentage as determined by Auger analysis as a function of sputter time. During the Auger analysis small amounts of the sample are removed, so the sputter time is a measure for the depth. The vertical lines correspond to the slabs of the model fitted to the PNR-data (see Figure 6.19), assuming the crossing between Co and C concentration corresponds to the boundary between magnetic area and PET-substrate. 'L' denotes the lubricating layer and 'NM' the non-magnetic region.*

A more likely explanation for the increase of Γ_m with depth in the lower layer after writing a signal with the recorder head can be found in the history of the recording process. When the tape moves along the recording head the bottom layer is first magnetized by a field parallel to its easy axis, but it is finally magnetized by a field which 'crosses' the easy axis of the bottom layer, which results in a decrease of the magnetization in this layer. For clarity a schematic view of the writing mechanism on the two-layer tape is given in Figure 6.27.

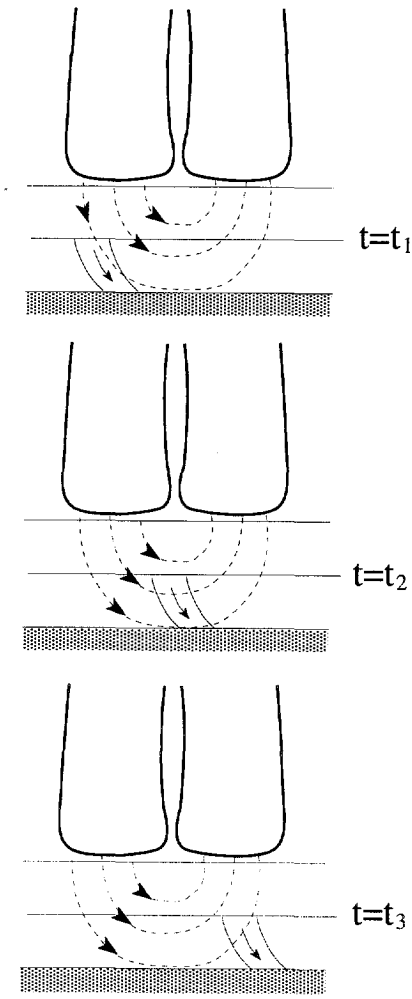

Figure 6.27: *The writing process by a recording head at successive moments.*

6.5.4 Interlayer Variations of the Two-layer Tape

For the investigated magnetic states, the average magnetization in both layers of the two-layer tape is calculated from the fitted model and given in Table 6.3. For <M> of each layer s is calculated taking variances and covariances into account. The inaccuracies of <M> for the whole tape are obtained by quadratic summation of the relative inaccuracy of <M> of the single layers.

In state **6** the magnetization of the upper layer is considerably larger than of the lower layer. As the two layers are magnetically independent, this indicates a different M_s for the two layers. In the literature interlayer variations of magnetic properties are reported [45, 46]. When an in-plane magnetic field is applied, an out of plane magnetic component (M_y in Figure 6.20) is reported [46]. When the two non-interacting layers are identical this component should be zero. Bernard and Stupp [46] explain their measured curves by an increase of both M_sT and the coercive field H_c for one layer and a decrease of M_sT and H_c for the other layer, with T the layer thickness. They give changes in the value of M_sT of + and - 13 % and in the value of H_c of + and - 6.9 %, compared to the average values of these quantities. From the work presented here it can be concluded that the upper layer has a larger M_s. The thickness of the upper layer is 78 nm and of the lower layer 82 nm, resulting in a difference of + and - only 2.5 % compared to its average value. The difference in M_sT in state **6** is + and - 7 %, considerably lower than calculated [46]. According to the work performed by Bernard and Stupp [46] the upper layer should also exhibit a higher H_c.

Neutron depolarization experiments have been performed on the two-layer tape [45]. From these experiments a value for the quotient of $\int M_s dT$ of both layers of 0.88 is found. The accuracy of this value is 0.02 [47]. The neutron depolarization experiments could not distinguish whether the value of $\int M_s dT$ of the upper or the lower layer is larger. This quotient is also calculated from the values in Table 6.3 and the thickness of the two layers in the model (Figure 6.19). In this way a value of 0.87 ± 0.05 is found, in good agreement with the value determined by [45].

To obtain a larger value for H_c and M_s the oxygen content and the magnetic packing fraction have to increase simultaneously [46]. In Figure 6.26 the relative composition as a function of sputter time as determined from Auger analysis is given. The position of the slab interfaces as given in this figure, are again estimated, with the assumptions mentioned at the beginning of section 6.5.2. Since the composition variations with depth are larger for the two-layer tape than for the one-layer tape, the assumptions are less likely to be truth than in the case of the one-layer tape. However, the Auger-data in Figure 6.26, indicate that the upper layer contains indeed more oxygen than the lower layer. The average of Γ_n of the two separate layers, as fitted to the PNR-data is equal within the accuracy (upper layer 0.00484(2) nm^{-2} and lower layer 0.00485(2) nm^{-2}). This is not in agreement with the statement of [46] that the layer with higher M_s and H_c should exhibit a larger packing density. In Figure 6.19 it can be seen that the lower layer exhibits larger differences in Γ_n than the upper layer. From comparison of both

Table 6.3: *Comparison of magnetization of the separately sputtered layers of the two-layer tape. To calculate the average magnetization over the whole the tape, the integrated magnetization was divided by the sum of the thicknesses of the two separately sputtered layers and the non-magnetic layer.*

magnetic state	$<M>_{PNR}$ total thickness (kA/m)	$<M>_{PNR}$ upper layer (kA/m)	$<M>_{PNR}$ lower layer (kA/m)
1	222±10	276±7	227±7
2	10±9	10±8	13±6
3	-191±11	-206±7	-226±8
6	356±18	443±12	363±13
7	-6±27	-288±20	259±18

fitted models and the Auger data of both tapes, an increase of oxygen seems to coincide with an increase in Γ_n. This is understandable, as the neutron scattering length divided by a cube with an edge of two times its atomic radius is 3 times as large for oxygen than for nickel or cobalt. One can also see that the lower and upper layer both have an increasing oxygen amount from the substrate side towards the surface side. From comparison between the Auger figure and the fitted model, it is clear that at the substrate side of each layer, with relatively little oxygen and therefore more magnetic material, the lower layer has a lower Γ_n than the upper layer. Probably this results in the larger value of M_s averaged over the upper layer. However, as the elements occur in the tapes in different phases (closed packed, amorphous, oxides), it is difficult to extract more conclusions from the Auger-data.

The average magnetization in state **1** of 222 kA/m is larger than the average magnetization in state **3** of 191 kA/m (see Table 6.2). This is mainly due to the larger magnetization in the upper layer (276 kA/m in state **1** and 206 kA/m in state **3**), see also Figure 6.25. An explanation for the much smaller in-plane magnetization in state **3** is the magnetic history and the coercive field of the upper layer. In state **1** the tape has no magnetic history and is therefore easily magnetized, however in state **3** the magnetization has to overcome the coercive field (see Figure 6.28).

It is tempting to assume that the H_c of the upper layer could be overcome easily by the field applied by the recording head, as it is closer to the recording head than the lower layer. However, the writing process is rather complicated. Both the magnitude and the direction of the magnetization vary with depth and time as the tape moves along the recording head, as schematically shown in Figure 6.27. From Table 6.3 it is clear that H_c of the upper layer is not reached when writing an opposite signal on an already written tape.

Table 6.3 shows that the average in-plane magnetization in the lower layer in

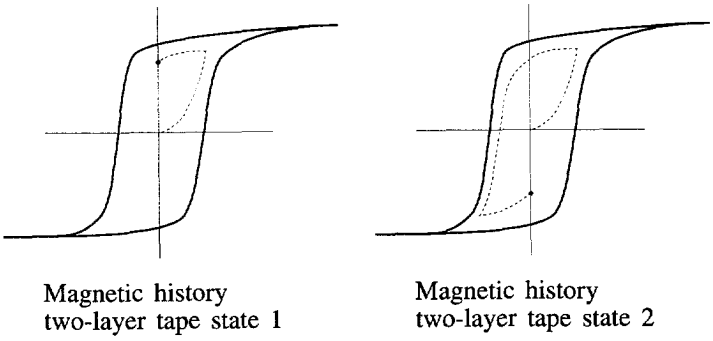

Figure 6.28: *Magnetic history of state* **1** *and* **3** *compared.*

state **7** is larger than state **1** and **3**, where the tape is magnetized in the in-plane direction by the recording head. This can be explained by the fact that the field produced by the recording head, which is last experienced by the two-layer tape is almost perpendicular to the easy axis of magnetization of the lower layer (see Figure 6.27). As argued in section 6.5.2 this will reduce the in-plane magnetization especially in the upper part of the lower layer.

6.6 Conclusions

From the performed PNR-experiments on videotapes the following conclusions are drawn:

- The measured PNR-curves can well be described by the models given in Figure 6.11 and Figure 6.19.
- The thickness of the tapes as obtained from the models fitted to the PNR-data agree very well with TEM-results. The average magnetization calculated from the model fitted to the two-layer tape agrees very well with VSM-results. For the one-layer tape the VSM-results were used to choose the presented boundary-model.
- Bulk demagnetization and DC demagnetization by a recording head both result in an in-plane magnetization component of approximately zero over the whole depth of the tape.
- A recording head writes throughout the whole depth of both investigated ME-tapes.
- The model fitted to the data measured on the two-layer tape indicates that this tape contains a non-magnetic region between the two sputtered layers.

- For the two-layer tape it is determined that $\int M_s dT$ is larger for the layer at the surface side than for the layer at the substrate side. This difference is determined by the difference in M_s of both layers.
- From the fitted model it is clear that the value of Γ_n increases during a sputter shift.
- An upper estimate for the voids fraction of 46 % for the one-layer and 51 % for the two-layer tape is determined.
- PNR-data of the one-layer tape are difficult to interpret without additional information, as in this case e.g. VSM-measurements. Probably investigation of tapes consisting of more layers will be more promising, as the PNR-curves will contain more detail. Nowadays tapes sputtered in three or even four shifts are available. PNR can be used to determine interlayer variations in magnetic properties of such tapes.

Chapter 7

PNR on Fe/Si multilayers

7.1 Interest in Fe/Si multilayers

The improved technology in producing thin layers made it possible to study the interaction of thin ferromagnetic layers separated by non-magnetic layers. Last years a lot of research has been performed on multilayers consisting of ferromagnetic layers separated by a non-magnetic metallic material. In particular the coupling between the magnetic layers and magnetoresistance effects were subjects of study. The best known examples are Fe/Cr-multilayers. These Fe/Cr-multilayers exhibit an oscillatory exchange coupling and magnetoresistance, and the presence of areas of biquadratic coupled regions is undoubtedly determined by Kerr-measurements on a sample with a wedge-shaped chromium interlayer [48]. The exchange coupling in multilayers with metallic spacers is nowadays well understood. Bruno [49] has written a review in which all mechanisms that are supposed to cause exchange coupling are described.

The coupling in multilayers in which ferromagnetic layers are separated by semiconducting layers is not yet clearly understood. This was the initial motivation to study magnetic coupling in Fe/Si multilayers.

In 1992 Toscano *et al.* [50] reported a very weak oscillatory exchange coupling in low temperature evaporated Fe/Si/Fe sandwiches, in which the silicon spacer has an amorphous structure. In 1992 an antiferromagnetic coupling was reported by Fullerton *et al.* [51] in Fe/Si multilayers. These multilayers were sputtered at room temperature, resulting in a spacer layer of a crystalline silicide. The experiments described in this chapter are performed on samples also sputtered at room temperature and with crystalline spacer material.

Mattson *et al.* [52] reported that the antiferromagnetic coupling in Fe/Si multilayers produced in the latter way, converted to a ferromagnetic one during cooling and could be restored by laser irradiation. They explained this result by excitation of charge carriers in the spacer by light induction. This phenomenon of light induction made these layers interesting for the optoelectronic industry and invoked more research into spacer layer thickness and temperature dependences of the an-

tiferromagnetic coupling. However, later publications reported the restoration of the antiferromagnetic coupling to be caused by a local laser heating effect and not to be associated with photogeneration of carriers [53, 54].

Fullerton and Bader [53] explained the strong temperature dependence of the antiferromagnetic coupling in such multilayers by a strongly temperature dependent biquadratic coupling(also called 90°-coupling). In Figure 7.1 the alignments favoured by the different coupling mechanisms: ferromagnetic, antiferromagnetic

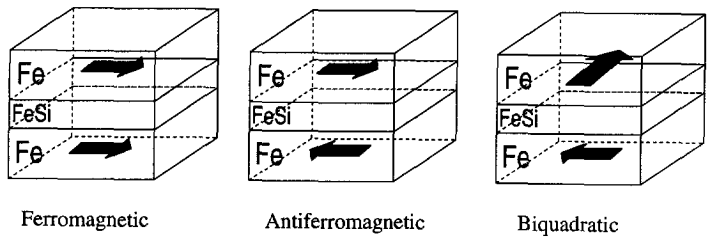

Figure 7.1: *Schematic view of the different alignments favoured by the three possible coupling mechanisms through the spacer: ferromagnetic, antiferromagnetic and biquadratic.*

and biquadratic, are schematically presented. Although the hysteresis curves measured at different temperatures can indeed be described using the following relation:

$$E_{ex} = -J_1 \frac{\vec{\mathbf{M}}_1 . \vec{\mathbf{M}}_2}{|\vec{\mathbf{M}}_1||\vec{\mathbf{M}}_2|} - J_2 \left(\frac{\vec{\mathbf{M}}_1 . \vec{\mathbf{M}}_2}{|\vec{\mathbf{M}}_1||\vec{\mathbf{M}}_2|} \right)^2 , \tag{7.1}$$

with E_{ex} the interlayer exchange energy, M_1 and M_2 the magnetization in adjacent ferromagnetic layers, and $J_1(J_2)$ the bilinear (strongly temperature dependent biquadratic) coupling parameter, no direct proof for a biquadratic coupling in Fe/Si multilayers exists. Fullerton and Bader suggest that compositional fluctuations in the silicide spacer layers cause the biquadratic coupling. But it is unclear why such compositional fluctuations should result in a large temperature dependence of J_2.

Later experiments [55, 56], however, show that the applied magnetic field at which magnetic saturation is reached strongly increases with stronger temperature. Therefore, the antiferromagnetic (AF) exchange coupling strength increases with decreasing temperature, and does not decreases as was wrongly concluded in the literature [52, 57].

Also experiments are performed on Fe/Si multilayers, with crystalline silicide spacer, of which the number of bilayers varied [58, 59]. These experiments showed that the overall magnetization as measured by VSM behaves less ferromagnetically when the number of bilayers of the sample increases. These results indicate a depth-dependence of the magnetic alignment in such Fe/Si multilayers. We performed PNR measurements on Fe/Si multilayers to investigate the depth-

dependence of the magnetic alignment, in order to understand more of the magnetic coupling in those multilayers.

7.2 Description of the Experiments

Four samples were produced by dc-magnetron sputtering ($p_{base} < 5 \times 10^{-5}$ Pa) in an argon atmosphere of 1 Pa on oxidized Si or glass substrates at a temperature of about 50 °C. The multilayers for which Kohlhepp *et al.* [58] determined that the amount of antiferromagnetic coupling increases with the number of bilayers were produced under exactly the same circumstances. The nominal Si spacer thickness was 1.1 nm or 1.4 nm and the nominal Fe thickness 3.0 nm. Each multilayer contained 20 bilayers.

PNR-curves of the multilayers on Si were measured at an angle of incidence of about 12.4 mrad at increasing magnetic fields ranging from 0 to 690 kA/m. To check a possible influence of the type of substrate on the depth profile also measurements were performed on the sample with 1.4 nm Si deposited on glass, at the same angle of incidence. All measurements were performed on ROG [17], the time-of-flight (TOF) neutron reflectometer of IRI in Delft.

Small angle XRD-experiments were performed to determine the modulation length of the multilayers, large angle XRD-experiments were performed to determine the crystal structure and the perpendicular coherence length of the multilayers.

For all samples the magnetization as a function of applied field has been measured by VSM-experiments. For the samples deposited on glass the hysteresis curves were measured on top and bottom side by the magneto-optical Kerr effect (MOKE).

7.3 Results and Interpretation

In Figure 7.2 simulated neutron reflectivity curves of a perfect ferromagnetically aligned Fe/Si multilayer and a perfect antiferromagnetically aligned Fe/Si multilayer are given. From this figure it is clear that the magnetic repetition period is twice as large for the antiferromagnetically aligned sample than for the ferromagnetically aligned sample. This results in an extra Bragg peak corresponding to this magnetic repetition period.

Figures 7.3 through 7.6 give the polarized neutron reflectivity results of the different samples. In all these figures a Bragg peak occurs around 0.45 and 0.47 nm^{-1} for the 1.4 and 1.1 nm Si samples, so the samples all contain a region of antiferromagnetic coupling. The measured Bragg peak is rather broad. This indicates irregularities in the repetition of the neutron scattering length density. The fact that the Bragg peak in the data of the 1.4 nm Si on silicon sample in Figures 7.4 and 7.5 occurs at larger q than for the simulated data presented in Figure 7.2 is caused by a smaller than nominal bilayer thickness.

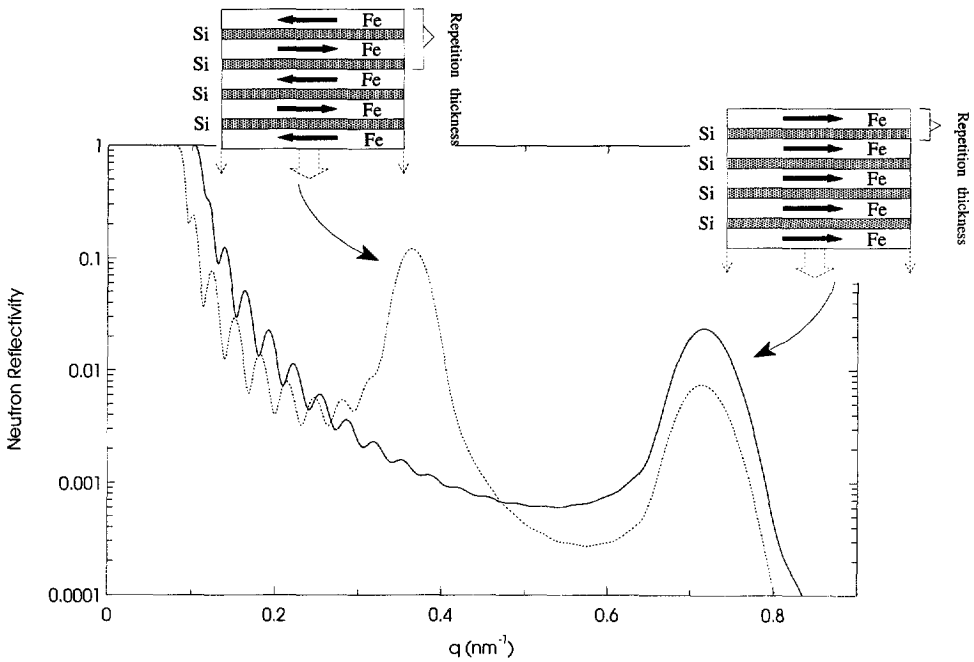

Figure 7.2: *Simulated spin parallel neutron reflectivity data for perfectly ferromagnetic (solid line) and antiferromagnetic (dashed line) alignment of the 1.4 nm Si on silicon sample.*

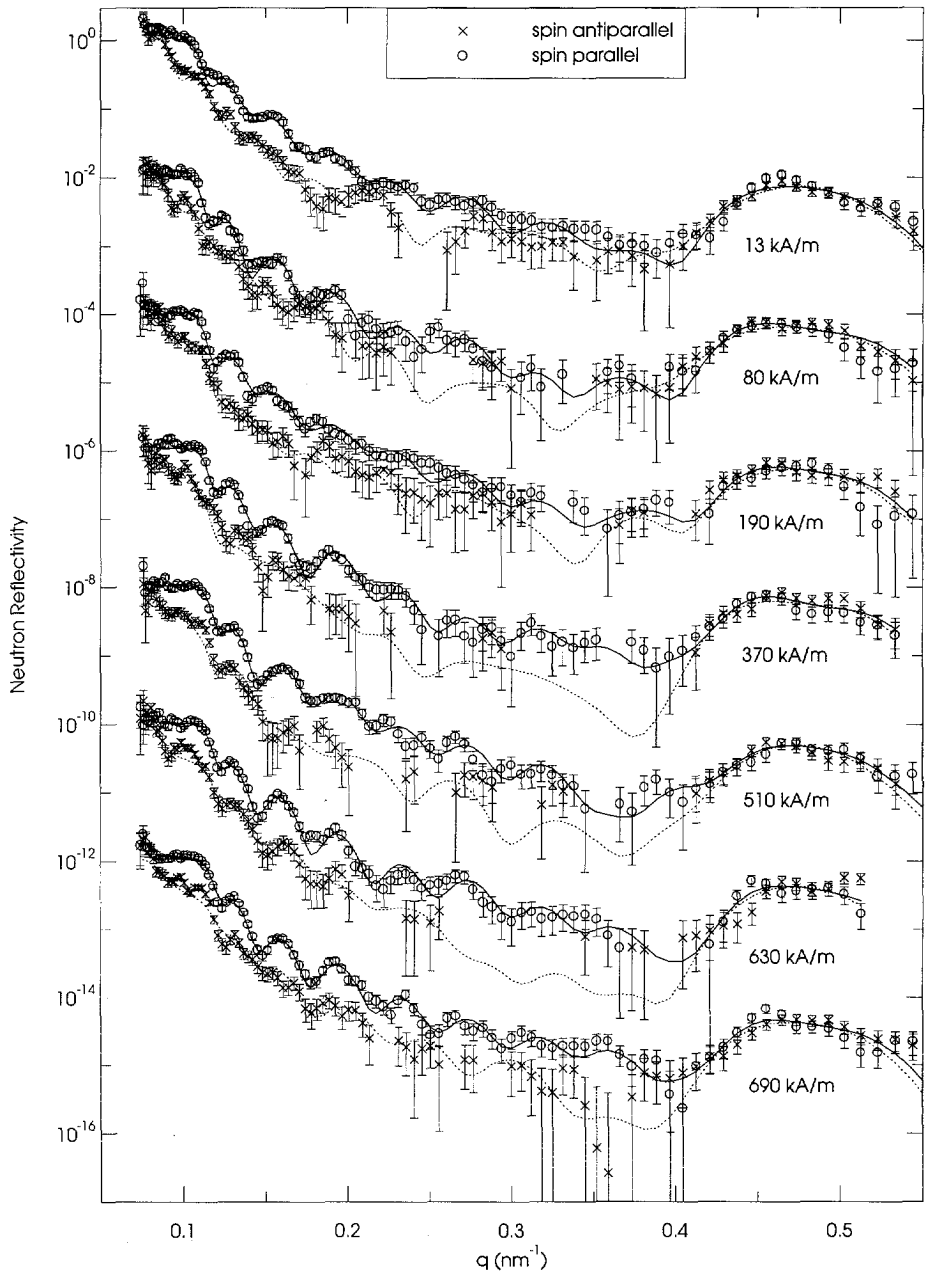

Figure 7.3: *Neutron reflectivity curves, divided by increasing powers of 100, of the 1.1 nm Si sample on silicon. The measured data are represented by symbols. The full (dashed) curves represent the spin parallel (antiparallel) simulated data.*

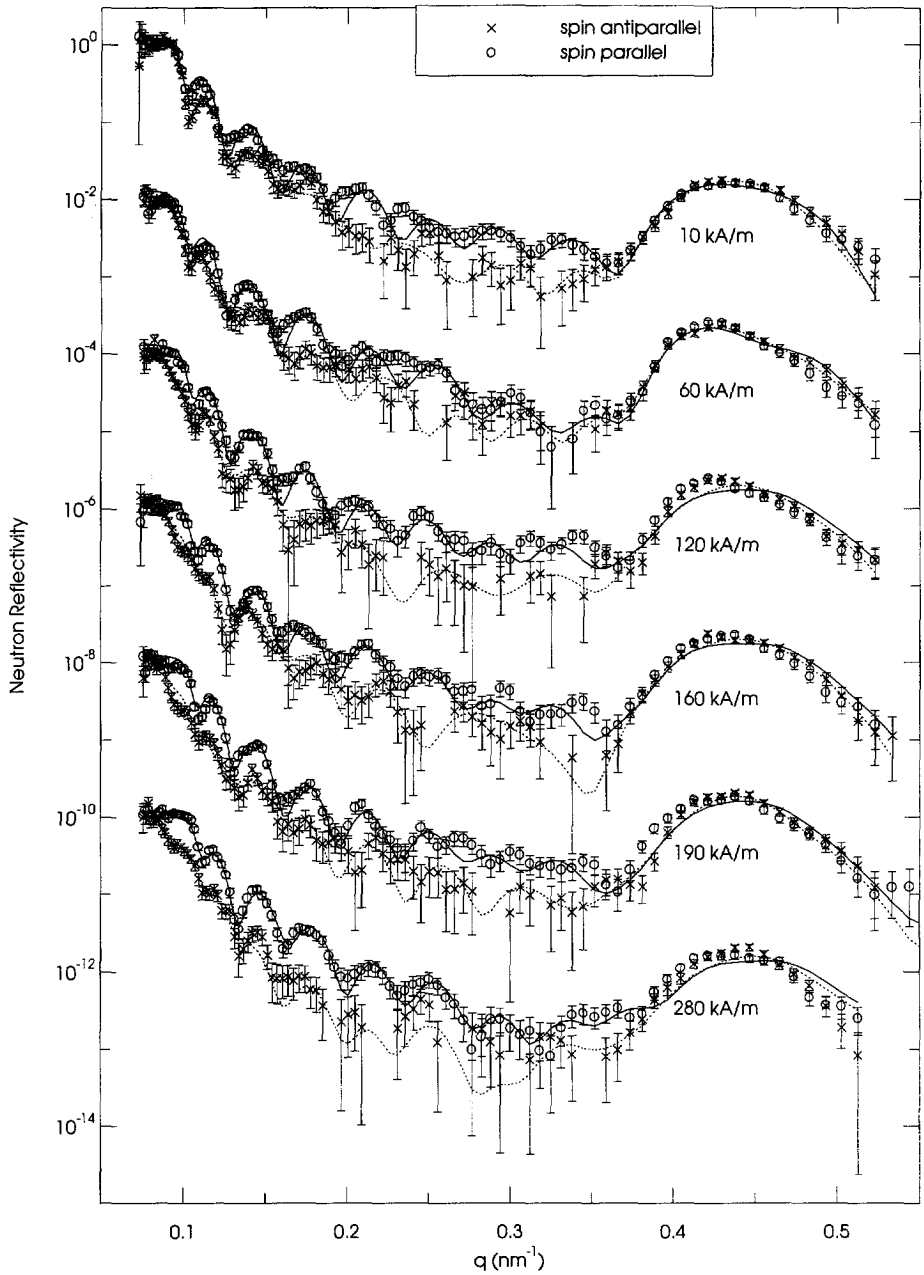

Figure 7.4: *Neutron reflectivity curves, divided by increasing powers of 100, of the 1.4 nm Si sample on silicon at magnetic field values from 10 up to 280 kA/m. The measured data are represented by symbols. The full (dashed) curves represent the spin parallel (antiparallel) simulated data.*

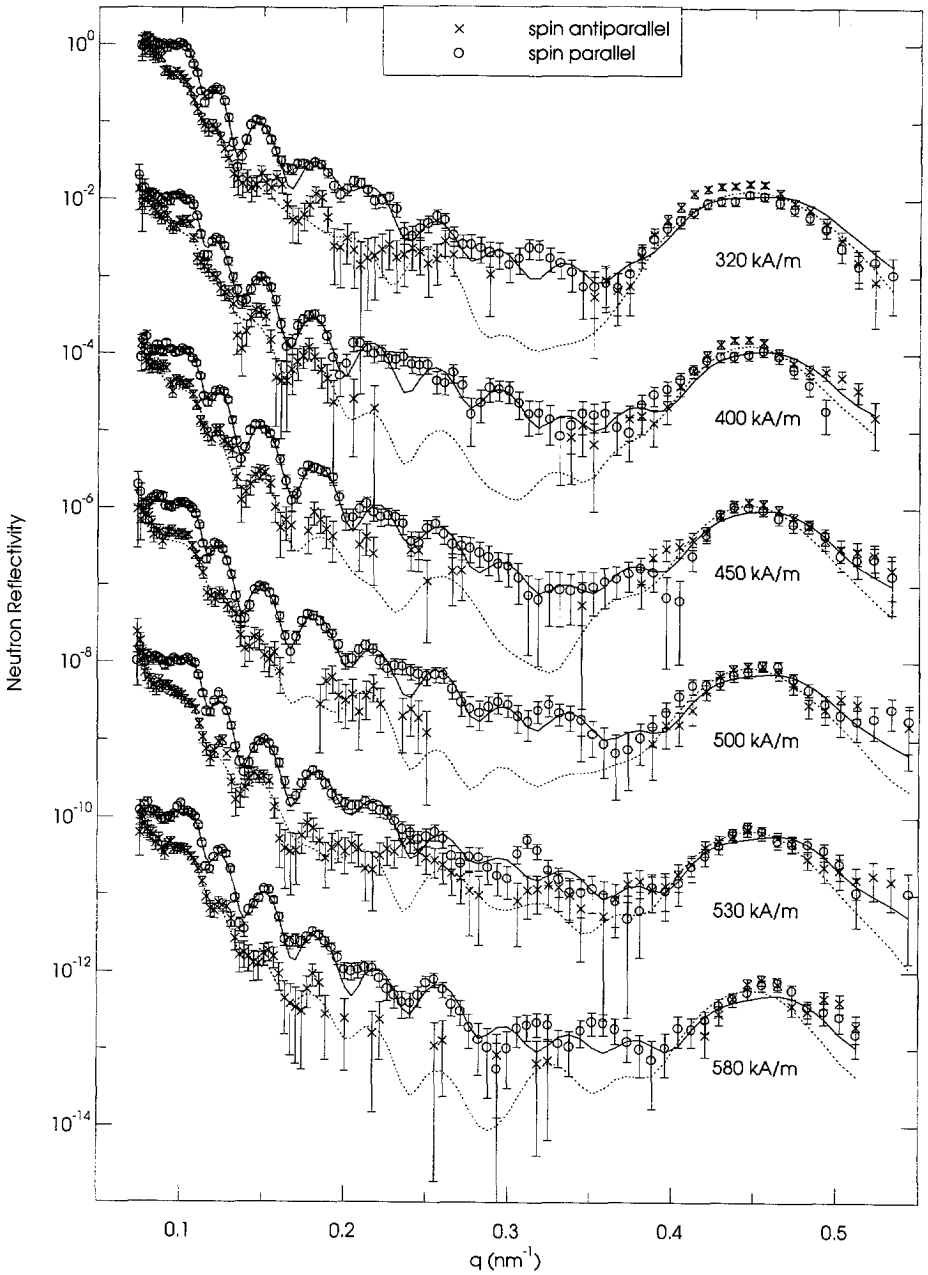

Figure 7.5: *Neutron reflectivity curves, divided by increasing powers of 100, of the 1.4 nm Si sample on silicon at magnetic field values from 320 up to 580 kA/m. Measured data are represented by symbols. The full (dashed) curves represent the spin parallel (antiparallel) simulated data.*

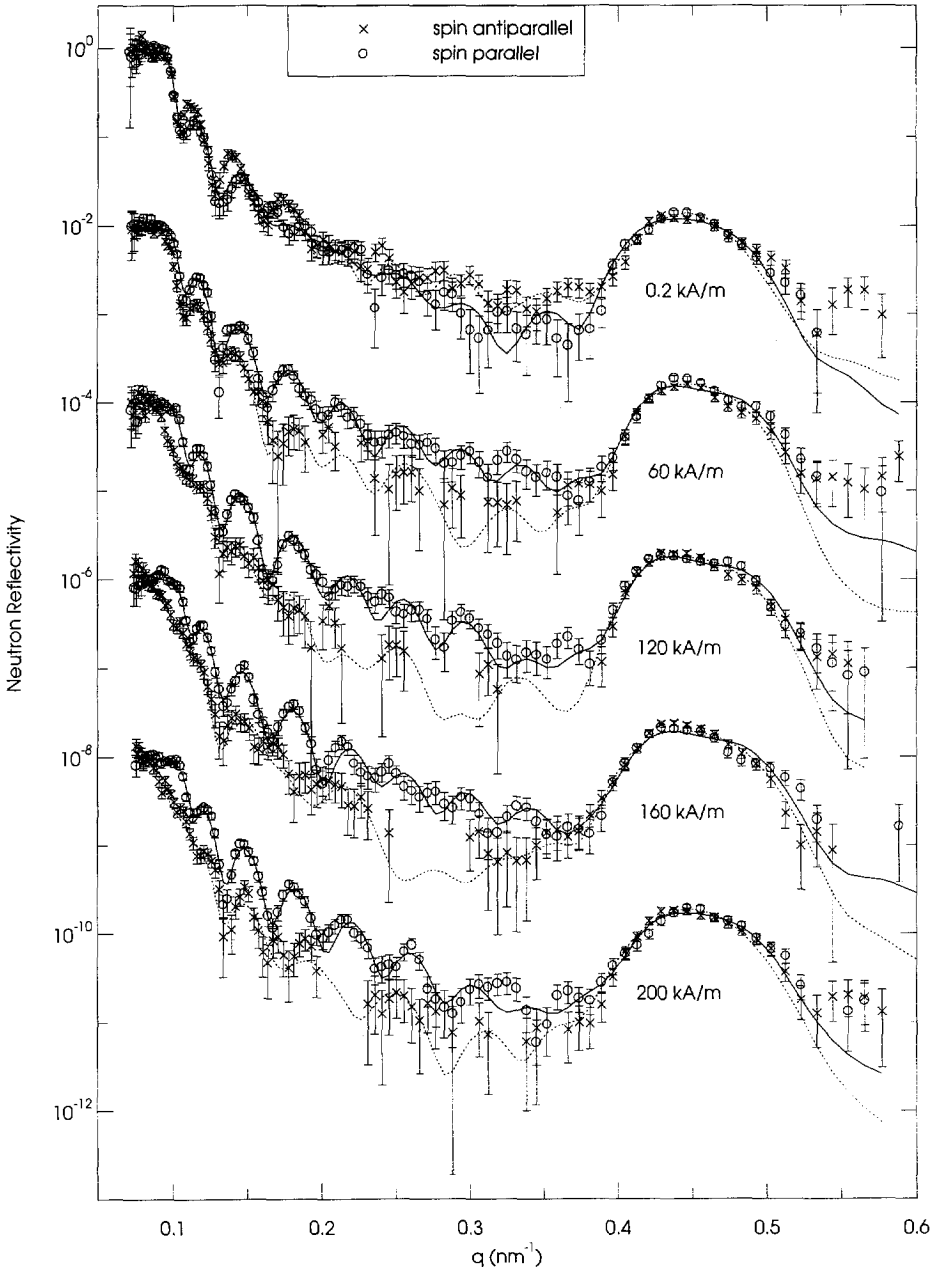

Figure 7.6: *Neutron reflectivity curves, divided by increasing powers of 100, of the 1.4 nm Si sample on glass. Measured data are presented by symbols. The full (dashed) curves represent the spin parallel (antiparallel) simulated data.*

The results of the MOKE-experiments are given in Figure 7.7. From these measurements it is clear that the topside of the sample behaves more antiferromagnetically than the substrate side of the sample. This indicates a depth-dependence of the magnetic coupling. This depth-dependence can be responsible for the width of the antiferromagnetic Bragg peaks.

To investigate objectively the magnetic alignment as a function of depth, Γ_m in each iron layer is allowed to vary independently during fitting to the PNR-data. In first instance the data were fitted with a perfect repetition of the nuclear profile, while the magnetic scattering length density is free in each iron layer. This resulted in models published in [60]. These models showed that at low fields the magnetization in the Fe-layers was predominantly aligned antiferromagnetically at the surface side and ferromagnetically at the substrate side. When the magnetic field was increased the region of ferromagnetic alignment increased.

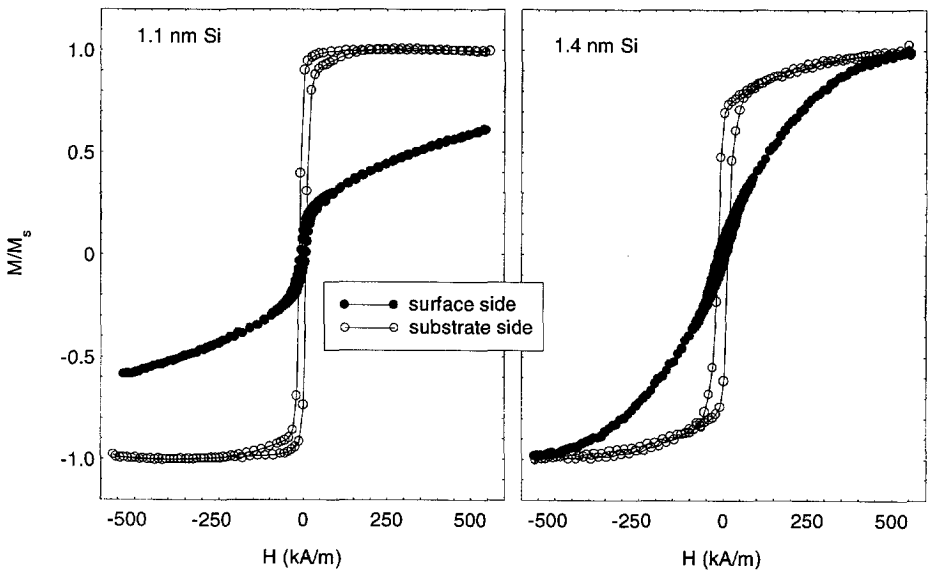

Figure 7.7: *Magnetization curves as measured by MOKE [61] of both sides of the samples on glass. Note that the magnetization curve measured at the top side of each sample behaves more antiferromagnetically than the magnetization curve at the substrate side of the sample.*

The agreement between the integrated product of the magnetization and the magnetic volume [60], as determined by VSM and as calculated from the described model, was bad for the 1.4 nm Si sample on silicon. This product calculated from the PNR-model was only 70 % of the value determined by VSM. The too low value of Γ_m integrated over the depth is probably caused by the model fitting a wrong

Γ_n-profile corresponding to a too high average value of Γ_n.

For all measurements the spin parallel neutron reflectivity is measured with much better statistical accuracy than the spin antiparallel data. Therefore, the model fit to the data is predominantly determined by the spin parallel data. As explained in chapter 1, the spin parallel data depend on the sum of Γ_m and Γ_n. Therefore an interchange between Γ_m and Γ_n will not affect the fit to the data much, but will result in bad agreement with the VSM-data.

As it was not possible to remeasure the data with better statistics because of available time and deterioration of the sample, the data were fitted again, assuming a Γ_n-profile with a lower average value. The data measured at the different magnetic fields were fitted simultaneously, keeping the Γ_n-profile equal for all magnetic fields and the Γ_m-profiles variable with the different fields. When agreement between the product of magnetization and magnetic volume obtained from PNR and from VSM was achieved, the simulated Bragg peak was narrower than the measured one, as shown in Figure 7.8. This indicated not only Γ_m but also Γ_n to be depth-dependent.

Fitting the data with a model in which the sample is divided into three regions in which the nuclear profile was exactly repeated, indicated the nuclear scattering density to become larger during sputtering. Model refinement resulted in an increase of Γ_n with thickness of the multilayers and the thickness of the spacer layer to decrease with thickness.

As the depth-dependence of Γ_n improved the fit to the data for the 1.4 nm Si on silicon sample, also the data measured on the other two samples were fitted using such a model. For the 1.1 nm Si on silicon sample this model resulted in a slightly better fit to the data and better agreement with the VSM-measurements. For the 1.4 nm Si on glass sample a slightly better fit to the data and a slightly better agreement with the VSM-results were found. So for all three samples the correspondence between measurements and calculation improves when Γ_n increasing with thickness is assumed. Such an increase of scattering length density is probably caused by the layer becoming more perfect during the sputtering process, i.e. fewer structural irregularities like vacancies, grain boundaries and pinholes occur.

The obtained models are presented in Figures 7.9 through 7.11. The fitted value of the experimental resolution is 7 % for both 1.4 nm Si samples and 7.9 % for the 1.1 nm Si sample on silicon.

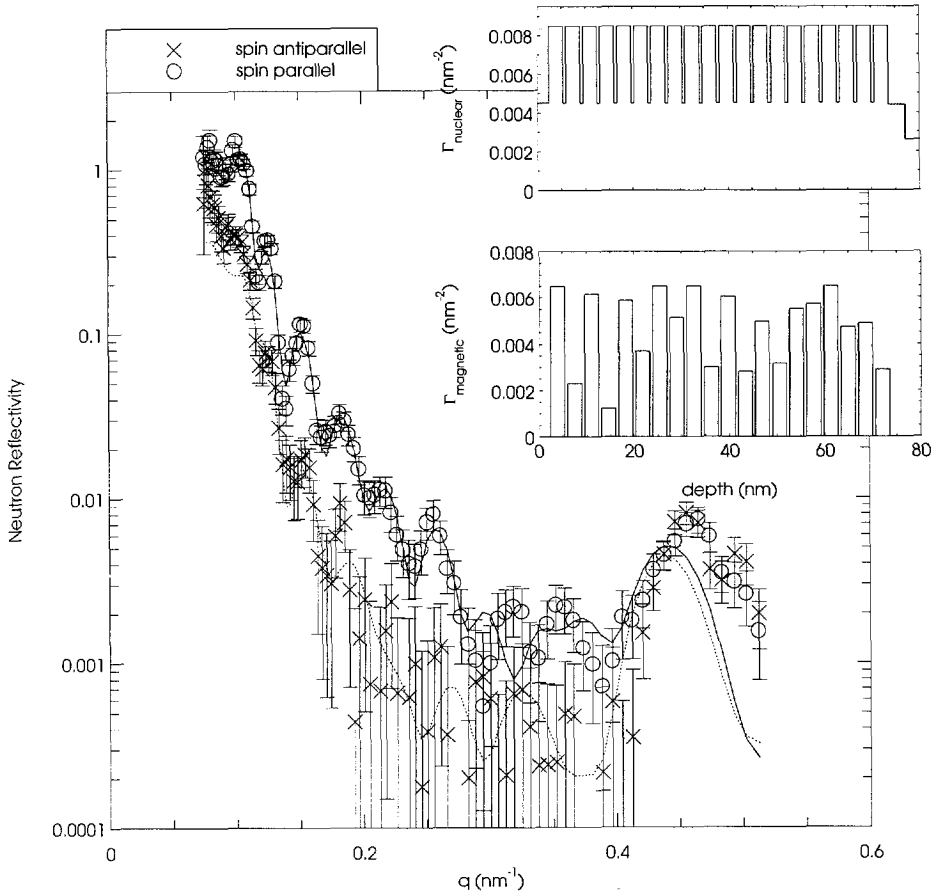

Figure 7.8: *Measured (symbols) and simulated (lines) PNR-data for the 1.4 nm Si sample on silicon at a magnetic field of 580 kA/m. The insert shows the model fitted to the data, supposing that the Γ_n-profile is equal for each bilayer.*

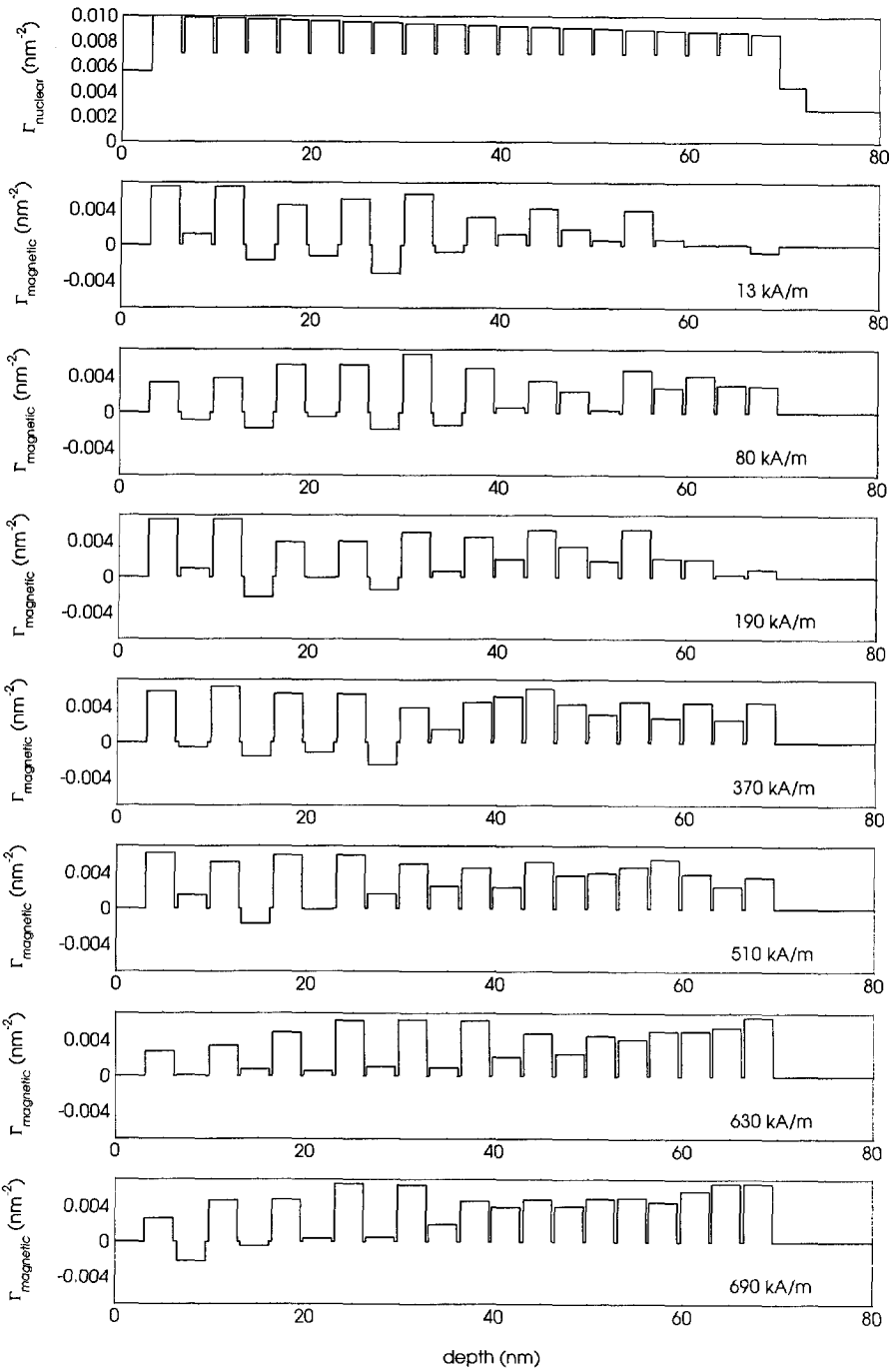

Figure 7.9: *The depth-dependence of Γ_n and Γ_M obtained by fitting to the PNR data at various magnetic fields for the 1.1 nm Si on silicon sample.*

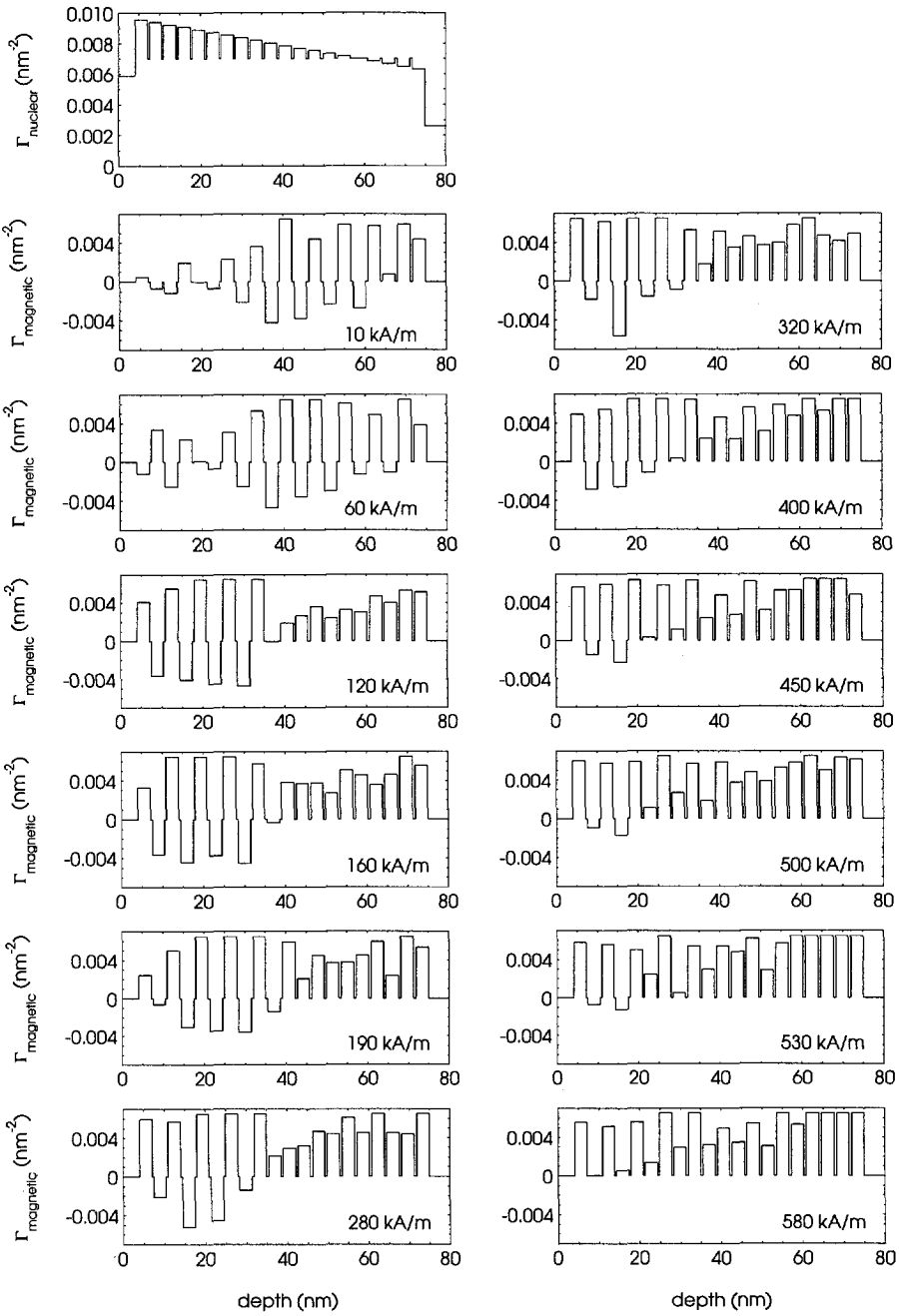

Figure 7.10: *The depth dependence of Γ_n and Γ_m obtained by fitting to the PNR data at various magnetic fields for the 1.4 nm Si on silicon sample.*

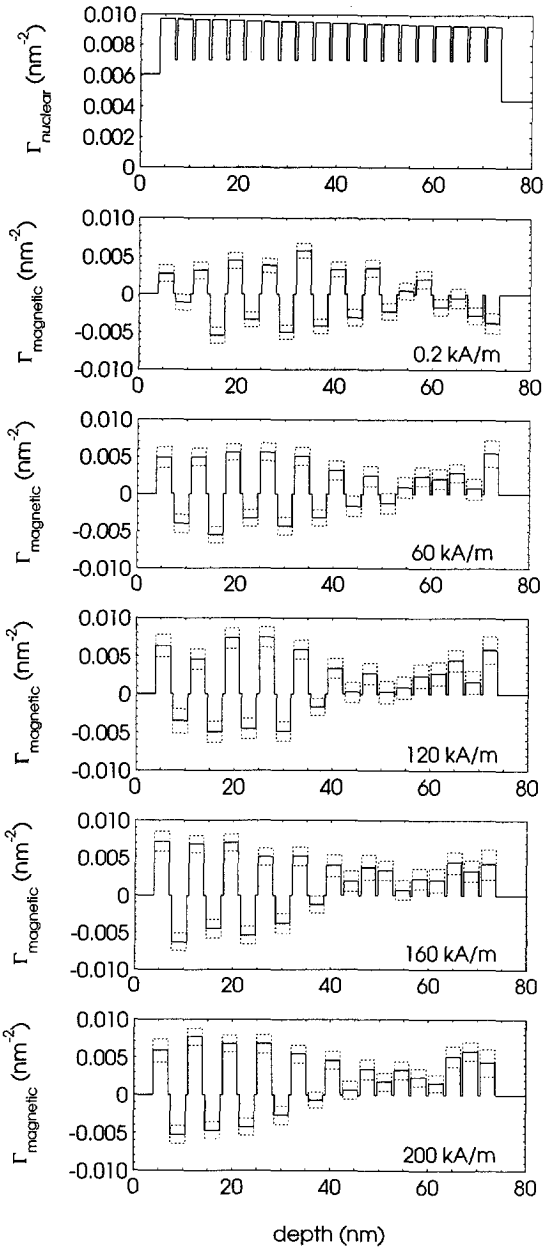

Figure 7.11: *The depth dependence of Γ_n and Γ_m obtained by fitting to the PNR data at various magnetic fields for the 1.4 nm Si on glass sample. The dotted lines give the fitted value of Γ_m plus and minus one standard deviation.*

From small angle XRD the nuclear repetition lengths are determined to be equal to 3.51 (±0.05) and 3.72 (±0.05) nm for the 1.1 and 1.4 nm Si on silicon samples, respectively. For the 1.1 nm Si sample the obtained bilayer thickness is 3.32 nm. For the 1.4 nm Si sample on silicon the obtained bilayer thickness is 3.58 nm. The agreement with the XRD-values is reasonable. The bilayer thickness for the 1.4 nm Si on glass sample determined from PNR is 3.51 nm. The reduction compared to the nominal sputter bilayer thicknesses of 4.1 and 4.4 nm is caused by interdiffusion of Fe into Si. As from the high-angle XRD experiments on these samples a coherence length of about 20 nm perpendicular to the surface is obtained, the spacer is supposed to be crystalline. The most likely candidate for this crystalline phase is the CsCl-structure (B2) FeSi, as the lattice spacing of this structure almost exactly matches the bcc lattice spacing of iron. This metallic FeSi structure is found to be stable in thin films [62, 63]. Mössbauer experiments on Fe/Si-multilayers performed by Dekoster *et al.* [64] also confirm the spacer layer to consist of CsCl-structured FeSi.

The fitted value of Γ_n for the spacer of 7.0×10^{-3} nm^{-2} agrees with the value of 7.3×10^{-3} nm^{-2}, calculated for FeSi in the CsCl-structure.

The value of Γ_n of bulk iron is 1.0×10^{-2} nm^{-2}. The obtained values of Γ_n at the topside of all three samples agree well with this value. As discussed above Γ_n of the iron layers decreases towards the substrate because of an increasing concentration of silicon.

For the 1.4 nm Si on glass sample the values of the standard deviations s, in the values of Γ_m in the different Fe-layers (because of statistical accuracy) are estimated. The dashed lines around the obtained values in Figure 7.11 give the probability range of 68.3 % based on the counting statistics. It was not possible to calculate $s(\Gamma_m)$ for both samples on silicon. When this is tried the parameter estimation routine finds a new minimum in which some values of Γ_m are unrealistically high.

In this chapter a different model fit to the data is presented from that in the earlier published results [60]. However, the trend in the magnetic profiles is the same in both models. Therefore, the conclusions which can be drawn from the models do not differ.

7.4 Comparison with VSM

Figure 7.12 gives the measured magnetization curves for the three samples. In the curves the average magnetization as determined by PNR is also given. For all three samples the agreement is satisfactory.

7.5 Discussion

From the models presented in Figures 7.9 through 7.11 it is clear that at low magnetic field the bottom part of both multilayers exhibit more ferromagnetic

alignment. By increasing the magnetic field, the ferromagnetically aligned volume of the sample increases, reducing the volume of antiferromagnetic alignment.

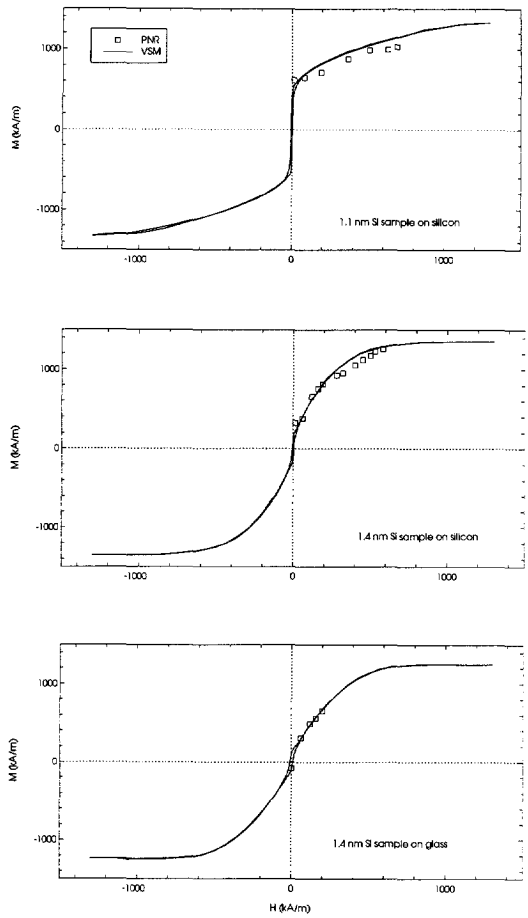

Figure 7.12: *The average magnetization as measured by VSM and as obtained from the profiles fitted to the PNR-data for the different samples.*

The value of Γ_m of bulk iron is 6×10^{-3} nm^{-2}. In Figures 7.10 and Figure 7.11 can be seen that in both samples with a nominal spacer thickness of 1.4 nm, regions occur in which neighbouring iron layers exhibit Γ_m-values of this magnitude with opposite sign. In these regions perfect antiferromagnetic alignment occurs. For both 1.4 nm Si samples this situation occurs at a depth between 15 and 30 nm at low magnetic field values.

As the applied field causes larger changes in the 1.4 nm Si sample than in the 1.1 nm Si sample, the antiferromagnetic coupling strength is larger in the latter one. The negative component of Γ_m is smaller for the 1.1 nm Si sample than for the 1.4 nm Si sample. This might be caused by the presence of a strong bi-

quadratic coupling in the 1.1 nm Si sample. However, a more likely explanation are percolation paths of iron atoms in the spacer short circuiting the magnetization. These percolation paths (here also called pinholes) result in ferromagnetic alignment over a fraction of every Si spacer, reducing the magnetic component antiparallel to the applied field. During sputtering the fraction of pinholes and the degree of FM-coupling across every spacer decreases: therefore the fraction of AFM-coupling increases during sputtering. The 1.1 nm Si sample will contain more pinholes than the 1.4 nm Si, resulting in a larger fraction of FM-coupling through the entire depth of the layer. This results in a smaller negative component of Γ_m as compared to the 1.4 nm Si sample.

The strong temperature-dependence is probably due to paramagnetic pinholes in the spacer. The pinholes short-circuit the magnetization, favouring ferromagnetic alignment when the temperature drops below the Curie temperature, T_C, of each pinhole. Of each iron percolation path T_C is determined by the number of adjacent ferromagnetic atoms. As this number is not constant, no discrete T_C for the whole sample exists, but rather a distribution of Curie temperatures where the coupling becomes more ferromagnetic during cooling.

The magnetic profiles presented in Figures 7.9 through 7.11 can be interpreted as the average Γ_m that the neutrons encounter in each iron layer. The antiferromagnetic Bragg peak is due to neutrons scattered at interfaces at at least two nuclear repetition lengths distance from each other. For example, in the case of the 1.4 nm Si on silicon sample the neutrons travel in the in-plane direction a distance of approximately 600 nm (2×3.58 nm/0.0124 rad) before encountering the next interface contributing to the antiferromagnetic Bragg peak. Therefore the regions of equal alignment have to be at least 600 nm large in the in-plane direction. The average Γ_m as experienced by the neutrons in such a region is not only determined by the "bulk" alignment in each Fe-layer, but also by the ferromagnetic regions around the pinholes.

The explanation of the presented Γ_m-profiles by a depth-dependent pinhole concentration is also in agreement with results obtained by other techniques than PNR. The MOKE-results (Figure 7.7) show more ferromagnetic behaviour at the substrate side of the Fe/Si multilayers because of the larger concentration of pinholes. The VSM-magnetization curves (Figure 7.12), with both ferromagnetic and antiferromagnetic characteristics, can be explained by the depth-dependent coupling mechanism. Also the increase of ferromagnetic coupling with the number of bilayers of Fe/Si multilayers produced under the same conditions [58] can be explained by the existence of pinholes. When the multilayer contains little bilayers, the influence of the pinholes is relatively large, so the magnetic behaviour will be mainly ferromagnetic. If the multilayer contains more bilayers, the surplus bilayers contain relatively less pinholes and the antiferromagnetic behaviour will be larger. The temperature dependence of the magnetic coupling as reported by den Broeder *et al.* [55] can be explained by the existence of pinholes. The at room temperature paramagnetic bridges will become ferromagnetic at cooling, enlarging the fraction of ferromagnetic alignment in the multilayers. This explains the increase of M_r/M_s with decreasing temperature as reported by [55].

7.6 Conclusions and Final Remarks

From the work described in this chapter the following conclusions can be drawn:

- The neutron scattering length density of the Fe/Si multilayers increases during sputtering.
- The PNR-data measured on Fe/Si multilayers at various magnetic fields can be described by the models presented in Figures 7.9 through Figure 7.11.
- The magnetization calculated from the models fitted to the PNR-data agrees well with the magnetization as measured by VSM. The agreement of the bilayer thickness as determined from the fitted model and small angle XRD-data is reasonable.
- The PNR-data measured at low magnetic fields can well be explained when the magnetic alignment is assumed to be predominantly ferromagnetic at the substrate side and predominantly antiferromagnetic at the topside of the samples. When the applied magnetic field increases, the fraction of ferromagnetic alignment will increase at the expense of the fraction of antiferromagnetic alignment.
- As the coupling mechanism and the coupling strength change throughout the whole depth of the Fe/Si multilayers, the overall hysteresis curve of a Fe/Si multilayer will be an average of all coupling mechanisms occurring in the multilayer. The presence of a biquadratic coupling mechanism is therefore not necessary to explain the hysteresis curves and their temperature-dependence.
- The depth-dependence of the magnetic coupling is ascribed to a depth-dependent concentration of pinholes, also responsible for the temperature-dependence of the coupling.
- The 1.1 nm Si on silicon sample has a larger amount of ferromagnetic coupling than the 1.4 nm Si on silicon sample. However, the antiferromagnetic coupling in the 1.1 nm Si on silicon sample is stronger than that in the 1.4 nm Si on silicon sample.
- Although biquadratic coupling is not needed to explain the magnetic properties measured on Fe/Si multilayers and no physical origin for biquadratic coupling is known, which could explain the large observed temperature-dependence of the interlayer coupling in Fe/Si multilayers, we can not exclude the existence of some biquadratic coupling. At the time the measurements were performed, ROG was not yet supplied with polarization analysis, so only R^+ and R^- could be measured. The presented data interpretation only takes into account the influence of magnetization components parallel or antiparallel to the polarization, while the measured reflectivity can also be influenced by magnetization components non-collinear with the polarization.

7.6. Conclusions and Final Remarks

Since the existence of biquadratic coupling in the Fe/Si multilayers can not be excluded from the described experiments, it is recommended to to perform PNR-experiments on such Fe/Si multilayers with polarization analysis, as is nowadays possible on ROG.

The spin parallel and spin antiparallel measurements performed at one magnetic field value should be performed with equally good counting statistics.

When new PNR-experiments on Fe/Si multilayers are performed, one should check by simulation whether a smaller number of bilayers also results in PNR-curves with clear characteristics. In the literature also differences are reported in the overall hysteresis curve between a multilayer of 2 and a multilayer of 6 bilayers [58]. So the depth-dependence of the coupling is already present in a multilayer containing only 6 bilayers. With fewer bilayers, the model contains fewer parameters to be fitted, which increases the confidence in the fitted model.

Chapter 8

NiFe/Cu/NiFe/FeMn; a spin-valve system

8.1 Interest in NiFe/Cu/NiFe/FeMn

In the system $Ni_{80}Fe_{20}/Cu/Ni_{80}Fe_{20}/Fe_{50}Mn_{50}$ (see Figure 8.1), one $Ni_{80}Fe_{20}$-layer is exchange-biased by the adjacent antiferromagnet $Fe_{50}Mn_{50}$, and the magnetization of the two $Ni_{80}Fe_{20}$-layers is coupled through the copper layer. The interplay between these two mechanisms determines the relative direction of the global magnetic moment in both $Ni_{80}Fe_{20}$-layers.

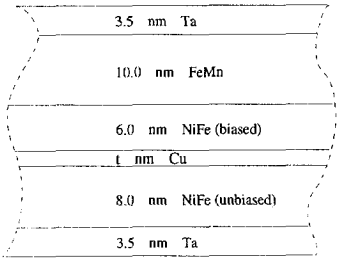

Figure 8.1: *Schematic representation of the spin-valve system considered.*

The mechanism of exchange-biasing was first observed by Meiklejohn and Bean [65] in 1956 in ferromagnetic Co-particles covered by a CoO layer, which is antiferromagnetic. Exchange-biasing is a phenomenon that can be observed when a ferromagnet and a highly anisotropic antiferromagnet are in close contact, so direct exchange between the two metals is possible. If the Curie temperature of the ferromagnet is higher than the Néel temperature, T_N, of the antiferromagnet, a unidirectional anisotropy—called exchange-biasing—can be induced by field

cooling the system from above T_N. The antiferromagnet will then order in a magnetic arrangement that minimizes the free energy of the total system at a parallel alignment of the ferromagnet with the applied field. The magnetic fields necessary to magnetize the system in the two opposite directions differ due to the exchange energy of the ferromagnet with the field cooled antiferromagnet. Therefore the adjacent antiferromagnet can cause a shift, also called bias, of the hysteresis curve of the ferromagnetic material along the H-axis. This shift only occurs when the energy for breaking the exchange at the ferromagnet/antiferromagnet interface is smaller than the anisotropy energy of the antiferromagnet. When the energy for breaking the exchange at the F/AF interface is larger than the anisotropy energy of the antiferromagnet, the anisotropy axis of the antiferromagnet will turn with the magnetization in the ferromagnet. As now also energy is needed to turn the anisotropy axis in the antiferromagnet, the hysteresis curve will be broader than the hysteresis curve of the free ferromagnet.

Another way to obtain exchange-biasing is to grow a system of a ferromagnet and an antiferromagnet in close contact in presence of a magnetic field. In the system considered in this chapter the antiferromagnetic $Fe_{50}Mn_{50}$-layer exchange-biases the adjacent $Fe_{80}Ni_{20}$(permalloy)-layer.

The coupling between the two permalloy layers of the considered system is the result of various mechanisms [66]. At small copper thicknesses the coupling through the copper layer is supposed to be caused by irregularities in the layered structure. 'Ferromagnetic bridges' in the copper layer caused by pinholes or by low-temperature diffusion of ferromagnetic material in grain-boundaries [67, 68] will give a large contribution favouring ferromagnetic alignment. Another mechanism favouring ferromagnetic alignment is Néel coupling. Néel coupling (also called 'orange-peel' coupling) is caused by correlated waviness of the ferromagnet/antiferromagnet interfaces [69]. In Figure 8.2 a schematic view of the principle of Néel coupling is given. When those two mechanisms are sufficiently weak, the oscillating RKKY-coupling might dominate the coupling between the two permalloy layers.

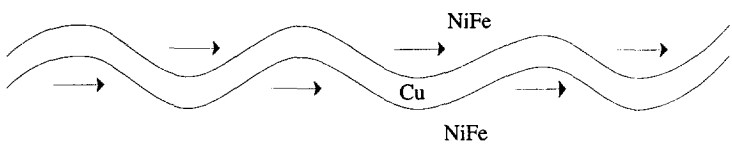

Figure 8.2: *Principle of Néel coupling. The magnetization tends to be directed parallel at the positions of the arrows by dipole coupling.*

The electrical resistance of a metal depends on the orientation of the electron spin with respect to the local magnetic moment. For example, in $Ni_{80}Fe_{20}$ the mean-free path of electrons with spin parallel to the local magnetic moment has been estimated to be at least five times larger than with spin antiparallel [70, 71].

This phenomenon is used to create multilayers that exhibit magnetoresistance. Such multilayers contain magnetic layers, that usually are aligned antiferromagnetically in remanence and can be aligned ferromagnetically by applying a magnetic field.

When in a multilayer the magnetization in neighbouring layers is oriented parallel to each other, the electrons with spin parallel to the local magnetic moment are weakly scattered, and therefore carry a large part of the current, while the spin antiparallel electrons are strongly scattered and contribute little to the conduction of the current. Assuming that the mean-free paths of the electrons are larger than the thicknesses of the various layers, the resistivity of such ferromagnetically aligned multilayers can be estimated to be:

$$\rho_{ferromagnetic} \approx \frac{\rho_p \rho_{ap}}{\rho_p + \rho_{ap}} , \tag{8.1}$$

with ρ_p the resistivity in the case of parallel alignment of spin and local magnetic moment, and ρ_{ap} the resistivity in the case of antiparallel alignment. Note that Eqn. (8.1) corresponds to parallel connection of the resistivity experienced by the electrons with spin "up" and spin "down", see Figure 8.3.

When the magnetization in a multilayer is aligned antiferromagnetically, the resistivity of this multilayer also corresponds with parallel alignment of the resistivity experienced by the electrons with spin "up" and spin "down". In this case however electrons with both spin states are alternately scattered strongly and weakly. Therefore the resistivity experienced by both electrons with spin "up" and spin "down" is equal to the average of ρ_p and ρ_{ap}. The resistivity of an antiferromagnetically aligned multilayer is therefore given by:

$$\rho_{antiferromagnetic} \approx \frac{\rho_p + \rho_{ap}}{4} , \tag{8.2}$$

again corresponding to connection in parallel of the resistivity experienced by electrons with both spin state (see also Figure 8.3).

The term 'spin-valve magnetoresistance' was introduced for the change in resistivity associated with changes in the magnetic alignment of the magnetic moment in the successive ferromagnetic layers [72]. Therefore this system is called a spin-valve system. The term giant magnetoresistance (GMR) is also used for the above described effect in the literature. However, this term suggests very large changes of the resistance, whereas also small changes of the resistance occur due to this effect.

Experiments by Rijks et al. [73] on similar $Ni_{80}Fe_{20}/Cu/Ni_{80}Fe_{20}/Fe_{50}Mn_{50}$ systems, produced under exactly the same conditions as in this work, show the magnetoresistance effect. These magnetoresistance curves are shown in Figure 8.4 for Cu thicknesses ranging from 0.9 to 9.3 nm. This figure shows that the magnitude of the magnetoresistance depends strongly on the Cu-thickness. When this system is applied in a magnetoresistive read head the copper thickness is about 2.0 nm. In spin-valve systems of this composition the magnetoresistance effect at room temperature can be as high as 4.3 % in a magnetic field of only 10 kA/m [73].

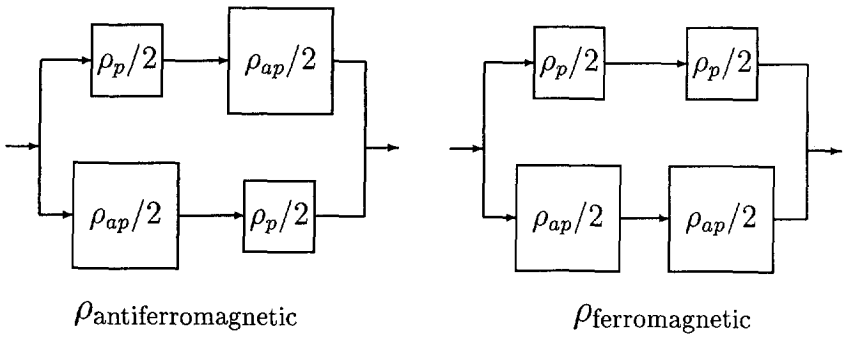

Figure 8.3: *Schematic representation of resistivity in case of ferromagnetic and antiferromagnetic alignment of magnetization in separate layers of a multilayer.*

Systems are known that exhibit a much larger spin-valve magnetoresistance effect. For example, Fe/Cr-multilayers exhibit magnetoresistances of 150 % at 4.2 K in a field of 1600 kA/m. The fact that the system considered here exhibits a significant change in magnetoresistance at room temperature in low magnetic fields makes this system very useful for applications, e.g. as a magnetoresistive read-back head. This kind of spin-valve system is already used in prototypes of magnetoresistive read-back heads.

The GMR-effect is supposed to be caused by the transition from parallel to antiparallel alignment of the magnetization in the NiFe-layers on both sides of a Cu-layer. By performing PNR on spin-valve systems one can study this transition. PNR-experiments were performed on spin-valve systems with Cu thicknesses below 2 nm, where the competition between exchange-biasing and interlayer coupling is large. The transition from parallel to antiparallel alignment can also be studied by magnetization measurements. By PNR however, the magnetization as a function of depth and therefore also the magnetization in the biased and unbiased permalloy layers separately can be determined.

Although PNR in general can provide information about the direction of the magnetization in thin layers by polarization analysis, we confined ourselves to the study of the magnetization component parallel to the polarization direction. This was done because at the time the experiments were performed ROG was not yet supplied with polarization analysis.

8.2 Description of the Experiments

Two samples, containing 5 repetition periods, grown on Si(100) have been studied: $5\times$[Ta(3.5)/$Ni_{80}Fe_{20}$(8)/Cu(t)/$Ni_{80}Fe_{20}$(6)/ $Fe_{50}Mn_{50}$(10)/Ta(3.5)], where the figures in brackets refer to the thickness of each layer in nm, and the thickness of the copper layer, t, is 1.0 or 1.5 nm. In Figure 8.1 the samples are given schematically.

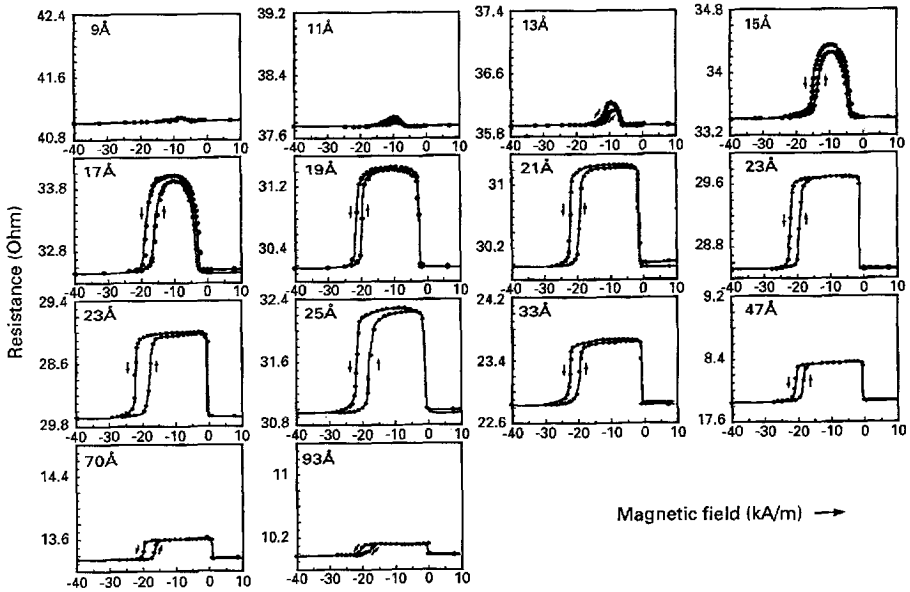

Figure 8.4: *Electrical resistance vs applied magnetic field for the system Si(100)/Ta(3.5)/$Ni_{80}Fe_{20}$(8)/Cu(t)/$Ni_{80}Fe_{20}$(6)/$Fe_{50}Mn_{50}$(10nm)/Ta(2) with the copper layer thickness given in the corner of each graph as reported by Rijks [73], showing the spin-valve magnetoresistance effect.*

The tantalum layers were put between the spin-valve structures to prohibit the antiferromagnet to interact with the permalloy layer other than its adjacent one. The tantalum layer at the surface is used to prevent oxidation and contamination, the layer at the substrate to minimize interdiffusion between the silicon substrate and the spin-valve structure.

The samples were dc magnetron sputtered, after cleaning the silicon substrate by a 2 % HF dip. During deposition in an Ar atmosphere of 0.7 Pa, an external in-plane magnetic field of 11 kA/m was applied. The sputter rate used was 0.2 nm/s. Due to the sputter process the temperature of the substrate might rise a few tens of degrees above room temperature. These sputter conditions were chosen exactly the same as used by Rijks for his samples, of which the magnetoresistance curves are given in Figure 8.4. The roughness at the interfaces was determined to vary between 0.3 and 0.5 nm by atomic force microscopy.

Of both samples the polarized neutron reflectivity was measured on ROG, the time-of-flight reflectometer of IRI, at an angle of incidence of 10 mrad. During the experiments a magnetic field was applied parallel to the axis favoured by the field applied during sample growth. In the following the applied field will be called positive when it cooperates with the exchange-biasing mechanism to favour alignment of the magnetization in the same direction. It will be called negative

when it favours opposite alignment of the magnetization. PNR-data of the 1.0 nm Cu sample were obtained in magnetic fields of +12.0, +19.2, -8.8, -12.0 and -13.6 kA/m, each obtained by decreasing the field from positive saturation. PNR-data of the 1.5 nm Cu sample were obtained in fields of -1.6, -8.8, -11.2, -13.6, -15.2 and -56.0 kA/m, each obtained by "increasing" the field from the negative saturated state.

8.3 Interpretation of PNR-data

The measured reflectivity curves of the 1.0 nm sample are given in Figure 8.5. The presented data show that when the applied magnetic field becomes more negative, the spin antiparallel reflectivity increases compared to the spin parallel reflectivity. At -12.0 kA/m the intensities of the spin parallel and spin antiparallel data are almost equally large. At -13.6 kA/m the spin antiparallel data have a larger value than the spin parallel data.

Figure 8.6 shows the neutron reflectivity curves of the sample with a copper layer of 1.5 nm. Again the spin antiparallel reflectivity increases compared to the spin parallel reflectivity when the applied field becomes more negative.

The peaks in the neutron reflectivity curves of the 1.0 nm Cu sample are situated at a slightly larger distance from each other than those of the 1.5 nm Cu sample. This is caused by the smaller repetition period of the 1.0 nm Cu sample. The neutron reflectivity data for each sample are fitted simultaneously keeping the depth profile of Γ_n the same for the different magnetic states. The models kept Γ_n and the thickness of the copper layer constant, because this layer is too thin to be fitted. The value of Γ_n was supposed to be equal for all permalloy layers. Except for the upper and lower Ta-layer the repetition is supposed to be perfect.

At first instance the PNR-data were fitted allowing only magnetic scattering in the permalloy layers [74]. The obtained model clearly shows that the magnetization behaves much more independently in the 1.5 nm Cu sample than in the 1.0 nm Cu sample. However, as the mechanism of exchange-biasing is not yet well understood, various other possibilities for the magnetization profile at the interface between the antiferromagnet and the ferromagnet were explored:

1. The biased layer is divided into two layers with Γ_n equal to each other, but Γ_m and the thicknesses of these two layers vary both independently. No magnetization is allowed in the antiferromagnetic layer.

2. The antiferromagnetic layer is divided into two layers with Γ_n equal to each other but the thicknesses of these two layers vary independently. The antiferromagnetic layer adjacent to the biased permalloy layer is allowed to exhibit magnetization. The value of Γ_m of the biased layer is constant over the whole depth of this layer.

3. Both the biased permalloy layer and the antiferromagnetic layer are divided into two layers, with Γ_n equal to each other. All thicknesses fit separately.

The value of the magnetization in both biased permalloy layers is allowed to differ from each other. Only the antiferromagnetic layer adjacent to the permalloy is allowed to exhibit magnetization.

The different assumptions did not change the value of χ^2 considerably. However, when the modelled antiferromagnet is allowed to exhibit some magnetic scattering length density at the interface, the value of the integral magnetization corresponds much better with the VSM-measurements. When no magnetization is allowed in the antiferromagnet the integrated magnetization at saturation from the fitted PNR-model is 20 (13) percent too large for the 1.0 (1.5) nm Cu sample. Allowing some magnetization at the permalloy side of the antiferromagnet gives good correspondence between PNR and VSM at saturation. Dividing the biased permalloy layer in magnetically different layers did not improve the fit to the data or the correspondence with the VSM-measurements significantly. Therefore the physical reality is supposed to be modelled best in the second mentioned possibility, allowing some magnetization in the antiferromagnet. The best models, fitted according to this possibility are presented in Figure 8.7. The magnetic contribution present in the antiferromagnet did not change the trend in the magnetization in the permalloy layers [74]. For the 1.0 and 1.5 nm Cu samples values for χ^2 of 3.49 and 2.94 were obtained respectively.

In the upper part of Figure 8.7 the fitted nuclear model is given by a solid line. For comparison the dashed line represents the profile expected as calculated from sputter velocity and bulk densities. Also for comparison the values of Γ_n as expected and as obtained by fitting are given in Table 8.1. The figures in brackets behind the fitted values give the standard deviation s as a result of the counting statistics. The values of Γ_n from PNR can differ from the expected ones considering that in calibrating the sputter velocity errors of 5 % can occur for each sputter target and that the density of the layers can differ from the bulk density as a consequence of strain or interdiffusion between the layers. The differences in the fitted values of Γ_n for FeMn and Ta for the two samples are rather large.

For both samples the values of the thickness and Γ_n of the Ta-layer at the surface as obtained by fitting are much larger than Γ_n of bulk Ta. By oxidation Ta_2O_5 will be formed, with a bulk value of Γ_n of 6.1×10^{-3} nm^{-2}. By absorbing oxygen also the volume and therefore the thickness of the top Ta-layer will increase. However, the fits to the 1.0 and 1.5 nm PNR- data result in the higher values of 0.008 and 0.007 nm^{-2}. These differences might be caused by contamination of the surface.

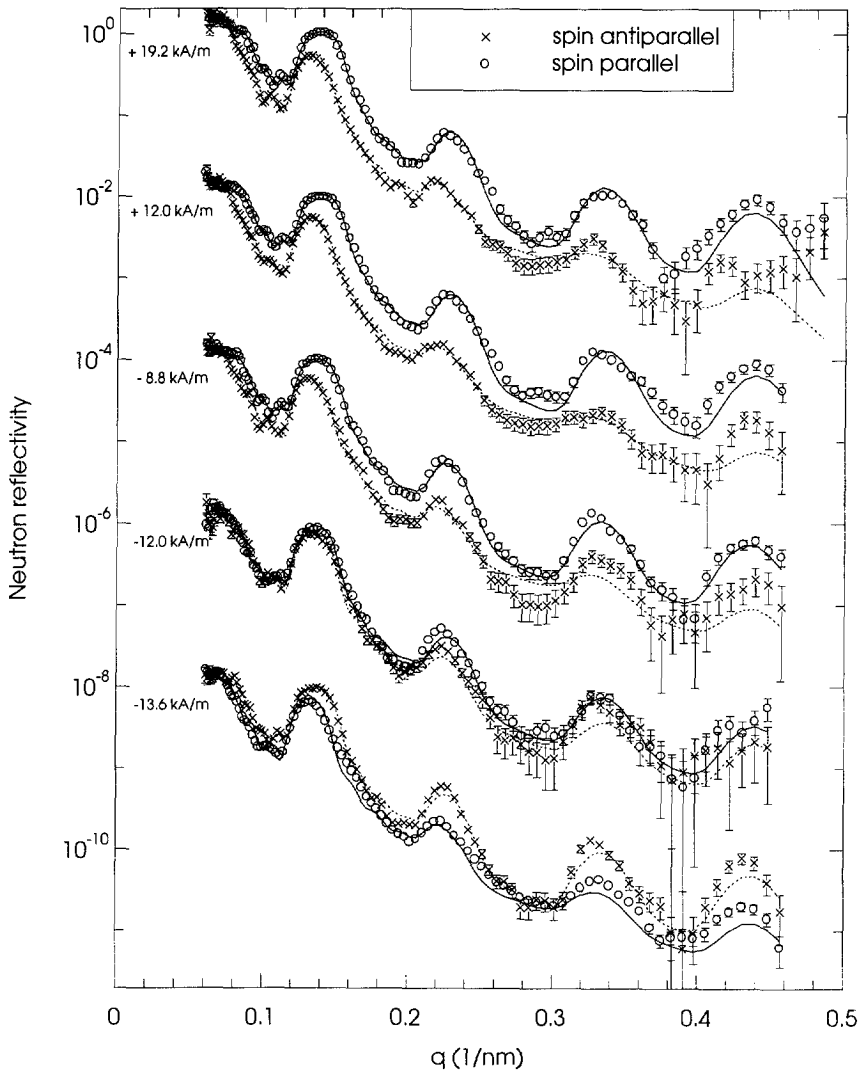

Figure 8.5: *Neutron reflectivity data (symbols) of the sample with a Cu-layer thickness of 1.0 nm at various in-plane magnetic fields. The lines represent the simulated spin parallel (solid) and spin antiparallel (dashed) reflectivity. Data measured at different field values are offset for clarity.*

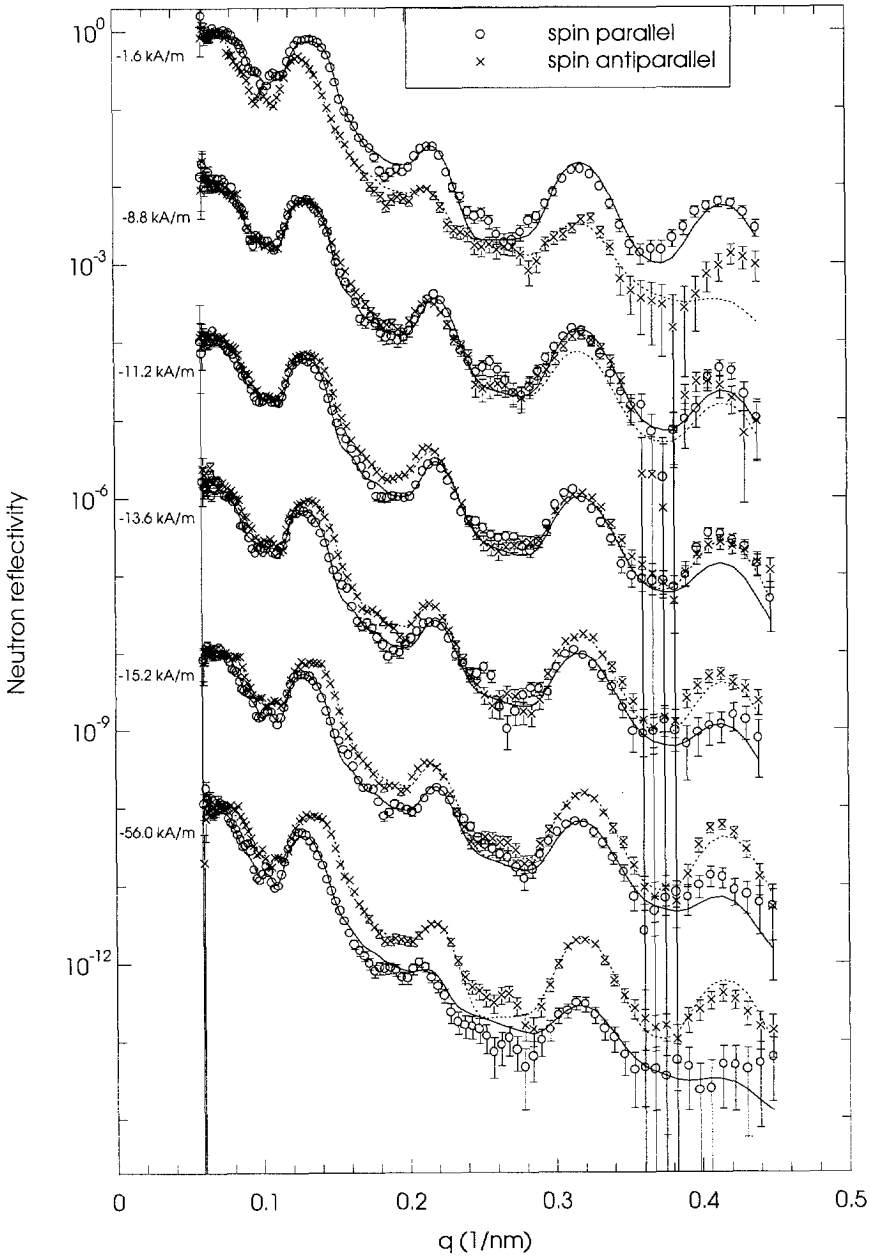

Figure 8.6: *Neutron reflectivity data (symbols) of the sample with a Cu-layer thickness of 1.5 nm at various in-plane magnetic fields. The lines represent the simulated spin parallel (solid) and spin antiparallel (dashed) reflectivity. Data measured at different field values are offset for clarity.*

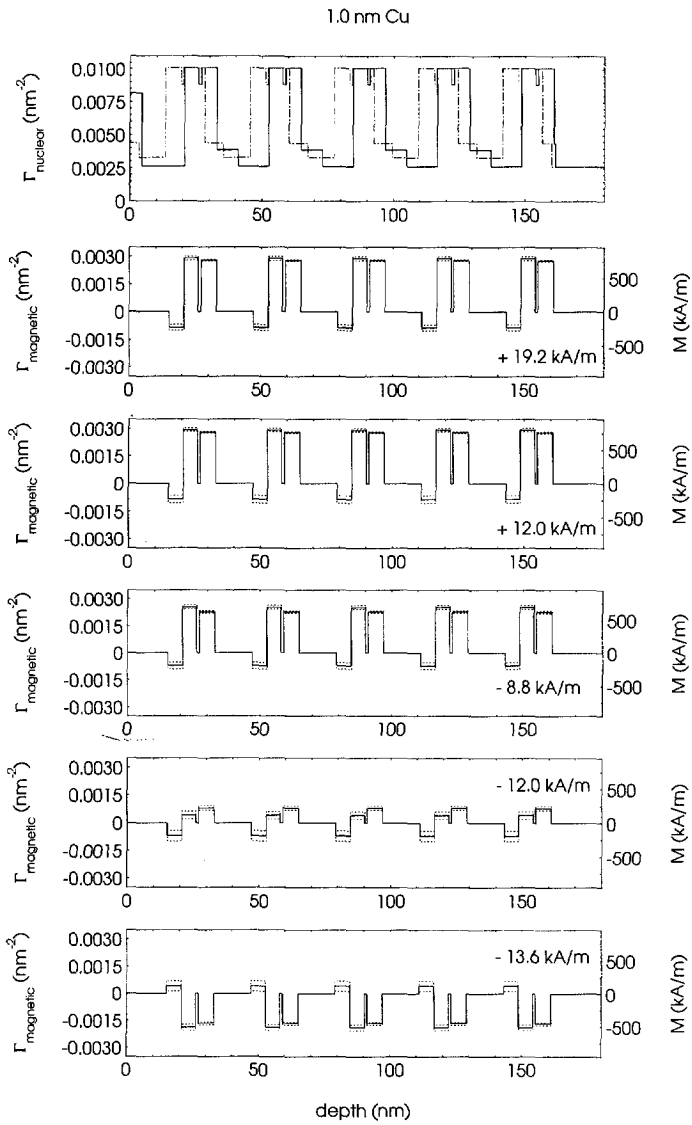

Figure 8.7: *Depth profiles of Γ_n and Γ_m as fitted to PNR-data of the 1.0 nm Cu sample. The dotted lines in the Γ_n graph represent the expected nuclear profile derived from sputtering time and bulk densities. The dotted lines in the Γ_m-graphs represent the fitted value of Γ_m plus and minus one standard deviation. On the right-hand axis of the Γ_m-graph the corresponding magnetization values are given in kA/m.*

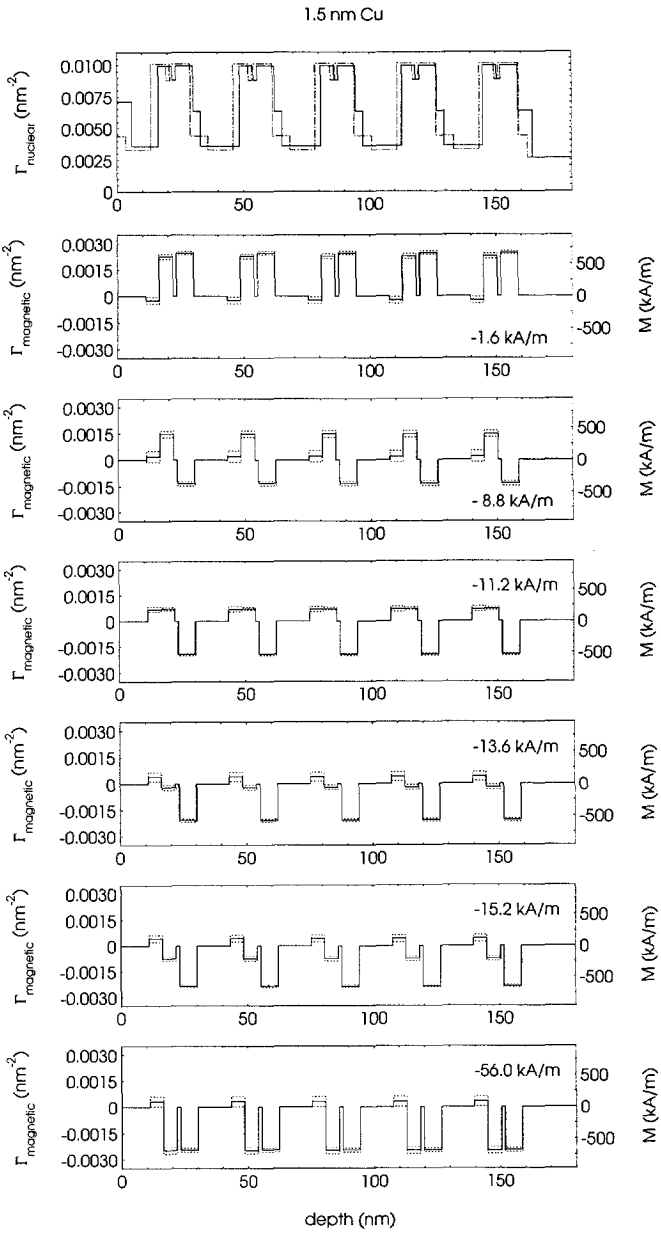

Figure 8.8: *Depth profiles of Γ_n and Γ_m as fitted to PNR-data of the 1.5 nm Cu sample. The dotted lines in the Γ_n graph represent the expected nuclear profile derived from sputtering time and bulk densities. The dotted lines in the Γ_m-graphs represent the fitted value of Γ_m plus and minus one standard deviation. On the right-hand axis of the Γ_m-graph the corresponding magnetization values are given in kA/m.*

Table 8.1: Comparison of Γ_n as calculated from bulk densities with Γ_n obtained by fitting to the PNR-data of the 1.0 and 1.5 nm Cu samples.

layer	Γ_n calc. from bulk density (nm^{-2})		fitted Γ_n 1.0 nm Cu (nm^{-2})	fitted Γ_n 1.5 nm Cu (nm^{-2})
Ta	0.0044	surface middle part bottom	0.0081(1) 0.00388(3) 0.0044 constant	0.0071(1) 0.0063(1) 0.0063(1)
$Ni_{80}Fe_{20}$	0.0101		0.01010(2)	0.00993(2)
Cu	0.0088		0.0088 constant	0.0088 constant
$Fe_{50}Mn_{50}$	0.0033		0.00262(3)	0.00357(3)
Si	0.0027	substrate	0.0026 constant	0.0026 constant

The value of the relative standard deviation for the thicknesses of the separate layers is smaller than 2 %. From Figures 8.7 and 8.8 it is clear that the total thickness in both samples agrees very well with the expected value.

Fitting the model, roughness is allowed at the interfaces. For the roughness at the different interfaces values between 0 and 8 nm were obtained for the 1.0 nm Cu sample and between 0 and 10 nm for the 1.5 nm sample. These fitted roughness parameters model a gradual change in Γ as described in section 4.1. Such a gradual change can be caused by interdiffusion between the sputtered layers. The fits to both samples yield a $\Delta q/q$-resolution of 8 %.

Considering the inaccuracies of the model (the negligence of the magnetization components perpendicular to the polarization of the neutrons, and the assumption that the repetitions are perfect), the agreement between the expected nuclear profiles and the obtained nuclear profiles is good.

Figure 8.7 also gives the magnetization depth profiles at the various magnetic fields. The dashed lines represent the fitted Γ_m-value plus and minus one standard deviation, based on counting statistics, assuming the model represents the reality. The value of Γ_m of bulk $Ni_{80}Fe_{20}$ is calculated to be equal to 3×10^{-3} nm^{-2}. The fitted value of Γ_m of the biased NiFe layer at + 19.2 and + 12.0 kA/m corresponds to this value. The magnetization in the unbiased layer of this sample is only 2.8(5) $\times 10^{-3}$ nm^{-2}. However, from VSM measurements it is clear that the sample is saturated at these field values. The fitted values for Γ_m of $Ni_{80}Fe_{20}$ of the 1.5 nm Cu sample are even lower at the saturated fields (-1.6 and -56.0 kA/m), as can be seen in Figure 8.7. These differences between bulk and fitted values can be caused by interdiffusion and stress. The value of Γ_m also depends strongly on the composition of the permalloy. Small changes in the composition might result in large changes of the value of Γ_m.

8.4 Correspondence with VSM

In Figure 8.9 the magnetization as a function of applied field as measured by VSM is given for the 1.0 and 1.5 nm Cu samples. The magnetization is calculated from the product of the magnetization and the magnetic volume as determined by VSM, using the thicknesses as obtained from fitting to the PNR-data.

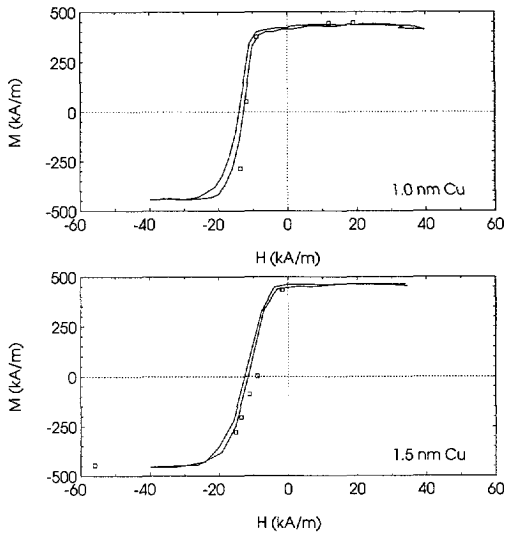

Figure 8.9: *Comparison between the magnetization as determined by VSM (lines) and by PNR (squares) for both samples.*

When comparing the magnetization as calculated from PNR with the VSM-curve, one has to realize that for the 1.5 nm sample each magnetic state was preceded by negative saturation, while for the 1.0 nm sample each magnetic state was preceded by positive saturation. This means that the data from PNR should be compared with different branches of the magnetization curves. The results from PNR for the 1.0 nm Cu sample agree well except for the field value of -13.6 kA/m. For the 1.5 nm Cu sample only the results at field values of -8.8 and -11.2 kA/m do not agree well with the VSM measurements. Considering the assumptions made, the agreement between the magnetization from PNR and from VSM is reasonable.

8.5 Discussion

The magnetic depth profiles in Figures 8.7 and 8.8 show that the magnetization in the permalloy layers of the 1.5 nm Cu sample rotates much more independently than that of the 1.0 nm Cu sample. The Γ_m-profiles for the 1.0 nm Cu sample show an almost simultaneous switch in the two NiFe-layers. In contrast, in the case of the 1.5 nm Cu sample a magnetic field region of at least 2.5 kA/m, in which the determined components of magnetization are antiparallel, is observed.

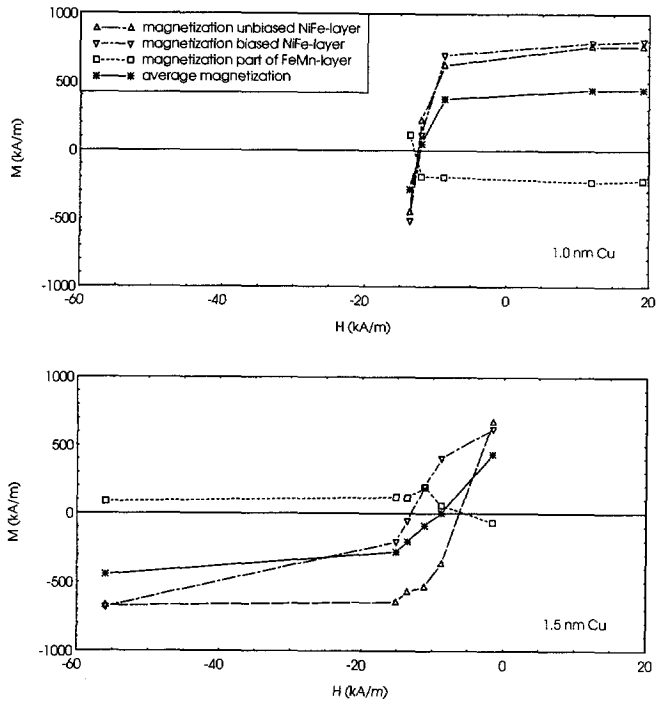

Figure 8.10: *Magnetization as a function of magnetic field of the biased and unbiased permalloy layers in both samples. The solid lines give the magnetization of the whole sample.*

These observations are in agreement with the measured magnetoresistance curves presented in Figure 8.4. As discussed in the introduction the magnetoresistance will be higher when the magnetization in the two permalloy layers rotates more independently. In the case of the 1.0 nm Cu sample the magnetization in both permalloy layers rotates almost simultaneously. This is in agreement with Figure 8.4 as the samples with a copper layer of 0.9 and 1.1 nm Cu show almost no change in resistance with applied magnetic field. In the 1.5 nm Cu sample, where the magnetization of the two permalloy layers rotates more independently, a magnetoresistance of 3 % is observed.

For the magnetic fields of -12.0 and -13.6 kA/m the profile fitted to the data measured on the 1.0 nm Cu sample is different from that expected. It is expected that the change in magnetization compared to the positive saturated state will be smaller in the biased layer than in the unbiased layer because of the exchange-biasing. However, the magnetization in the biased layer has changed more compared to positive saturation than in the unbiased layer. This might be caused by the assumptions made interpreting PNR-data measured without polarization

analysis using the matrix method. The influence of an in-plane component of magnetization perpendicular to the polarization direction is neglected in the data interpretation. This magnetization component will be considerable for the 1.0 nm Cu sample at magnetic field values of -12.0 and -13.6 kA/m. Apparently the influence of this perpendicular magnetization component in the permalloy layers is too large to determine the almost equally large magnetization components parallel to the polarization direction, separated by only 1.0 nm Cu, accurately.

In Figure 8.10 the magnetization versus field of the biased and unbiased layers is given for both samples. Also the magnetization of the magnetic part of the antiferromagnetic layers is given. One can see that for the 1.0 nm Cu sample the differences in the magnetization in the two permalloy layers during the magnetization rotation are much smaller than for the 1.5 nm Cu sample.

At most magnetic fields the net magnetization in the antiferromagnet is aligned antiparallel to the magnetization in the biased permalloy layer, (see Figures 8.7 and 8.8). In Figure 8.11a the fitted values of those two parameters are plotted versus each other. The two points (first quadrant in Figure 8.11a) for which the net magnetization in the direction of the polarization in the antiferromagnet is not anti-parallel to the magnetization in the biased layer are measured at the field values for which the VSM and PNR results do not agree very well (-8.8 and -11.2 kA/m, 1.5 nm Cu sample). At these field values the in-plane magnetization component perpendicular to the polarization direction is relatively large. As the influence of this component is neglected, the fitted values for Γ_m at these field values probably differ more from reality than at other fields. However, from Figures 8.7, 8.8 and Figure 8.11a it is clear that at saturation the magnetization in the magnetic part of the antiferromagnet and the biased permalloy layer is aligned antiferromagnetically.

In Figure 8.11b the magnetization in the antiferromagnet versus the magnetization in the unbiased NiFe-layer is presented. Surprisingly these two parameters have consistently the opposite sign (empty first and third quadrant).

As mentioned before, the best agreement between PNR and VSM is obtained when a part of the antiferromagnet is modelled to exhibit a magnetic contribution at the biasing interface. This indicates that at the biasing interface the antiferromagnet behaves in another way than in bulk FeMn, where Γ_m is equal to zero. The fitted thicknesses of these magnetic FeMn-layers are 5.5 and 5.3 nm for the 1.0 and 1.5 nm Cu sample, respectively. The fitted roughness between the non-magnetic and magnetic FeMn-layer is about 5 nm, with a value of s between 0.7 and 14 nm for the 1.0 and 1.5 nm Cu sample. Roughness at this interface implies only a variation in the magnetic contribution as Γ_n is equal for the magnetic and the non-magnetic part of the FeMn-layer. The fact that the fitted roughness has approximately the same value as the fitted thickness of the magnetic part of the FeMn-layer, can be interpreted as a gradual decrease of the magnetic component from the biasing interface. However, as s of the fitted roughness at this interface is large, care has to be taken in drawing conclusions.

From the literature follows that the macroscopic magnetic behaviour of spin-valve systems can be well described by models in which the ferromagnetic layers

are considered as one domain [75, 73, 76, 77], and the magnetization reversal takes place by rotation only. Nishioka [75] reported that the magnetization in the free layer rotates without domain formation.

Traditionally the magnetization in the antiferromagnet is supposed to be equal to zero. Assuming that the antiferromagnet exhibits no net magnetization and that the magnetization reversal takes place only by rotation, the total magnetic energy of a spin-valve system is given by the following equation [73]:

$$E_{tot} = -\mu_0 M_1 t_1 H \cos(\beta_1) - \mu_0 M_2 t_2 H \cos(\beta_2) - E_{EB} \cos(\beta_2) - J \cos(\beta_1 - \beta_2). \tag{8.3}$$

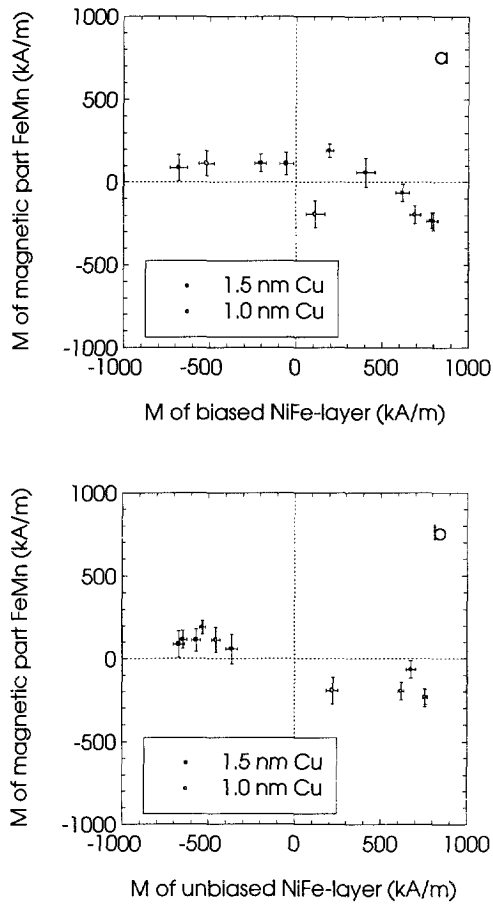

Figure 8.11: *Magnetization in the magnetic part of the FeMn-layer versus the magnetization in the biased permalloy layer (figure a) and versus the magnetization in the unbiased permalloy layer (figure b). The error-bars indicate one standard deviation.*

The first two terms of the total magnetic energy represent the Zeeman-energy of the two magnetic layers with magnetization M, thickness t, and with β_i the angle between the applied field and the magnetization in the two layers, as shown in Figure 8.12. The third term corresponds to the exchange energy E_{EB} at the interface between the ferromagnetic and antiferromagnetic layers, and the fourth term to the exchange coupling between both $Ni_{80}Fe_{20}$-layers. When the antiferro-

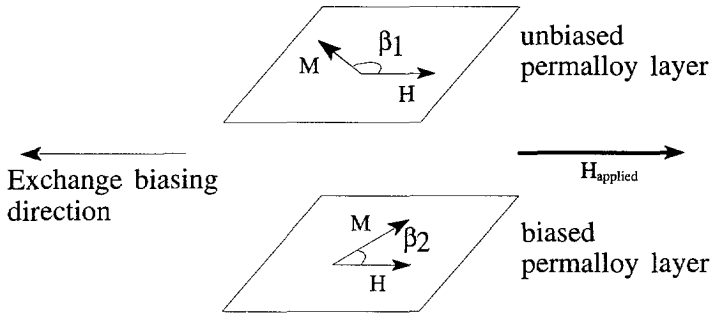

Figure 8.12: *Definition of the angles β_1 and β_2. These angles are defined as the angles between the average magnetization in both layers and the applied negative magnetic field.*

magnet also exhibits magnetization, this will lead to an additional Zeeman-term in Eqn. (8.3). However, as traditionally the magnetization in the antiferromagnet is supposed to be zero, the Zeeman-energy corresponding to magnetization in the antiferromagnet is probably accounted for in the value of E_{EB}. By comparing the values of the magnetization in the permalloy layers found by fitting the model without any magnetization in the antiferromagnet (published in [74]) and the model presented here, one sees that the trend is the same. Therefore in the following comparison the Zeeman-energy of the antiferromagnet is neglected.

The direction of the magnetization of both ferromagnetic layers can be obtained by minimizing the total energy as given in Eqn. (8.3) with respect to β_1 and β_2 for a given value of H. This was done by Rijks et al. [73]. They conclude that in the system [$Ni_{80}Fe_{20}$(8nm)/Cu(t)/$Ni_{80}Fe_{20}$(6nm)/ $Fe_{50}Mn_{50}$(8nm)] no perfect antiparallel alignment of the magnetic moments in the two NiFe-layers can be realized for a thickness of the copper layer less than 1.5 nm. Therefore the magnetoresistance decreases rapidly when the Cu-layer becomes less than 1.5 nm, as shown in Figure 8.4.

To calculate the orientation of the magnetization in the permalloy layers of the samples considered in this study, the values of the two parameters: J and E_{EB} have to be known. For E_{EB} the value 0.13 mJ/m^2 is taken, as determined by Rijks [73] for spin-valve systems sputtered under the same circumstances, however the antiferromagnetic layer of his samples is smaller (8 nm instead of 10 nm). It is assumed that this difference does not influence the value of E_{EB} considerably.

The value of J is extrapolated from results of Rijks to be equal to 0.17 and 0.04 mJ/m^2 for the 1.0 and 1.5 nm Cu samples respectively.

The calculated orientation of the magnetization in the permalloy layers for both samples is given in Figure 8.13 by dashed lines. The symbols in Figure 8.13 represent β calculated from the fitted Γ_m-profiles, assuming the norm of the magnetization does not change during rotation.

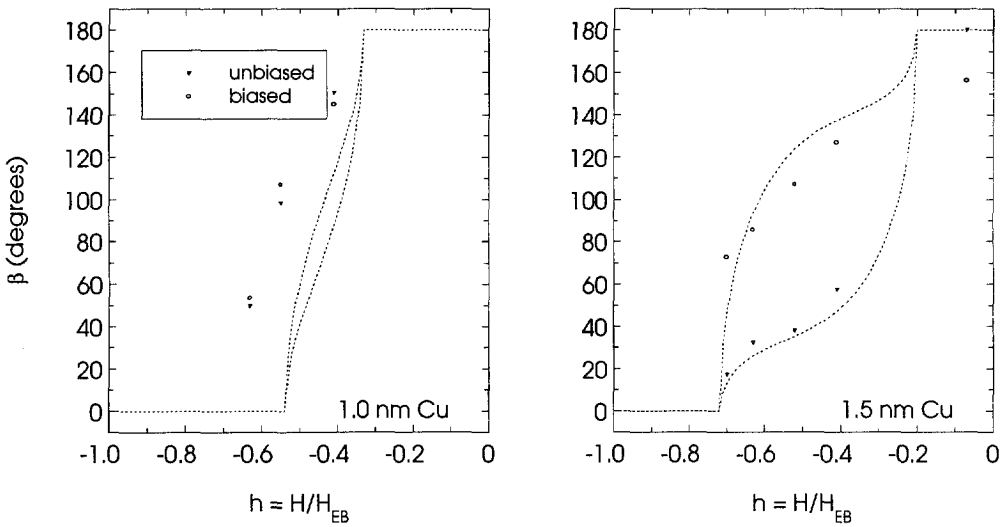

Figure 8.13: *Optimal values for β deduced from energy minimalization are given by the dashed curves. The points represent β calculated from the models fitted to the PNR-data.*

For the 1.5 nm Cu sample the orientation of the magnetization in the permalloy layers agrees well with the calculation, considering the assumptions made. For the 1.0 nm sample a shift to larger values of $h = H/H_{EB}$ seems to have taken place. A possible explanation for this shift is an error in the estimate of E_{EB} and J.

8.6 Conclusions and Final Remarks

From the performed PNR-experiments on the spin-valve systems the following conclusions can be drawn:

- The magnetization in the two permalloy layers of the 1.5 nm Cu sample rotates much more independently than in the 1.0 nm Cu sample.
- The magnetization as calculated from the models fitted to the PNR-data and determined by VSM-measurements is reasonable.
- The magnetization for both samples from PNR shows the same tendency as when calculated from energy minimalization, assuming the reversal in both

permalloy layers takes only place by rotation.

- The model fitted to the PNR data indicates that at the exchange-biasing interface the antiferromagnet is ordered such that it contains an in-plane magnetic contribution over a length of about 5 nm. At saturation the magnetization in this magnetic part of the antiferromagnet is aligned anti-parallel to the magnetization in the biased NiFe-layer.

- Variation in the magnetic contribution within the biased NiFe-layer does not improve the fit to the data, indicating that Γ_m of the biased NiFe-layer is constant.

The interface between antiferromagnet and ferromagnet can be studied in more detail in a multilayer of Ta/FeMn/NiFe. The samples studied in this work are more complicated and therefore it is more difficult to extract information on exchange-biasing from these samples.

When PNR-experiments with polarization analysis would be performed on spin-valve systems as described in this chapter, the influence of the in-plane magnetization component perpendicular to the polarization direction can be taken into account. Then a model can be fitted to the data that resembles the physical reality more, resulting in better quality of the fit and the fitting parameters can be determined more accurately.

Chapter 9

Conclusions and Final Remarks

The experiments described in this thesis show that polarized neutron reflectometry can give vital information on depth profiles of the magnetization that can not be obtained by other techniques. For example the conclusion that the upper layer of the two-layer tape exhibits a larger product of spontaneous magnetization and thickness can not be obtained by another technique. Also the gradual change of the perpendicular anisotropy in the Co-Cr layer can not be determined by other techniques

Recently ROG was supplied with polarization analysis, which makes it possible to determine also the in-plane component of the magnetization perpendicular to the polarization direction of the beam. Interpreting the PNR-data measured on the spin-valve systems described in chapter 8, only the magnetic component parallel to the polarization direction could be determined, neglecting the influence of the component perpendicular to the polarization on the reflectivity profile. To compare the results with energy minimalization calculations, the norm of the magnetization is assumed to be the same for the different magnetic field values, so magnetization reversal should take place by rotation only. By performing PNR-experiments with polarization analysis on such samples, one can check whether or not the norm of the magnetization is indeed the same. Also it is expected that a better model fit to the data can be obtained when also the influence of the in-plane magnetization component perpendicular to the beam polarization is taken into account.

It is also recommended to perform PNR-experiments with polarization analysis on Fe/Si multilayers as described in chapter 7. Such experiments can give an definitive answer on the presence of biquadratic coupling in Fe/Si multilayers, as discussed in literature.

PNR-data are difficult to interpret because of the loss of phase information, resulting in non-uniqueness of the fitted model. To gain confidence in fitted models comparison with other techniques should always take place. Therefore, as much

information as possible should be obtained by other techniques like X-ray reflection, X-ray diffraction, Auger analysis, electron microscopy, VSM, magneto-optical Kerr effect measurements etc.

Models with different boundary conditions could be fitted to the PNR-data measured on the one-layer tape, that showed hardly any distinct characteristics. In this case VSM was needed to choose the best model.

From chapter 7 and 8 it is clear that the correspondence with VSM can give additional information. In chapter 7 on the Fe/Si multilayers the initial disagreement between results from PNR and VSM led to a more complicated model of the sample, with Γ_n decreasing from the surface towards the substrate. In chapter 8 on the spin-valve system, comparison between PNR- and VSM-results indicated a magnetic moment in part of the antiferromagnetic layer. Therefore, one should always compare the magnetization as fitted to PNR-data with the magnetization as measured by VSM.

When comparing those two quantities one should also be aware that the VSM signal is sensitive to the product of magnetic volume and magnetization. To calculate the value of the magnetization from the VSM-signal, the thickness of the layer is needed. Because the thickness as estimated from sputter calibration might be less accurate than the thickness from PNR, the latter can better be used for this calculation. This is the case for the Co-Cr sample, as described in chapter 4. Also because of the non-uniqueness of the fitted model comparison of the fitted magnetization with the magnetization determined by VSM is a highly recommended check.

To be able to measure the magnetization at the time the PNR-experiment takes place at IRI, it is highly recommended to have a VSM set-up available at IRI. Disagreement in the magnetic behaviour as a result of oxidation, training or relaxation can then be excluded.

Another method to enhance the confidence in the fitted models, is to design the samples in such way that as little parameters as possible have to be fitted. For example in the literature changes are observed of the bulk magnetization curve of Fe/Si multilayers containing 2 and 6 bilayers [58]. When experiments on Fe/Si multilayers are repeated it should be checked by simulation whether or not different magnetic alignments in Fe/Si multilayers containing less bilayers result in sufficient characteristic PNR-curves.

It is also recommended to study the exchange-biasing interface of the spin-valve system described in chapter 8 in a less complicated sample. The results of chapter 8 indicate that the antiferromagnet layer at this interface, contains a net magnetic moment in a layer of about 5 nm at the interface with the permalloy layer. To research the exchange-biasing interface, a NiFe/FeMn/spacer multilayer is sufficient. In such a sample the number parameters to be fitted is considerably less than in the spin-valve system described in chapter 8. Whenever it is possible to design the samples to be used for PNR-experiments, one should perform model calculations to optimize for example the number of repetitions, or the thicknesses of layers.

All experiments described in this thesis are interpreted using the so-called

matrix method. In this method one approximates the variation of the neutron scattering length density by slabs with constant neutron scattering length density. All experiments could be described using this method.

However, to reduce the amount of fitting parameters it is strongly recommended to write a shell around the parameter fitting routine, in which analytical dependences of the neutron scattering length density on depth can be approximated by discrete steps in the neutron scattering length density. The matrix method can then be applied to these discrete steps.

Using the matrix method on videotapes and the Co-Cr layer, with only small or gradual changes in Γ_n and Γ_m, it appeared that the data could best be fitted, assuming the sample to contain more layers with equal thickness, with the thickness itself a parameter to be fitted. Otherwise an interchange of the values obtained for the thickness and Γ might occur.

Overcorrecting the experimental data measured on the Co-Cr layer for the polarization of the neutron beam, resulted in a negative spin antiparallel reflectivity. This shows that a careful calibration of the polarization of the neutron beam is needed.

Chapter 7 on Fe/Si multilayers clearly shows that spin parallel and spin antiparallel data should be measured with equally good statistical accuracy. Otherwise one of the two curves will dominate the parameter optimization process, and interchange between Γ_n and Γ_m can occur without influencing the quality of the fit to the data significantly. In chapter 7 the disagreement between the values of the magnetization as determined by PNR and by VSM indicated that the Γ_n-profile obtained initially was too low. In chapter 4 model calculations showed that the influence of statistical accuracy is not large. However the assumed statistical inaccuracy in this model study is much smaller than that of the data described in chapter 7.

A systematic program of measurements on tapes on which signals with currents of different amplitudes are written, can give more insight into the depth dependence of the writing process as a function of current amplitude. Also opposite signals can be written on the tape using the wide recording head and an AC current. The in-plane variation by the opposite magnetized domains will result in off-specular reflection, which can be measured with a position sensitive detector.

Bibliography

[1] J.A.C. Bland, J. Lee, S. Hope, G. Lauhoff, J. Penfold and D. Bucknall, Journ. of Magn. and Magn. Mat. **165**(1997) 46.

[2] C. Vettier, Physica B **192** (1993) 1.

[3] F. de Bergevin and M. Brunel, Acta Crystallogr. A **37** (1981) 314.

[4] S.W. Lovesey, J. Phys. C: Solid State Phys. **20** (1987) 5625.

[5] D. Gibbs, D.R. Harshman, E.D. Isaacs, D.B. McWhan, D. Mills, and C. Vettier, Phys. Rev. Lett. **61** no 10 (1988) 1241.

[6] G.P. Felcher, Physica B **192** (1993) 137.

[7] C. Kao, J.B. Hastings, E.D. Johnsen, D.P. Siddons, G.C. Smith and G.A. Prinz, Phys. Rev. Lett. **65** (1990) 373.

[8] V.F. Sears, 'Neutron Optics', (Oxford University Press, Oxford, 1989).

[9] J. Lekner, 'Theory of Reflection of Electromagnetic and Particle Waves', (Martinus Nijhoff Publishers, Dordrecht, 1987).

[10] S.W. Lovesey, 'Theory of neutron scattering from condensed matter', Volume 2, (Clarendon Press, Oxford, 1984).

[11] S.J. Blundell and J.A.C. Bland, Phys. Rev. B **46** (1992) 3391.

[12] G.P. Felcher, R.O. Hilleke, R.K. Crawford, J. Haumann, R. Kleb and G. Ostrowski, Rev. Sci. Instrum. **58** (1987) 609.

[13] V.-O. de Haan, "ROG a neutron reflectometer at the IRI", PhD thesis, Delft University of Technology, (1995).

[14] V.-O. de Haan, J. de Blois, P. van der Ende, H. Fredrikze, A. van der Graaf, M.N. Schipper, A.A. van Well, J. van der Zanden, Nucl.Instr. and Meth. A **362** (1995) 434-453.

[15] M.T. Rekveldt, P. Verkerk and A.A. van Well, Nuclear Instruments and Methods in Physics Research **B34** (1988) 285-289.

[16] P. Verkerk, A.A. van Well and M.T. Rekveldt, Physica B, **156 & 157** (1989) 544- 546.

[17] A.A. van Well, Physica B **180** & **181** (1992) 959.

[18] W.H. Kraan, M.Th. Rekveldt and P.T. Por, Nucl. Instr. and Meth. A **300** (1991) 35.

[19] P.T. Por, W.H. Kraan and M.Th. Rekveldt, Nuclear Instruments and Methods in Physics Research A **339** (1994) 550-555.

[20] Private communication with H. Fredrikze.

[21] A. Seeger 'Moderne Probleme der Metallphysik' (Springer-Verlag, Berlin-Heidelberg-New York, 1966).

[22] J. Penfold, J. de Phys **50** (1989) C7-99.

[23] R. Felici, J. Penfold, R.C. Ward and W.G. Williams, 'The Calibration of Slow Neutron Polarised Beam Instruments', Rutherford Appleton Laboratory Report RAL-87-025, April 1987.

[24] J. Penfold, 'Polarisation Calibration on Crisp', Crisp Commissioning Note, 6 February 1992.

[25] S. Iwasaki and Y. Nakamura, IEEE Trans. Magn. MAG-**13**, 5 (1977) 1272.

[26] J.C. Lodder, J.M.M.M. **159** (1996) 238-248.

[27] Y. Nakamura, J. Magn. Soc. Japan, **15**, Supplement S2 (1991).

[28] J.C. Lodder, "Co-Cr-(X) thin films for high density recording", PhD thesis, Twente University of Technology (1995) 115.

[29] Y. Maeda, and M. Asahi, J.Appl.Phys., **61(5)** (1987) 1972.

[30] T.J.L. Jones and W.G. Williams, Nucl. Instr. and Meth. **152** (1987) 463.

[31] A. van der Graaf, H. Fredrikze, P. de Haan, M.Th. Rekveldt and J.C. Lodder, Journ. of Magn. and Magn. Mat. **140-144** (1995) 695-696.

[32] J.Penfold, "UPdate on polarised neutron calibration on CRISP", CRISP Commissioning Note, 22 April 1993.

[33] E.R. Cohen and B.N. Taylor, Physics Today, August 1996 BG 9.

[34] V.F. Sears, Neutron News 3, No. 3 (1992) 26.

[35] A. Feuerstein, M. Mayr, IEEE Trans. Magn. **MAG-20**, (1984), 51-56.

[36] P. ten Berge, L. Abelmann, C. Lodder, A. Schrader, S. Luitjens, J. Magn. Soc. Japan **18**, Supplement S1 (1994), 295-298.

[37] G. Bottoni, D. Candolfo and A. Cecchetti, presented at intermag '94.

[38] 'Bits op de korrel; Magnetische registratie en interactie', inaugural lecture of Prof.Dr.Ir. S.B. Luitjens, University of Twente, 24 november 1994.

[39] D. Henderson, M. Brodsky and P. Chandeasi, Applied Physics Letters, **25** no. 11, (1974) 641.

[40] J.P.C. Bernards, S.E. Stupp, H.A.J. Cramer, J. Magn. Soc. Japan **18**, Supplement S1 (1994), 287-290.

[41] K. Chiba, K. Sato, Y. Ebine and T. Sasaki, IEEE Transactions on Consumers Electronics, **35** (1989) 421-427.

[42] J. Penfold and R.K. Thomas, J.Phys.: Condens. Matter **2** (1990) 1369.

[43] A.A. van Well, V.-O. de Haan, H. Fredrikze, Physica B **198** (1994) 217-219.

[44] H.J. Richter, IEEE Trans. Magn. **29** (1993) 21-33.

[45] P.T. Por and M.Th.Rekveldt, Journ. of Magn. and Magn. Mat. **161** (1996) 357.

[46] S.E. Stupp and J.P.C. Bernards, Journ. of Magn. and Magn. Mat. **155** (1996) 300-302.

[47] Private communication with P.T. Por.

[48] M. Rührig, R. Schäfer, A. Hubert, R. Mosler, J.A. Wolf, S. Demokritov and P. Grünberg, Phys. Status Solidi A **125**, (1991) 635.

[49] P. Bruno, Phys.Rev.B **52** (1995) 411.

[50] S. Toscano, B. Briner, H. Hopster and M. Landolt, Journ. Magn. Magn. Mat. **114** (1992) L6.

[51] E.E. Fullerton, J.E. Mattson, S.R. Lee, C.H.Sowers, Y.Y. Huang, G. Felcher and S.D. Bader, Journ. Magn. and Magn. Mat. **117** (1992) L301.

[52] J.E. Mattson, Sudha Kumar, Eric E. Fullerton, S.R. Lee, C.H. Sowers, M. Grimsditch, S.D. Bader, F.T. Parker, Phys. Rev. Lett. **71** 185.

[53] E.E. Fullerton and S.D. Bader, Phys. Rev. B, **53** no 9 (1996) 5112.

[54] B. Briner and M. Landolt, Phys. Rev. Lett. **73** (1994) 340.

[55] F.J.A. den Broeder and J. Kohlhepp, Phys. Rev. Lett. **75** no 16 (1995) 3026.

[56] J. Kohlhepp and F.J.A. den Broeder, Journ. of Magn. and Magn. Mat. **156** (1996) 261.

[57] K. Inomata, K. Yusu and Y. Saito, Phys. Rev. Lett. **74** no 10 (1995) 1863.

[58] J. Kohlhepp, M. Valkier, A. van der Graaf and F.J.A. den Broeder, Journ. of Magn. and Magn. Mat. **165** (1997) 431.

[59] A. Chaiken, R.P. Michel and M.A. Wall, Phys. Rev. B **53** no 9 (1996) 5518.

[60] A. van der Graaf, M. Valkier, J. Kohlhepp and F.J.A. den Broeder, Journ. Magn. and Magn. Mat. **165** (1997) 157-160.

[61] J. Kohlhepp, M. Valkier, A. van der Graaf, Phys. Rev. B **55** no 2 (1997) R696.

[62] H. von Känel, K.A. Mäder, E. Müller, N. Onda andH. Sirringhaus, Phys. Rev. B **45** no 23 (1992) 13807.

[63] K.A. Mäder, H. von Känel and A. Baldereschi, Phys. Rev. B **48** no 7 (1993) 4364.

[64] J. Dekoster, H. Bemelmans, S. Degroote, R. Moons, A. Vantomme and G. Langouche, presented at E-MRS springmeeting 1996 Strassbourg.

[65] W.H. Meiklejohn and C.P. Bean, Phys. Rev. **102** (1956) 1413. W.H. Meiklejohn and C.P. Bean, Phys. Rev. **105** (1957) 904. W.H. Meiklejohn Journal of Applied Physics, suppl. to **33**, no. 3. (1962) 1328.

[66] J.C.S. Kools, IEEE Trans. Magn. **32** (1996), 3165.

[67] J.C.S. Kools, Th.G.S.M. Rijks, A.E.M. De Veirman, D. Neerinck and R.F.O. Reneerkens, "Microstructure of sputter-deposited $Ni_{80}Fe_{20}/Cu/Ni_{80}Fe_{20}/FeMn$ spinvalves", unpublished.

[68] C. Meny, J.P. Jay, P. Panissod, P. Humbert, V.S. Speriosu, H. Lefakis, J.P. Nozieres and B.A. Gurney, "Annealed Cu/Co/Cu/NiFe/FeMn spinvalves: Nanostructure and magnetism," MRS Proc, **313** (1993) 289.

[69] L. Néel, Comptes Rendus **225** (1962) 1676.

[70] A. Fert and I.A. Campbell, J.Phys.F **6** (1976) 849.

[71] B.A. Gurney, V.S. Speriosu, J.P. Nozières, H. Lefakis, D.R. Wilhoit and O.U. Need, Phys.Rev.Lett. **71** (1993) 4023.

[72] B. Dieny, Journ. of Magn. and Magn. Mat. **136** (1994) 335.

[73] Th.G.S.M. Rijks, R. Coehoorn, J.T.F. Daemen and W.J.M. de Jonge, J. Appl. Phys. **76** (2) (1994) 1092.

[74] A. van der Graaf, A.R. Ball and J.C.S. Kools, Journ. of Magn. and Magn. Mat. **165** (1997) 479.

[75] J, Nishioka, G. Gangopadhyay, H. Fujiwaran and M. Parker, IEEE Trans. Magn. **31** (1995) 3949.

[76] M.R. Parker, H. Fugiwara, S. Hossain and W.E. Webb, IEEE Trans. Magn. **31** (1995) 2618.

[77] M. Labrune, J.C.S. Kools, A. Thiaville and D.Tomas, presented at MML conference, Cambridge, (1995).

[78] D. Mauri, H.C. Siegmann, P.S. Bagus and E. Kay, J.Appl. Phys. **62** (1987) 3047.

Summary

Polarized Neutron Reflectometry on Thin Magnetic Films

by Anja van der Graaf

In january 1993 the neutron reflectometer ROG was installed at IRI. The specular neutron reflectivity as a function of the perpendicular component of the incoming neutron momentum is determined by the neutron scattering length density as a function of depth. This neutron scattering length density contains a nuclear and a magnetic contribution, which can be separated by using ROG in polarized mode, i.e. with the magnetic moment of the neutrons in the same direction. In this thesis pioneering polarized neutron reflectometry (PNR) experiments performed on ROG are described. To develop experience with the technique of polarized neutron reflectometry also experiments were performed on CRISP, the neutron reflectometer of the Rutherford Appleton Laboratory at the ISIS facility, which can be used in polarized mode.

ROG is a TOF(time of flight)-reflectometer, meaning that the time of arrival of pulsed neutrons is registered. From the time of arrival the velocity and the associated wavelength of each arriving neutron is deduced. The neutron beam can be polarized by reflection on a polarizing mirror with much higher reflectivity for neutrons with one of the two possible spin states. The sign of the magnetic term of the neutron scattering length density is determined by the direction of the polarization of the beam compared to the magnetization in the sample. Usually PNR-experiments are performed with the polarization of the beam subsequently parallel and antiparallel to the magnetic field applied to the sample. The polarization direction of ROG can be reversed using an adiabatic spin flipper. The degree of polarization of the beam hitting the surface of the sample is the same for both polarization directions of the beam. All components of the apparatus can be set automatically controlled, to optimize the reproducibility of the settings.

The calibration of the polarization degree of the ROG using the 3P2S-method is

described. As this polarization degree influences the measured intensities directly, each measurement has to be corrected for the polarization degree before it can be interpreted in terms of magnetization depth profiles.

All experiments, presented in this thesis, are interpreted using the so-called matrix method. This method approximates the neutron scattering length density as a function of depth, by slabs of constant scattering length density. The neutron wave function in each subsequent slab is determined by the boundary conditions that the wave function itself and its derivative should be continuous at the interface. Using these boundary conditions a matrix for each slab is defined. This matrix is used to calculate the influence of the slab on the reflectivity curve. From model calculations it is clear that poor calibration of the degree of polarization has in general a larger influence on the data with lower reflectivity (in most cases the spin antiparallel data). When the lower reflectivity data are also measured with less statistical accuracy, the parameter optimizing routine might be dominated by the higher reflectivity data. In that case an interchange between the magnetic and nuclear part of the neutron scattering length density might occur. Furthermore it will be more difficult to find any acceptable set of parameter values, describing the measured data.

PNR-experiments on a 140 nm Co-Cr layer at various in-plane magnetic fields have been performed. Co-Cr is considered as a candidate for a perpendicular recording medium, because of the easy axis of magnetization perpendicular to the surface. However these Co-Cr layers are known to exhibit a so-called 'initial layer' at the substrate. This initial layer exhibits a decrease of the perpendicular anisotropy. Interpretation of the PNR-data measured at low magnetic field shows a gradual decrease of the perpendicular anisotropy from the surface to the substrate instead of a discrete initial layer. The minimum of perpendicular preference of the easy-axis and also the maximum of the remanent magnetization in-plane occurs at about 30 nm of the substrate. At high magnetic field the in-plane magnetization shows also a gradual increase from the surface towards the substrate. This can be explained by the structure of the layer. Close to the substrate the layer contains more grain boundaries, while further away from the substrate the grains become larger and the layer contains less grain boundaries. Chromium tends to dissolve in the grain boundaries. As the spontaneous magnetization of Co-Cr depends sensitively on the fraction chromium, the in-plane magnetization at saturation increases from the top towards the bottom of the sample.

Metal Evaporated videotapes in different magnetic states are investigated by PNR. The experiments were performed on tapes sputtered in one and two shifts, to which will be referred as one-layer and two-layer tape. The fitted profiles show that the nuclear part of the neutron scattering length density increases during one sputter shift. This can be caused by the layer becoming more dense (less porous), but also by compositional changes with depth. From the models fitted to the measured data an upper estimate of the fraction of voids is found of 46 and 51 % for the one- and two-layer tape respectively.

Using an 11 mm wide recording head a DC signal was written on both tapes. Analysis of PNR-data obtained from these written tapes, show that the record-

ing head writes throughout the whole depth of the tape. It is also clear that the measurements on the two-layer metal evaporated tape can very well be described by a model assuming a non-magnetic region in between the two sputtered layers. The two layers of the two-layer tape have been sputtered with an opposite angle of incidence. The model fitted to PNR-data in remanence after perpendicular magnetization show the opposite in-plane component of magnetization. It is determined that the product of the saturation magnetization and the thickness, M_sT is higher for the layer at the surface side of the two-layer tape.

Because in the literature indications are given that the magnetic coupling in Fe/Si multilayers with a crystalline FeSi spacer is depth-dependent, PNR-experiments were performed on such multilayers. The multilayers contained twenty Fe/Si bilayers, with a nominal iron sublayer of 3 nm thick and a nominal silicon thickness of 1.1 or 1.4 nm. During sputtering Fe diffuses into Si, resulting in a crystalline FeSi spacer. The magnetic behaviour of these multilayers appeared to be indeed strongly depth-dependent. On the substrate side the magnetization in consecutive iron layers behaves predominantly as a ferromagnet, while at the surface side the magnetization in consecutive iron layers behaves predominantly as an antiferromagnet. These results are in agreement with MOKE-results measured on Fe/Si multilayers on glass. However, PNR gives a model of the magnetization alignment over the whole depth of the multilayer.

The decrease of ferromagnetic coupling with distance from the substrate is probably caused by a decrease of percolation paths of iron atoms (pinholes) through the spacer layers from the substrate towards the surface of the multilayer. The pinholes short-circuit the magnetization through the spacer, resulting in a preference for ferromagnetic alignment. During sputtering the concentration of pinholes becomes smaller because the multilayer becomes more perfect. Also the nuclear density of the Fe/Si multilayer increases from the substrate towards the surface. Furthermore less antiferromagnetic alignment appears to be present in the 1.1 nm Si sample, but the antiferromagnetic coupling present is stronger. Apparently the exchange coupling is stronger for this spacer thickness, but also more pinholes are present.

The reversal of the magnetization in the separate ferromagnetic layers of a spin-valve system is researched by PNR. A spin-valve system contains two ferromagnetic layers separated by a non-magnetic layer. One of the ferromagnetic layers is exchange-biased by an adjacent antiferromagnetic layer. When a magnetic field opposing the exchange-biasing is applied, the magnetization in the unbiased layer will change its direction at a lower field value than the biased layer. Therefore, the magnetization in the two ferromagnetic layers is aligned antiparallel at a certain magnetic field value, resulting in an increase in electrical resistance, so-called giant magnetoresistance. This characteristic of spin-valves makes them suitable candidates as the sensitive material in read heads.

On NiFe/Cu/NiFe/FeMn spin-valve systems PNR-experiments are performed at different magnetic fields. The interpretation of the PNR-experiments shows that in a spin-valve system with a copper layer thickness of 1.5 nm the magnetization in the ferromagnetic NiFe-layers rotates much more independently then in

a spin-valve system with a copper layer thickness of 1.0 nm. The obtained results agree well with energy minimalization calculations. The results also indicate that the antiferromagnet which exchange-biased one permalloy layer, contains a net magnetic moment at a layer of about 5 nm at the interface with the ferromagnetic layer.

Samenvatting

Gepolariseerde Neutronen Reflectometrie aan Dunne Magnetische Lagen

door Anja van der Graaf

In januari 1993 is de neutronen reflectometer ROG van het IRI in gebruik genomen. De speculaire neutronen reflectiviteit als functie van de loodrechte component van de inkomende neutronen impuls wordt bepaald door de neutronen verstrooiingslengtedichtheid als functie van diepte. Deze neutronen verstrooiingslengtedichtheid bevat een nucleaire en een magnetische bijdrage, die van elkaar gescheiden kunnen worden door reflecties van twee tegengesteld gepolariseerde bundels te meten. Een gepolariseerde neutronen bundel vertoont een voorkeursrichting van de magnetische momenten van de neutronen. In dit proefschrift worden verkennende gepolariseerde neutronen reflectie (PNR) experimenten op de ROG beschreven. Om ervaring met de techniek gepolariseerde neutronen reflectometrie op te bouwen werden ook experimenten uitgevoerd op CRISP, de neutronen reflectometer op het Rutherford Appleton Laboratorium van ISIS, waarop ook metingen met gepolariseerde bundels kunnen worden uitgevoerd.

ROG is een TOF(time of flight)-reflectometer, dat wil zeggen dat de tijd van aankomst van gepulste neutronen wordt geregistreerd. Uit de tijd van aankomst kan de snelheid en de daaraan gekoppelde golflengte van ieder gedetecteerd neutron worden afgeleid. De neutronen bundel kan worden gepolariseerd door reflectie aan een polariserende spiegel met een veel hogere reflectiviteit voor neutronen met één van de twee mogelijke spin toestanden. Het teken van de magnetische term van de neutronen verstrooiingslengtedichtheid wordt bepaald door de richting van de polarisatie van de bundel ten opzicht van de magnetisatie van het preparaat. Gewoonlijk worden PNR-experimenten uitgevoerd met de polarisatie van de bundel zowel parallel als anti-parallel aan het over het preparaat aangelegde magnetisch veld. De polarisatie van de bundel kan worden omgekeerd met een adiabatische spinflipper. De polarisatiegraad van de bundel, invallend op

het preparaat, is hetzelfde voor beide polarisatie richtingen van de bundel. Alle componenten van het apparaat kunnen geautomatiseerd worden bestuurd, om de reproduceerbaarheid van de instellingen te optimaliseren.

De ijking van de polarisatiegraad van de ROG met de 3P2S-methode wordt beschreven. Omdat de polarisatiegraad de gemeten intensiteiten direct beïnvloedt, moet iedere meting worden gecorrigeerd voor de polarisatiegraad, voordat deze kan worden geïnterpreteerd in termen van magnetisatie diepte profielen.

Alle metingen beschreven in dit proefschrift zijn geïnterpreteerd met de zogenaamde matrix methode. Deze methode benadert de neutronen verstrooiingslengtedichtheid als functie van diepte door lagen met constante verstrooiingslengtedichtheid. De neutronen golffunctie in iedere volgende laag wordt bepaald door de randvoorwaarden dat zowel de golffunctie zelf als ook de afgeleide continu zijn op het grensvlak. Met behulp van deze randvoorwaarden wordt een matrix voor iedere laag gedefinieerd. De matrix wordt gebruikt om de invloed van de laag op het reflectiviteitspatroon te berekenen. Uit model berekeningen blijkt dat een slechte ijking van de polarisatiegraad in het algemeen een grotere invloed heeft op de meetpunten met lagere reflectiviteit (in de meeste gevallen de spin antiparallel data). Als de meetpunten met lagere reflectiviteit ook worden gemeten met grotere statistische onnauwkeurigheid, kan de parameter optimalizatie routine worden gedomineerd door de meetpunten met hogere reflectiviteit. In dat geval kan een uitwisseling tussen het magnetische en nucleaire deel van de neutronen verstrooiingslengtedichtheid optreden. Verder zal het moeilijker zijn om een acceptabele set van parameter waarden te vinden om de meetpunten te beschrijven.

PNR-experimenten aan een 140 nm dikke Co-Cr laag bij verschillende magnetische velden in het vlak zijn uitgevoerd. Co-Cr wordt beschouwd als een kandidaat medium voor loodrechte recording, vanwege de voorkeursrichting van de magnetisatie loodrecht op het oppervlak. Echter, deze Co-Cr lagen staan er om bekend een zogenaamde 'initiële laag' aan de substraat kant te vertonen. Deze initiële laag vertoont een verminderde loodrechte anisotropie. Interpretatie van de PNR-data, gemeten in lage magnetische velden vertoont een geleidelijke afname van de loodrechte anisotropie van het oppervlak richting substraat in plaats van een discrete initiële laag. Het minimum van de loodrechte oriëntatie van de voorkeursrichting van magnetisatie en ook het maximum van de remanente magnetisatie in het vlak, ligt op ongeveer 30 nm afstand van het substraat. Bij hoge magnetische velden vertoont de magnetisatie in het vlak ook een geleidelijke toename vanaf het oppervlak richting substraat. Dit kan worden verklaard uit de structuur van de laag. Dichtbij het substraat bevat de laag meer korrelgrenzen, terwijl op grotere afstand van het substraat de korrels groter worden en de laag minder korrelgrenzen bevat. Chroom neigt tot oplossen in de korrelgrenzen. Omdat de spontane magnetisatie van Co-Cr erg gevoelig is voor de fractie chroom, neemt de magnetisatie in het vlak in verzadiging toe van het oppervlak richting substraat.

Metal Evaporated videotapes in verschillende magnetische toestanden zijn onderzocht met PNR. De experimenten zijn uitgevoerd aan tapes gesputterd in één of twee gangen, die respectievelijk één-laags en twee-laags tape worden genoemd.

Uit de gefitte modellen blijkt dat het nucleaire deel van de neutronen verstrooiingslengtedichtheid toeneemt tijdens één sputtergang. Dit kan worden veroorzaakt doordat de tape minder poreus wordt tijdens het sputteren, maar ook door veranderende chemische samenstelling. Uit de gefitte modellen volgt een schatting voor de bovengrens van de porieën fractie van 46 en 51 % voor de één- en twee-laags tape respectievelijk.

Met een 11 mm brede schrijfkop werd op beide tapes een DC signaal geschreven. Analyse van PNR-data, gemeten aan deze tape, laat zien dat de schrijfkop schrijft over de gehele diepte van de tape. Het is ook duidelijk dat de metingen aan de twee-laags tape het best kunnen worden beschreven door een model dat een niet-magnetische gebied tussen de twee gesputterde lagen aanneemt. De twee lagen van de twee-laags tape zijn gesputterd bij een tegenovergestelde invalshoek. De PNR-data van de twee-laagse tape in remanentie, na loodrechte magnetisatie, is gemeten. Het model dat aan deze data is gefit, laat duidelijk de tegenovergestelde componenten van de magnetisatie in het vlak in de afzonderlijke lagen zien. Het is vastgesteld dat het produkt van verzadigingsmagnetisatie en de dikte, M_sT hoger is voor de laag aan het oppervlak van de twee-laags tape.

Op grond van aanwijzingen in de literatuur dat de magnetische koppeling in Fe/Si multilagen met een kristallijne FeSi tussenlaag diepte afhankelijk is, werden PNR-experimenten aan dergelijke multilagen uitgevoerd. De multilagen bevatten twintig Fe/Si bilagen, met een nominale ijzer laagdikte van 3 nm en een nominale silicium laagdikte van 1.1 of 1.4 nm. Tijdens het sputterproces diffundeert ijzer in silicium, wat resulteert in een kristallijne FeSi tussenlaag. Het magnetisch gedrag van deze multilagen blijkt sterk afhankelijk van de diepte te zijn. Aan de substraat zijde is de magnetisatie in opeenvolgende ijzerlagen hoofdzakelijk ferromagnetisch gerangschikt, aan het oppervlak daarentegen is de magnetisatie in opeenvolgende ijzerlagen hoofdzakelijk anti-ferromagnetisch gerangschikt. Deze resultaten zijn in overeenstemming met MOKE-resultaten gemeten aan Fe/Si multilagen op glas. PNR geeft echter een model rangschikking van de magnetisatie over de gehele diepte van de multilaag.

De afname van de ferromagnetische koppeling met afstand van het substraat wordt waarschijnlijk veroorzaakt door de afname van percolatie paden (pinholes)van ijzer atomen door de tussenlaag, vanaf het substraat naar het oppervlak van de multilaag. De percolatie paden sluiten de magnetisatie kort door de tussenlaag, wat resulteert in een voorkeur voor ferromagnetische rangschikking. Tijdens het sputteren van de lagen wordt de concentratie van de percolatie paden kleiner omdat de multilaag perfecter wordt. De nucleare dichtheid van de Fe/Si multilagen neemt toe vanaf het substraat in de richting van het oppervlak. Verder blijkt minder anti-ferromagnetische rangschikking aanwezig te zijn in het 1.1 nm Si preparaat, maar de aanwezige anti-ferromagnetische koppeling is sterker dan in het 1.4 nm Si preparaat. Blijkbaar is de exchange koppeling sterker. Het feit dat minder anti-ferromagnetische rangschikking aanwezig is in het 1.1 nm Si preparaat, wijst erop dat dit preparaat meer percolatie paden bevat dan het 1.4 nm Si preparaat.

Het omklappen van de magnetisatie in de afzonderlijke ferromagnetische lagen van een 'spin-valve' systeem is onderzocht met PNR. Een 'spin-valve' systeem be-

vat twee ferromagnetische lagen, van elkaar gescheiden door een niet-magnetische laag. Eén van de ferromagnetische lagen wordt 'geëxchange-biased' door een aangrenzende anti-ferromagnetische laag. Als een magnetisch veld wordt toegepast dat de 'exchange-biasing' tegenwerkt, zal de richting van de magnetisatie in de 'niet-gebiasde' laag al bij een lager veld omklappen dan in de 'gebiasde' laag. Hierdoor bestaat er een veld interval waarvoor de magnetisatie in de twee ferromagnetische lagen anti-parallel gerangschikt is, wat resulteert in een toename van de elektrische weerstand, zogenaamde reuze magnetoweerstand. Deze eigenschap van 'spin-valve' systemen maakt hen geschikte kandidaten als gevoelig materiaal in leeskoppen.

Aan NiFe/Cu/NiFe/FeMn 'spin-valve' systemen zijn PNR-experimenten bij verschillende magnetische velden uitgevoerd. De interpretatie van de PNR-experimenten laat zien dat in het preparaat met een koperlaagdikte van 1.5 nm de magnetisatie in de ferromagnetische NiFe-lagen veel onafhankelijker omdraait dan in een preparaat met een koperlaagdikte van 1.0 nm. De verkregen resultaten komen goed overeen met energie minimalisatie berekeningen. De resultaten duiden op een magnetisch moment in de anti-ferromagnetische laag, in een gebied tot 5 nm afstand van het grensvlak met de 'gebiasde' ferromagnetische laag.

Glossary of Symbols

$\vec{\mathbf{B}}$	magnetic induction [T]
b	total neutron scattering length [m]
b_n	nuclear neutron scattering length [m]
c	velocity of light [m/s]
D	distance between sample and detector, measured along the z-axis [m]
dev^2	measure for quality of fit, when χ^2 is not defined [-]
E	total energy [J]
E_{EB}	exchange energy at interface between ferromagnetic and antiferromagnetic material[J]
e	elementary charge [C]
f	flipper efficiency[-]
J_1	bilinear coupling parameter between magnetization in two layers [Jm^{-2}]
J_2	biquadratic coupling parameter between magnetization in two layers[Jm^{-2}]
$\vec{\mathbf{H}}$	magnetic field [A/m]
h	height of detector above direct neutron beam [m]
$\hbar$	constant of Plank, divided by 2π [Js]
I^+	intensity of neutron beam at detector position with spin parallel to the magnetization [$\mathrm{s}^{-1}\mathrm{m}^{-2}$]
I^-	intensity of neutron beam at detector position with spin antiparallel to the magnetization [$\mathrm{s}^{-1}\mathrm{m}^{-2}$]
I^{++}	intensity of neutron beam at detector position with first and second spin flipper in non-flip mode [$\mathrm{s}^{-1}\mathrm{m}^{-2}$]
I^{+-}	intensity of neutron beam at detector position with first in non-flip and second spin flipper in flip mode [$\mathrm{s}^{-1}\mathrm{m}^{-2}$]
I^{-+}	intensity of neutron beam at detector position with first in flip and second spin flipper in non-flip mode [$\mathrm{s}^{-1}\mathrm{m}^{-2}$]
I^{--}	intensity of neutron beam at detector position with first and second spin flipper in flip mode [$\mathrm{s}^{-1}\mathrm{m}^{-2}$]
$\vec{\mathbf{k}}$	wave vector [nm^{-1}]
L	distance between the end of the neutron guide and the sample [m]
$\vec{\mathbf{M}}$	magnetization [A/m]
$\vec{\mathbf{M}}_{//}$	in plane magnetization [A/m]
M_s	magnitude of spontaneous magnetization [A/m]

M_r	magnitude of remanent magnetization [A/m]
$\mathsf{m_s}$	matrix corresponding to single interface [-]
$\mathsf{m_i}$	matrix corresponding to i'th interface with layer [-]
M	matrix corresponding to sample [-]
M_p	in-plane magnetization component in polarization direction [A/m]
m_n	mass neutron [kg]
m_p	mass proton [kg]
m	number of datapoints measured at one field value/ physical state [-]
N	number of datapoints in total fit [-]
n	number density [nm^{-3}]
P	polarization degree [-]
p	number of parameters used in fit [-]
p	magnetic neutron scattering length [m]
p_{base}	background pressure [Pa]
Q	wave number transfer [nm^{-1}]
q	component of wavevector perpendicular to samle surface [nm^{-1}]
q_{cr}	critical q-value[nm^{-1}]
R	neutron reflectivity [-]
R^+	spin parallel neutron reflectivity [-]
R^-	spin antiparallel neutron reflectivity [-]
R^{++}	neutron reflectivity with first and second spin flipper in non-flip mode [-]
R^{+-}	neutron reflectivity with first spin flipper in non-flip and second in flip mode [-]
R^{-+}	neutron reflectivity with first spin flipper in flip and second in non-flip mode [-]
R^{--}	neutron reflectivity with first and second spin flipper in flip mode [-]
$\vec{\mathbf{r}}$	position vector [m]
r	reflection amplitude [-]
s	estimated standard deviation or width of the sample [-/m]
T_i	thickness of i'th layer [nm]
T_C	Curie temperature [K]
t	transmission amplitude [-]
V	potential energy [J]
w	width of the neutron guide [m]
x, y, z	carthesian coordinates
α	critical angle of reflection of neutron guides [mrad]
α_1	depolarization of the neutron beam before it hits the sample [-]
α_2	depolarization of the neutron beam after it hits the sample [-]
η	random number to simulate statistics [-]
ζ	angle between magnetic induction and polarization of the neutron beam [-]
γ	gyromagnetic ratio [-]
Γ	neutron scattering length density (in fact multiplied by 4 π) [m^2]
Γ_n	nuclear part of Γ [m^2]
Γ_m	magnetic part of Γ [m^2]

ρ	electrical resistivity (Ωm)
θ	angle of incidence [rad]
θ_{cr}	critical angle of incidence [rad]
β_i	angle between applied negative field and magnetization (chapter 7) [rad]
λ	wave length [m]
μ_0	magnetic permeability of vacuum [Hm$^-$1]
μ_N	nuclear magneton [JT$^-$1]
$\vec{\mu_{\mathbf{n}}}$	magnetic momentum of neutron [JT$^-$1]
$\vec{\sigma}$	spin [-]
σ	roughness [m]
Ψ	neutron wave function
ψ	neutron wave function in one dimension
ϕ	derivative of neutron wave function in one dimension
χ^2	measure for quality of fit defined by equation 4.30

Dankwoord

Iedereen die bijgedragen heeft aan het werk beschreven in dit proefschrift ben ik dankbaar. De volgende personen wil ik in het bijzonder noemen:

Mijn promotor Leo de Graaf, ben ik dankbaar voor het vertrouwen dat hij in me heeft gesteld, mijn co-promotor Theo Rekveldt voor de met begeestering gevoerde discussies en Henk Fredrikze voor zijn begeleiding, zijn ruime sociale belangstelling en de ritjes naar huis na laat werk.

Ik ben Cock Lodder en Poul de Haan van het MESA Research Institute van de Technische Universiteit Enschede erkentelijk voor het beschikbaar stellen van het Co-Cr preparaat, dat in hoofdstuk 5 beschreven wordt.

Hoofdstuk 6, 7 en 8 zijn ontstaan in samenwerking met Philips Research Laboratories. Ik wil Hugo Cramer en Steven Stupp danken voor de samenwerking met betrekking tot de metal evaporated tapes; Jürgen Kohlhepp en Frits den Broeder voor het maken van de Fe/Si multilagen en de discussies over de interpretaties van de PNR-metingen; Jacques Kools voor het sputteren van de spin-valve samples en Andrew Ball voor zijn hulp bij de PNR-experimenten hieraan. Theo Rijks bedank ik hartelijk voor het beschikbaar stellen van Figuur 8.4.

Ik dank Marc Valkier, die als zijn afstudeerwerk metingen met de eerste interpretatie aan de Fe/Si multilagen heeft verricht; Victor de Haan omdat hij mij heeft ingewijd in de besturing van de ROG en de software voor simulatie en data bewerking; Piet van der Ende voor hulp op meettechnisch gebied en zijn altijd open oor; Martijn Schipper en Toine Beunes voor de instant hulp bij computer problemen tijdens experimenten; Jan van der Zanden en Hans Perre voor mechanische ondersteuning; Peter Por dank ik voor de nuttige discussies over met name metal evaporated tapes en Rita Bijlsma voor de hulp bij de laatste loodjes.

Binnen de vakgroep stralingsfysica heb ik een gezellige en leerzame tijd beleefd, met veel sociale activiteiten, koffie en humor in de IRI-bar. Alle lopers dank ik voor het ontspannende zweten tijdens de lunch; Ed Osterholt speciaal voor zijn aansporingen tot hardlopen en Wicher Kraan voor de geboden competitie: wat een maatwerk! Mijn kamergenoten, en andere slachtoffers, wil ik bedanken voor het luisteren als ik mijn verhaal kwijt wilde. En natuurlijk dank ik alle collega's, die de vakgroep stralingsfysica voor mij tot een warm nest maakten.

Rob Eek, je onverwoestbare kameraadschap heeft me vaak geholpen tijdens de afgelopen IRI-jaren, dankjewel.

Curriculum Vitae

Anja van der Graaf was born 25 May 1966 in Lekkerkerk. She graduated in June 1984 from gymnasium-β at Scholengemeenschap 'de Krimpenerwaard' in Krimpen a/d IJssel. In February 1991 she obtained a masters degree in Materials Science at the Delft University of Technology. Her graduation work took place in the section Physical Chemistry of the Solid State, and her graduation thesis described amorphization in Ni/Ti multilayers investigated by in-situ electrical resistivity measurements.
From May 1991 until April 1992 she worked in the X-ray department of Corporate Research of Akzo-Nobel. From April 1992 she has been working at IRI. There she investigated thin magnetic layers by polarized neutron reflectometry supervised by dr. H. Fredrikze and dr. M. Th. Rekveldt. This work is described in this thesis.

List of Publications

A. van der Graaf, M.A. Hollanders, B.J. Thijsse and E.J. Mittemeijer, "Evidence for amorphization in Ni/Ti multilayers from electrical resistivity", Materials Science and Engineering **A133** (1991) 636-639.

A. van der Graaf, H.Fredrikze, P. de Haan, M.Th. Rekveldt and J.C. Lodder, "Polarized neutron reflectometry on Co-Cr", Journ. of Magn. and Magn. Mat. **140-144** (1995) 695-696.

V.-O. de Haan, J. de Blois, P. van der Ende, H. Fredrikze, A. van der Graaf, M.N. Schipper, A.A. van Well, J. van der Zanden, "ROG, the neutron reflectometer at IRI, Delft," Nuclear Instruments and Methods in Physic Research A **362** (1995) 434-453.

A. van der Graaf, H. Fredrikze, M.Th. Rekveldt and S.E. Stupp, "Polarized neutron reflectometry on a two-layer ME-tape", Journ. of Magn. and Magn. Mat. **155** (1996) 303-305.

A. van der Graaf, H. Fredrikze, M.Th. Rekveldt, "Polarized neutron reflectometry on metal evaporated videotapes", Physica B **221** (1996) 393-397.

A.R. Ball, H. Fredrikze, P.J. van der Zaag, R. Jungblut, A. Reinders, A. van der Graaf and M.Th. Rekveldt, "Neutron reflectometry on an exchange biased $Ni_{80}Fe_{20}/Fe_{50}Mn_{50}$ bilayer", Journ. of Magn. and Magn. Mat., **148** (1995) 46-48.

J. Kohlhepp, M. Valkier, A. van der Graaf, F.J.A. den Broeder, "Apparant strong biquadratic exchange coupling in Fe/Si multilayers - the role of pinholes", Journ. of Magn. and Magn. Mat. **165** (1997) 431-434.

J.T. Kohlhepp, M. Valkier, A. van der Graaf, F.J.A. den Broeder, "Mimicking of a strong biquadratic exchane goupling in Fe/Si multilayers", Phys.Rev.B, **55** no. 2 (1997) R696-R699.

A. van der Graaf, A.R. Ball, J.C.S. Kools, "Magnetic alignment in spin-valve system studied by polarized neutron reflectometry", Journ. of Magn. and Magn. Mat. **165** (1997) 479-483.

A. van der Graaf, M. Valkier, J. Kohlhepp and F.J.A. den Broeder, "Interlayer coupling in Fe/Si multilayers studied by polarized neutron reflectometry", Journ. of Magn. and Magn. Mat. **165** (1997) 157-160.

Henk Fredrikze, Anja van der Graaf, Andrew Ball, Marc Valkier and Theo Rekveldt, "IRI polarized neutron reflectometry on magnetic (multi-)layers", Proceedings of the International Seminar "Polarized Neutrons for Condensed Matter Investigations" Dubna, June 18-20 (1996), 84-93.

W.H. Kraan, A. van der Graaf, H. Fredrikze, V.E. Mikhailova, M.Th Rekveldt, "Describing magnetisation and neutron depolarisation of perpendicular Co-Cr film with in-depth varying K(u)", Journ. of Magn. and Magn. Mat. **140-144** (1995), 1907-1908.

H. Fredrikze, A. van der Graaf, M. Valkier, J. Kohlhepp and F.J.A. den Broeder, "(Anti)-ferromagnetic coupling in Fe/Si multilayers from polarized neutron reflectometry", Physica B **234-236** (1997), 498-499.